MODELING OF CHIP FORMATION MECHANISM IN MACHINING CARBON FIBER REINFORCED POLYMER

by

Chunlei Song

B.A., South China University of Technology, 2013
M.S., Shanghai Jiao Tong University, 2017

A THESIS SUBMITTED IN PARTIAL FULFILLMENT OF
THE REQUIREMENTS FOR THE DEGREE OF

DOCTOR OF PHILOSOPHY

in

THE FACULTY OF GRADUATE AND POSTDOCTORAL STUDIES
(Mechanical Engineering)

THE UNIVERSITY OF BRITISH COLUMBIA
(Vancouver)

October 2022

The following individuals certify that they have read, and recommend to the Faculty of Graduate and Postdoctoral Studies for acceptance, the dissertation entitled:

MODELING OF CHIP FORMATION MECHANISM IN MACHINING CARBON FIBER REINFORCED POLYMER

submitted by **Chunlei Song** in partial fulfillment of the requirements for the degree of

Doctor of Philosophy in **Mechanical Engineering**

Examining Committee:

Dr. Xiaoliang Jin, Assistant Professor, Mechanical Engineering, UBC
Supervisor

Dr. Yusuf Altintas, Professor, Mechanical Engineering, UBC
Supervisory Committee Member

Dr. Clarence de Silva, Professor, Mechanical Engineering, UBC
University Examiner

Dr. Anoush Poursartip, Professor, Materials Engineering, UBC
University Examiner

Dr. Anasavarapu Srikantha Phani, Professor, Mechanical Engineering, UBC
Supervisory Committee Member

Dr. Reza Vaziri, Professor, Civil Engineering, UBC
Supervisory Committee Member

Abstract

Carbon fiber reinforced polymer (CFRP) composites possess high specific strength, high specific elastic modulus, and high energy absorption ability, which make them competitive in advanced industrial applications such as aerospace, automotive, and construction. To achieve the dimension and tolerance requirements of the CFRP components, cutting operations such as milling and drilling are necessary.

A mechanics model of the chip formation is developed to investigate the buckling failure mode, which occurs at 0° fiber orientation, by dividing the chip formation into shearing and buckling processes. The chip length increases owing to the shear failure in the interface layer until the Euler buckling or micro buckling failure is activated. The nonlinear relationship between the cutting forces and uncut material is modeled and validated by experiments.

A generalized mechanics model is proposed to predict the chip formation mode (fiber and matrix failure modes), chip formation angle, and cutting forces in the entire fiber orientation range of $[0°, 180°]$ for UD CFRP. For each fiber orientation, the stresses on the chip formation plane needed to activate the relevant chip formation mode, including fiber tension, fiber compression, matrix tension, and matrix compression, are determined. The chip formation plane which requires the minimum cutting energy is found, and the corresponding failure stresses and cutting forces are predicted with experimental validation.

To further analyze the damage states for fiber and matrix material during the chip formation, a frictional-damage mechanics model is developed. It is found that the friction in the damaged area under transverse compression can provide additional stress on the fracture plane. This friction is able to increase the shear stress on the fracture plane after the failure is initiated, and then influence the direction of the fracture plane in uncut material.

For the MD CFRP, it is found that the plies of different fiber orientation angles converge in the cutting process. An analytical model is proposed to analyze the variation of chip formation mode for each ply in the orthogonal cutting of MD CFRP. By using the minimum energy principle for all plies, the variation chip formation mode due to the interlaminar bonding effect is predicted.

Lay Summary

In machining of carbon fiber reinforced polymer (CFRP) components where the high process efficiency and surface quality are required, proper process planning such as the selection of cutting tool geometry, process parameters, and fiber orientation is necessary.

This thesis develops a mechanics model to investigate the chip formation mechanism in machining of CFRP with different fiber alignment configurations. The objective of the thesis is to understand the fiber and matrix failure type, chip formation mode, and stress state under various fiber orientations. The effect of cutting tool geometry, the friction between the tool and the workpiece, and the bonding effect among layers of CFRP are considered. In addition, the quantitative relationship between the chip formation mechanism and fiber orientation is provided. The models developed in this thesis can be used to instruct and optimize the practical machining process planning, by selecting proper fiber orientation, cutting tool geometry, and process parameters.

Preface

This thesis presents cutting mechanics models to predict chip formation mechanism, chip formation angle, and cutting forces in machining UD and MD CFRP. In addition, a new failure criterion is proposed to predict the fracture of the uncut material based on the continuum damage mechanics. All research was performed in the Department of Mechanical Engineering at The University of British Columbia under the supervision of Professor Xiaoliang Jin. The presented results in all chapters which have been published or are under review are summarized as follows:

The content of Chapter 2 reviews the existing analytical models for machining CFRPs in the literature. All existing models and relevant failure criteria are presented.

The content of Chapter 3 focuses on the chip formation process when the fiber orientation equals 0° and the failure mode is buckling. This work has been published: Song, C. and Jin, X., 2020. Shearing-buckling mechanism in orthogonal cutting of UD carbon fiber reinforced polymer. Journal of Materials Processing Technology, 280, p.116612. I was responsible for the concept formulation, simulation of the results, and experimental validation and Professor Xiaoliang Jin was involved in the concept formulation and modeling analysis. The manuscript was written by the candidate and edited by Professor Xiaoliang Jin.

The content of Chapter 4 proposes a new generalized mechanics for machining UD CFRP. This model is able to predict the chip formation mechanism, chip formation angle, and cutting forces in the fiber orientation range of $[0°, 180°]$. This work is published: Song, C. and Jin, X., 2022. Analytical modeling of chip formation mechanism in cutting unidirectional carbon fiber reinforced polymer. Composites Part B: Engineering, p.109983. I was responsible for the concept formulation, simulation of the results, and experimental validation and Professor Xiaoliang Jin was involved in the concept formulation and modeling analysis. The manuscript was written by the candidate and edited by Professor Xiaoliang Jin.

The content of Chapter 5 proposes an energy method to predict the fracture propagation direction during the UD CFRP failure process under an arbitrary 3D loading. This work has been published: Song, C. and Jin, X., 2021. Fracture angle prediction for matrix failure of carbon-fiber-reinforced polymer using the energy method. Composites Science and Technology, 211, p.108869. I was responsible for the concept formulation and simulation of the results, and Professor

Xiaoliang Jin was involved in the concept formulation, modeling, and result analysis. The manuscript was written by the candidate and edited by Professor Xiaoliang Jin.

The content of Chapter 6, as an extension of Chapter 5 to the machining process, proposes a new failure criterion to predict the fracture direction based on continuum damage mechanics using the energy dissipation method. Besides, the proposed failure criterion is implemented into the framework of the proposed cutting mechanics model. This work will be submitted to a journal publication. I was responsible for the concept formulation and simulation of the results, and Professor Xiaoliang Jin was involved in the concept formulation, model revision, and result analysis. The manuscript was written by the candidate and edited by Professor Xiaoliang Jin.

The content of Chapter 7 considers the interlaminar bonding on the chip formation mechanism variation for all plies in MD CFRP. This work has been published: Jin, X. and Song, C., 2022. Orthogonal cutting mechanics of multi-directional carbon fiber reinforced polymer with interlaminar bonding effect. CIRP Annals. I and Professor Xiaoliang Jin are responsible for the concept formulation, simulations and experimental analysis. The manuscript was written by the candidate and edited by Professor Xiaoliang Jin.

Table of Contents

List of Tables

List of Figures

List of Symbols

A_c	[mm²]	Area of chip formation plane
b	[mm]	Width of cut
d		Damage variable
d_1, d_2		Damage variable for fiber and matrix failure modes
E_a	[GPa]	Equivalent modulus
E_f	[GPa]	Fiber elastic modulus
E_t	[GPa]	Transverse elastic modulus
E_m	[GPa]	Matrix elastic modulus
E_1, E_2	[GPa]	Longitudinal and transverse elastic moduli of UD CFRP
e_{nl}, e_{nt}		In-plane and out-of-plane "internal friction"-related coefficients
e_{nl}		'Internal friction' coefficient
F_c	[N]	Resultant cutting force
F_t	[N]	Resultant thrust force
F_n	[N]	Compressive force on chip formation plane
F_s	[N]	Shear force on chip formation plane
$F_{n,i}$	[N]	Compressive force on chip formation plane of i^{th} ply
$F_{s,i}$	[N]	Shear force on chip formation plane of i^{th} ply
F_v	[N]	Compressive force on tool rake face
F_u	[N]	Friction force on tool rake face
F_{tc}	[N]	Tangential cutting force in chip formation region
F_{fc}	[N]	Thrust cutting force in chip formation region
$F_{tc,i}$	[N]	Tangential cutting force in chip formation region of i^{th} ply
$F_{fc.i}$	[N]	Thrust cutting force in chip formation region of i^{th} ply

$F_{c,b}$, $F_{c,p}$	[N]	Cutting force components in chip formation and pressing regions for buckling failure
$F_{t,b}$, $F_{t,p}$	[N]	Thrust force components in chip formation and pressing regions for buckling failure
G_{IIC}	[N/mm]	Fracture energy in the shear interface layer
G_{II}	[N/mm]	Fracture toughness under compression
G_{II}^{0}	[N/mm]	Fracture toughness without transverse compression
G_m	[GPa]	Matrix shear modulus
G_t	[GPa]	Transverse shear modulus
G_{12}, G_{13}	[GPa]	In-plane shear moduli of UD CFRP
G_{23}	[GPa]	Out-of-plane shear modulus of UD CFRP
h	[mm]	Uncut chip thickness
h_0	[mm]	Nominal uncut chip thickness
h_b	[mm]	Position of the machined surface
I_f	[mm^4]	2nd moment of area of the uncut material
I_r		Irregular coefficient
K_b		Cutting coefficient
K_t		Thrust coefficient
L_c	[mm]	Fracture region length
L_s	[mm]	Shear region length
L_{mic}	[mm]	Chip length prediction of micro buckling theory
L_{Eu}	[mm]	Chip length prediction of Euler buckling theory
ΔL	[mm]	Relative cutting displacement
P	[N]	Compressive force
P_b, σ_{mic}	[N], [MPa]	Critical force, stress for micro buckling
r	[mm]	Fiber radius

r_e	[mm]	Edge radius of insert
S_{12}, S_{23}	[MPa]	Shear strengths
S_{23}^*	[MPa]	Calculated out-of-plane shear strength for Puck's compression criterion
S_{12}^d	[MPa]	Resultant shear stress on the damaged surfaces
S_{12}^m	[MPa]	Ultimate shear strength for matrix failure mode
s_o, s_f		Damage initiation strain and complete failure strain
ΔT, ΔM		Differences between the CFRP temperature and moisture contents
t	[mm]	Workpiece thickness
V	[m/s]	Cutting speed
W_i	[J] or [N·m]	Cutting power of i^{th} ply
X_{11}^t, X_{11}^c	[MPa]	Tensile and compressive strengths in the fiber direction
X_{22}^t	[MPa]	Tensile strength in the transverse direction and shear strength
Y	[N/mm^2]	Dissipation rate of the complementary free energy density
α	[mm]	Rake angle
β	[mm]	Clearance angle
β_f	[mm]	Friction angle between rake face and uncut material
γ_c	[mm]	Damage distance
γ_m	[mm]	Fracture distance
$\varepsilon_{nt}, \varepsilon_{St}$		Shear and sliding strains on the fractured surfaces
δ	[°]	Fiber cutting angle
δ_i	[mm]	Fiber cutting angle of i^{th} ply
θ	[°]	Fiber orientation
θ_i	[°]	Fiber orientation of i^{th} ply

θ_p	[°]	Fracture angle
μ_{12}		Coulomb friction coefficient on the fractured surfaces
μ_{nl}, μ_{nt}		Coulomb friction coefficient on the fractured surfaces in the fiber and transverse directions
μ_b		Friction coefficient in chip formation region
$\mu_{b,n}$		Friction coefficient force negative rake angle
$\mu_{b,z}$		Friction coefficient force zone rake angle
μ_p		Friction coefficient in pressing region
v_p		Poisson's ratio
v_{12}, v_{13}, v_{23}		Poisson's ratios in the related directions
ζ_1^o, ζ_2^o	[mm]	Relative displacements for failure initiation of fiber and matrix modes
ζ_1^f, ζ_2^f	[mm]	Relative displacements for complete failure of fiber and matrix modes
$\boldsymbol{\sigma_{NLT}}$		Stress tensor in the transformed coordinate system
σ_{Eu}	[MPa]	Critical stress for Euler buckling
$\sigma_{c,b}$	[MPa]	Cutting stress
σ_n	[MPa]	Compressive stress on chip formation plane
$\sigma_{n,i}$	[MPa]	Compressive stress on chip formation plane of i_{th} ply
σ_{11}, σ_{22}	[MPa]	Normal stresses which are parallel to the fiber direction
$\sigma_{11,i}, \sigma_{22,i}$	[MPa]	Normal stresses which are parallel to the fiber direction of i^{th} ply
σ_{22}, σ_{33}	[MPa]	Transversely normal stresses which are perpendicular to the fiber direction
τ_s	[MPa]	Shear stress on chip formation plane
$\tau_{s,i}$	[MPa]	Shear stress on chip formation plane of i^{th} ply

$\tau_{s,i}$	[MPa]	Shear stress on chip formation plane of i^{th} ply
τ_{12}, τ_{13}	[MPa]	In-plane shear stresses which is parallel to the fiber direction
τ_{23}	[MPa]	Out-of-plane shear stress
$\tau_{12,i}$	[MPa]	In-plane shear stress which is parallel to the fiber direction of i^{th} ply
τ_f	[MPa]	Overall shear stress on the fracture plane
φ	[°]	Chip formation angle
φ_e	[°]	Chip formation angle for all plies of MD CFRP
φ_i	[°]	Chip formation angle of i^{th} ply

List of Abbreviations

CDM	Continuum damage mechanics
CFRP	Carbon fiber reinforced polymer
CZM	Cohesive zone model
EOHM	Equivalent orthotropic homogeneous material
GFRP	Glass fiber reinforced polymer
MD	Multi-directional
RVE	Representative volume element
UD	Unidirectional

Acknowledgements

Doing research in the mechanical area and finalizing Ph.D. program has been my dream since I was a primary school student.

First, I would like to thank my supervisor, Professor Xiaoliang Jin, for his rigorous research attitude, patient guidance, and questioning spirit which make my research period rather substantial. I cherish the critical thinking approaches that I learned from my supervisor, and I will continue to use them in my future work.

I am thankful to the members of AMPL, who are always kind to help me conduct the experiments. I also appreciate the support from Professor Yusuf Altintas who provided us with the experimental setup, lathe, and cutting tool during the startup phase.

Additionally, I am thankful to my supervisor, Professor Zhike Peng, from Shanghai Jiao Tong University where I got my master's degree. He gave me the chance to do research in mechanical engineering and taught me a fundamental understanding of cutting mechanics and data analysis.

Finally, I want to thank my parents for their emotional support, patience with my progress, and encouragement.

1. Introduction

1.1 Background

Carbon fiber-reinforced polymers (CFRPs) are composites consisting of carbon fibers and matrix material, and have become one of the most popular structural materials in various industries owing to the following properties: (1) The modulus and strength of CFRP can be customized in the required directions. The direction and content of fibers in the CFRP material can be customized to meet practical requirements, which provide high flexibility to design the CFRP materials with appropriate configurations to satisfy the strength requirements in different applications. (2) CFRP has a high strength-to-weight ratio. Table 1 presents the comparison of specific modulus and strength between a typical woven CFRP and aluminum alloy Al 6061-T6. It shows that the CFRP can provide equivalent strength with lower weight, which is required aerospace industry. (3) CFRP can maintain the same performance under glass transition temperature [1,2]. The maintenance of the material's mechanical behaviour under various working temperatures is an important index to evaluate its applications. The mechanical behaviour of the CFRP materials is almost constant under the glass transition temperature (between $120°\mathrm{C}$ and $210°\mathrm{C}$). Therefore, CFRP has been used as the wing spars and racing car body structure (Airbus A350 XWB). (4) The thermal conductivity of CFRP is relatively low, which is typically $5-8\,\mathrm{W/(m\cdot K)}$ in the in-plane direction and $0.5-0.8\,\mathrm{W/(m\cdot K)}$ in the transverse direction [3,4]. On the other hand, the thermal conductivity of aluminum is $162-253\,\mathrm{W/(m\cdot K)}$ [5]. This property makes CFRP material suitable for aerospace structural components requiring thermal insulation. (5) CFRP processes comparably small thermal expansion. For example, the thermal expansion coefficient of CFRP components is one-sixth of the aluminum 6061-T6 and one-third of the stainless steel 304 [6]. The small thermal expansion is beneficial for reducing stress at the joint in the assembled components under varying temperatures.

Table 1.1 Mechanical property comparison of woven CFRP (provided by the manufacturer) and Aluminum 6061-T6.

Mechanical properties	Woven CFRP (55% fiber content)	Aluminum 6061-T6
Density	1700 kg/m^3	2700 kg/m^3
Elastic modulus	70.0 GPa	68.9 GPa
Tensile strength	600 MPa	310 MPa

The unique mechanical properties make CFRP materials suitable to be used as structural components of sporting goods, vehicles, and airplanes (see Fig. 1.1). For example, in the aerospace industry, the usage of CFRP components has reached a weight ratio of over 50% for both Airbus A350 XWB and Boeing 787.

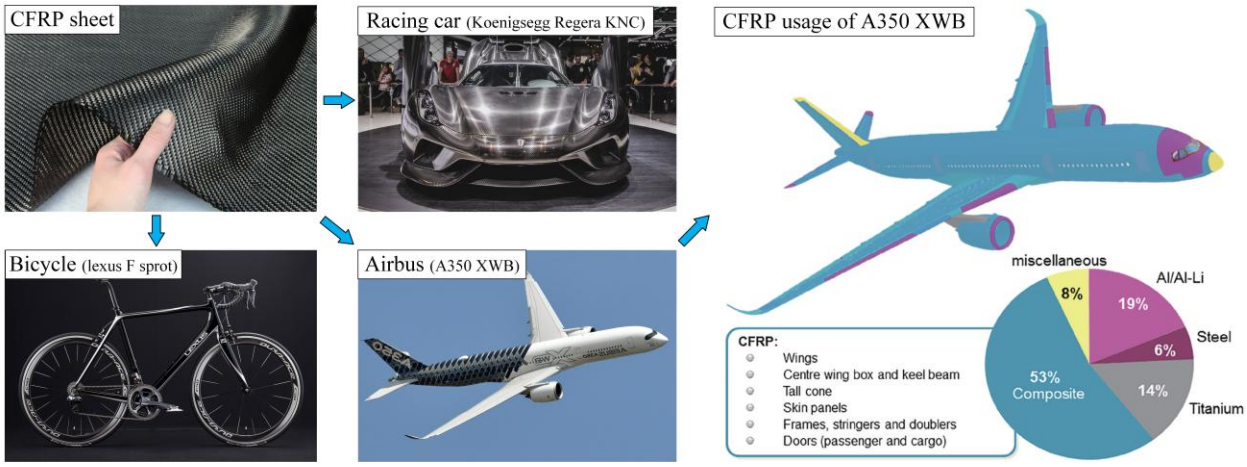

Figure 1.1 CFRP material applications. (Websites of Lexus, MotorBiscuit, and Airbus Technical magazine)

To support the external loading from different directions, four types of CFRP prepregs are produced in the industry: unidirectional (UD) CFRP, multi-directional (MD) CFRP, woven CFRP, and 3D orthogonal woven CFRP [7], with their layout configurations shown in Fig. 1.2. The first two types use the UD prepreg and stack in one or several directions to bear the loadings in specific directions. The woven CFRP is produced using the weave approach like clothes. The 3D woven CFRP adds fiber bundles to provide additional resistance to bear the loading in the transverse direction.

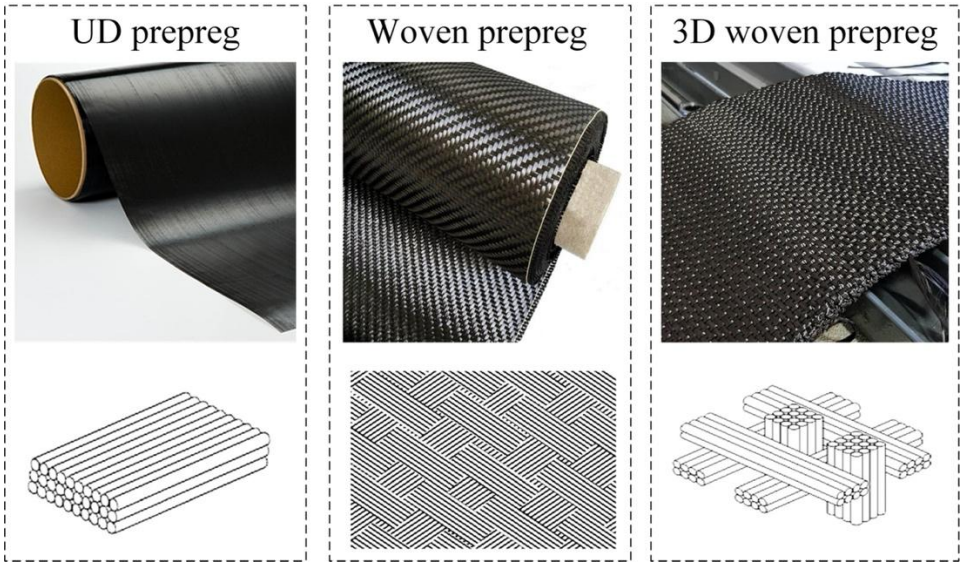

Figure 1.2 CFRP categories and internal structure [7].

1.2 Machining of Carbon Fiber Reinforced Polymer

The CFRP prepregs need to be laid up in a mould with the matrix material, and cured under pressure to produce the parts with the required thickness and shape. The machining operations (see Fig. 1.3) such as edge trimming, drilling, and slot milling are needed for fiber burr removal, hole making, or part assembly. However, different from metal cutting, the machining of CFRP is highly influenced by the anisotropy and inhomogeneity of the material [8], that is, the chip formation process is dependent on the selected fiber orientation and cutting parameters. The first challenge related to the machinability of CFRP components is the occurrence of delamination for the top and bottom plies [9]. The initiation of the delamination is related to the chip formation mechanism, fiber orientation, tool wear state, and cutting parameters. In the machining process, the delamination occurs in the form of uncut fibers and fiber bundles on the top and bottom plies of CFRP parts, which can propagate along the fiber direction. The delaminated parts cannot be completely repaired, which can lead to high machining costs if the process condition is not properly selected. Another challenge is the severe machined surface or subsurface damage at specific fiber orientations. The subsurface damage in the form of matrix fracture, fiber breakage, and debonding can propagate by several millimeters depth under the machined surface [10]. Meanwhile, the mechanical strengths of the material decrease substantially due to the growth of the subsurface damage under external loadings. The third challenge in the machining of CFRP is fast and severe tool wear. Abrasive tool wear may occur after 2-3 meters of cutting length. The change of tool

edge geometry due to wear progression leads to delamination and severe subsurface damage. All the challenges mentioned above are related to the failure of CFRP material in the chip formation region in the machining process. Therefore, to improve the machining performance for CFRP, it is essential to understand the failure mechanism of fiber and matrix material due to the material removal process in machining, and its quantitative relationship with the fiber orientation and cutting parameters.

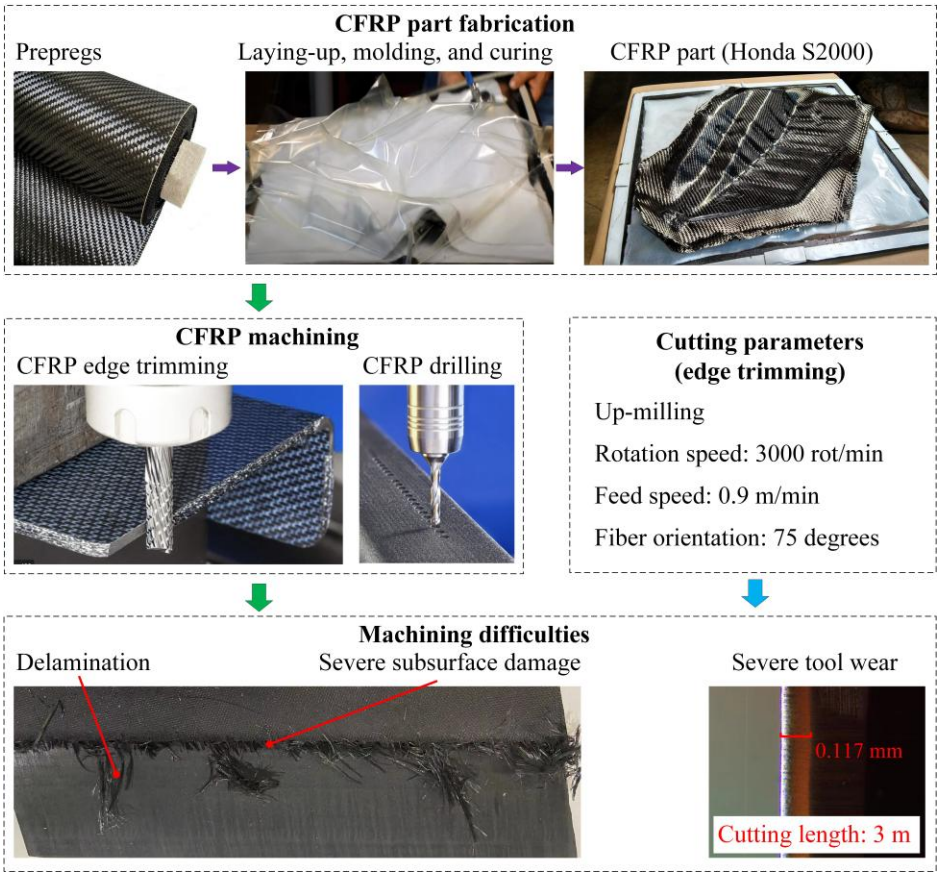

Figure 1.3 Manufacturing process of CFRP parts and machining difficulties. (CFRP fabrication: The Fab Forums, CFRP machining: SEM website by contribution editor Jim Lorincz)

1.3 Experimental investigation and modeling of CFRP chip formation mechanism

The existing investigations of the chip formation mechanism for machining CFRP are mainly based on experimental observation [11-14] and finite element analyses [15,16]. The variation of chip formation mechanism with respect to the fiber orientation is discussed and divided into three ranges: matrix shearing failure in the fiber orientation range of $[0°, 90°]$, fiber bending failure in the fiber orientation range of $[90°, 180°]$, and fiber buckling when the fiber orientation is equal to $0°$. However, the reason for the chip formation mechanism transition is not discussed in terms

of the stress state in the uncut material, because the interaction between the normal and shear stresses cannot be experimentally measured. In addition, the material fracture direction of the uncut material defined by the chip formation angle is not explained. Another challenge in experimentally examining the chip formation modes or the material fracture in machining CFRP is that the formed fracture plane is full of broken fibers and crushing matrix material. In addition, the failure of CFRP material starts from the micro cracks owing to the material defects, stress concentration, and debonding of the interface layer between the fiber and the matrix. The failure initiation occurs inside the CFRP material, while the on-site experimental observation can only be performed from the side of the workpiece. Therefore, the fracture initiation and propagation which influence the chip formation mode in machining CFRP can not be directly examined through experiment. The main problem for finite element modeling is the high computational cost. In addition to the element distortion, the modeling accuracy is highly affected by the element size.

One of the measurable quantities, which are determined by the chip formation mechanism, is the cutting force. The measurements of the cutting force show an apparent variation with the fiber orientation. Considering that the tangential and feed cutting forces are the projections of the forces on the fracture plane, they can be used to evaluate the failure stresses of the uncut material. Also, the chip formation angle of uncut material can be obtained by examining the orientation of the chip formation plane with respect to the cutting direction, and it determines the projection angle of the cutting force to the fracture plane. To the best of my knowledge, all existing analytical models aim to predict the cutting forces with the pre-defined chip formation mechanism obtained by the experimental study. The chip formation mechanism and its variation have not been discussed in existing analytical models.

1.4 Thesis Objectives

The objectives of this thesis are to propose an analytical cutting mechanics model to investigate the chip formation mechanism and its transition with the fiber orientation for UD and MD CFRPs in orthogonal cutting. The measurable quantities such as cutting forces and chip formation angle are used to validate the proposed models. The specific aims of the thesis to achieve the objective include the followings:

(1) capture the uncut material deformation and chip formation when the material fails due to the buckling at 0° fiber orientation;

(2) determine the quantitative relationship among the chip formation mechanism, fiber orientation, and cutting parameters in the entire fiber orientation range;

(3) investigate the effect of damage propagation in matrix material on the chip formation mechanism;

(4) model the interlaminar bonding effect on the chip formation in machining MD CFRP.

1.5 Thesis Structure and Flow

This thesis is structured as follows: Chapter 2 presents a literature review on the existing cutting models of UD CFRP, including finite element models, analytical mechanics models, and fiber deflection models. Chapter 3 proposes a shearing-buckling mechanism for cutting UD CFRP when the fibers are oriented in the cutting directions. In Chapter 4, a cutting mechanics model is proposed to predict the chip formation mechanism and its variation with the fiber orientation. Chapter 5 proposes a new fracture angle prediction model using the energy method which is extended to the cutting mechanics model to investigate the effect of micro crack propagation on the chip formation in Chapter 6. In Chapter 7, the interlaminar bonding between plies with different fiber orientations is discussed and modeled for cutting of MD CFRP. The conclusions of this thesis and the future research direction are given in Chapter 8. The flowchart of this thesis is summarized in Fig. 1.4.

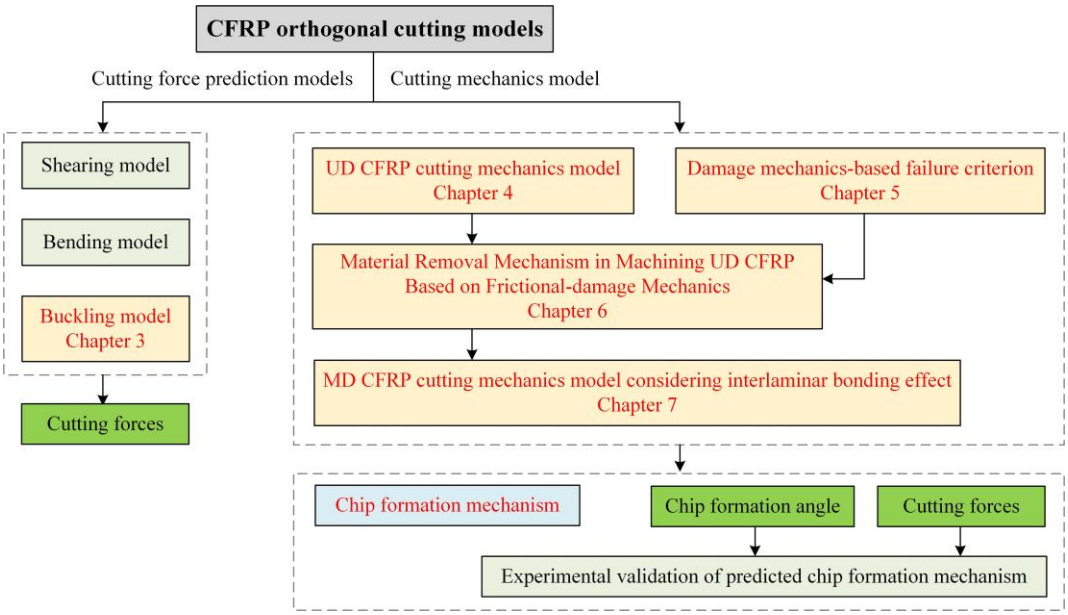

Figure 1.4 Thesis flowchart.

2. Literature Review

This chapter focuses on the literature review on state of the art in experimental studies and modeling of the machining of CFRP. First, the experimental studies which investigate the chip formation mechanism are presented. Then, the existing CFRP cutting models including finite element models, discrete element models, and analytical models are discussed. Moreover, because this thesis presents a CFRP cutting mechanics model based on continuum mechanics, the failure criteria of CFRP and the relevant failure mode under arbitrary mechanical loading are presented.

2.1. Experimental studies of CFRP cutting

Since the manufacturing process for CFRP is developed and patented in the 1960s, researchers have started to analyze its machinability using orthogonal cutting methods [11]. The earliest experimental investigation (see Fig. 2.1) of the fundamental material removal mechanism was conducted by KoPlev et al. [12]. They used an orthogonal cutting setup and UD CFRP workpiece with the fiber orientation parallel and perpendicular with respect to the cutting direction. The cutting forces and chip geometry at various uncut chip thicknesses were analyzed. It was found that the machined surface was more smooth for the parallel cutting whose failure was initiated at the interface layer. For the perpendicular cutting, the formed chips were always in block-like shape. Wang et al. [13] conducted orthogonal cutting experiments for UD CFRP in the entire fiber orientation range of $[0°, 180°]$. To understand the variation of chip formation mechanism with the fiber orientation, the cutting forces and morphology of the machined surface were examined. By considering the dominant force applied by the cutting rake face, the chip formation mechanism is categorized as (1) delamination for $0°$ fiber orientation and positive rake angle, (2) fiber buckling for $0°$ fiber orientation and nonpositive rake angle, (3) fiber cutting for fiber orientation range of $[0°, 90°]$, (4) deformation for $90°$ fiber orientation, and (5) shearing for fiber orientation range of $[90°, 180°]$. This work was then extended to MD CFRP [14] whose stacking sequence used was $[0°/90°/45°/135°]$ and chip formation mechanism is affected by the interlaminar bonding. It was found that the chip formation mechanisms for $90°$ and $135°$ plies changed owing to the interlaminar bonding effect, while the chip formation mechanisms for the other two plies remained the same.

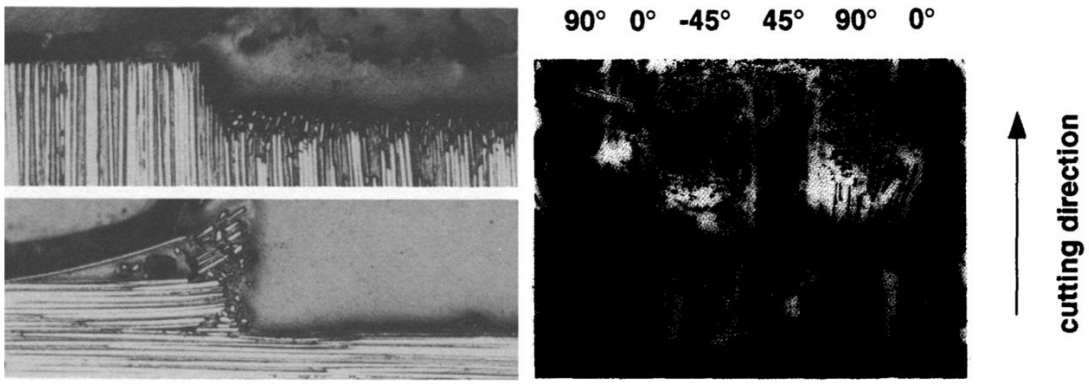

Figure 2.1 Experimental studies of orthogonal cutting of UD [12] and MD [14] CFRPs.

2.2. Existing CFRP cutting models

The mechanics models of cutting CFRP have been developed to capture the chip formation mechanism or cutting forces, classified into two categories: (1) finite element models which focus on the stress distribution by assuming CFRP workpiece as an equivalent homogeneous material (EHM) in macro-scale, or modeling the deformations and failures of fiber, matrix, and interface separately in micro-scale as shown in Fig. 2.2; (2) analytical models which aim to predict the cutting forces based on pre-assumed material deformation and chip formation modes [15]. The detailed literature work and discussions on both modeling techniques are discussed as follows.

The early finite element studies treated the CFRP workpiece as macro-scale anisotropic and homogeneous material whose moduli can be calculated based on the EHM simplification. Arola and Ramulu [16] pioneered the finite element analysis of cutting UD CFRP to predict the cutting forces. The effects of fiber orientation and tool geometry on the stress distribution in the deformed CFRP material were analyzed. Besides, the tangential cutting forces were predicted and compared with the models using the maximum stress criterion and Tsai-Hill criterion [17,18]. Ramesh et al. [19] conducted Lagrangian formulation-based transient elastoplastic finite element analysis for orthogonal cutting of fiber-reinforced polymers (FRPs) in the entire fiber orientation range. It was shown that the plastic strain was negligible and the chip formation was dominated by the matrix shear failure. Mahdi and Zhang [20,21] estimated the mechanical properties for the EHM equivalent of CFRP based on the fiber and matrix properties individually [22]. It was shown that the use of Tsai-Hill criterion can increase the force prediction accuracy under the plane stress condition. In addition, various meshing strategies were compared to improve the force prediction accuracy. Arola et al. [23] introduced a critical nodal stress criterion to simulate the CFRP

trimming process when fiber orientation is in the range of $[0°, 90°]$. They found that the sub-surface damage increased with the fiber orientation and the best surface quality was achieved when the tool rake angle is $10°$. Lasri et al. [24] compared various CFRP failure criteria, including the maximum stress, Hashin's and Hoffman's criteria regarding the prediction accuracy of cutting forces and sub-surface damage. All of the three failure criteria achieved the prediction of the tangential cutting forces with acceptable accuracy, although apparent errors were observed for the thrust force predictions. In addition, it was noted that the sub-surface damage was strongly influenced by the fiber orientation, and the minimum sub-surface damage was achieved when the fiber orientation is $30°$.

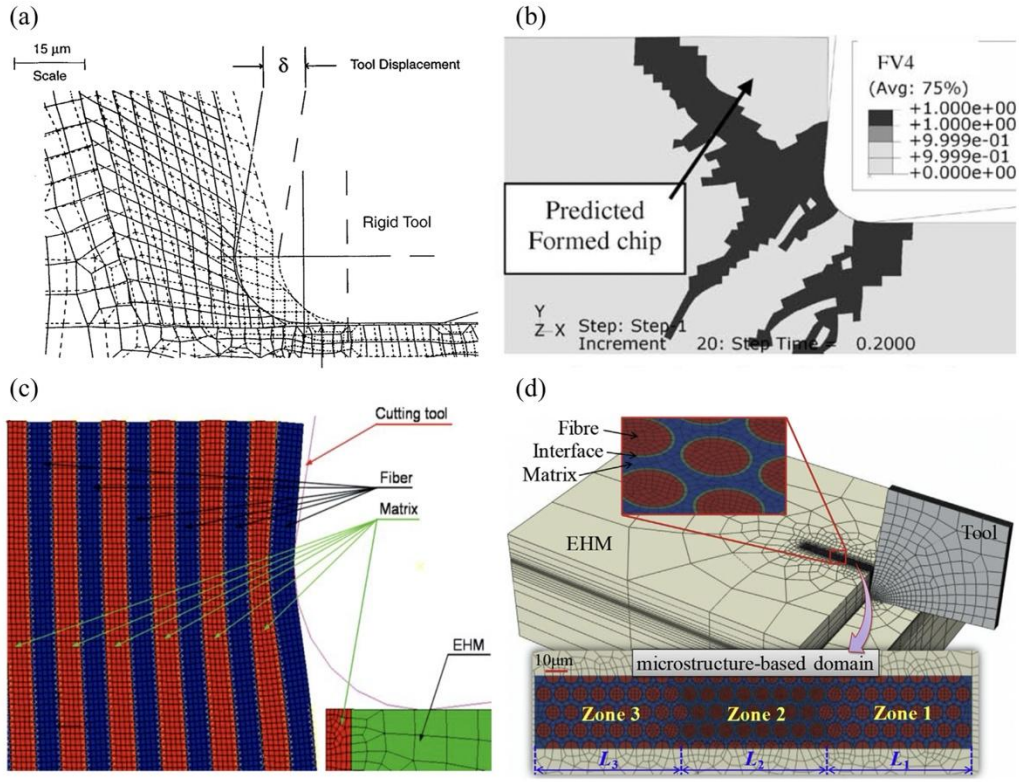

Figure 2.2 Macro scale and micro-scale finite element models. (a) [23], b [24], (c) [27], and d [35].

The micro-scale finite element models, which can capture the deformation of fibers and matrix individually, became popular owing to the rapid development of computational capability. Nayak et al. [25] modeled the cutting operation with $90°$ fiber orientation considering the transverse compression failure of a single fiber attached to an elastic half-space. The sub-surface damage caused by the fiber-matrix debonding was modeled using the cohesive zone model (CZM). Nayak et al. [26] extended this micro-scale model to the fiber orientation range of $[0°, 90°]$. The

quantitative relationships between fiber orientation, tool geometry, sub-surface damage depth, and cutting forces were analyzed. Rao et al. [27] proposed a two-phase micro-mechanical model in the fiber orientation range of $[0°, 90°]$ based on elastic fiber and elastoplastic matrix assumptions. It was shown that the failure modes of fiber, matrix, and fiber-matrix interface were dominated by fiber orientation. The tangential cutting forces were predicted with high accuracy, but an opposite trend was observed between the predictions and experimental results for thrust force. Mkaddem et al. [28] combined the advantages of micro-scale and macro-scale models by using an adaptive mesh strategy and equivalent orthotropic homogeneous material (EOHM) approach to predict the cutting forces. The sensitivity of cutting forces with respect to fiber orientation, tool rake angle, and uncut chip thickness was analyzed. Dandekar and Shin [29] proposed a multiphase finite element model to simulate the fiber-matrix interface debonding and fiber pull-out. Furthermore, the debonding effects that occurred at the front and rear faces of the deformed fibers were considered to achieve better force prediction results. Galzada et al. [30] focused on the tensile and compressive failures of the fiber-matrix interface, which was meshed using continuum elements with near-zero thickness. Based on continuum damage mechanics (CDM), the fiber-matrix interfacial failure was characterized using an exponential law. This model revealed the relationships between the chip formation modes and the fiber orientation, and the effect of tool rake angle on chip formation was considered. This model achieved accurate predictions of the cutting and thrust forces. Abena et al. [31] modeled the fiber-matrix interface as finite thickness element, zero thickness, and surface element, respectively. The tangential cutting forces were predicted with acceptable accuracy, even though the thrust forces were underestimated. Yan et al. [32] studied the energy dissipating mechanism in the orthogonal cutting of UD CFRP, and analyzed the sensitivity of the simulated fiber deformation with respect to the fiber stengths and friction coefficient. Xu et al. [33] proposed a three-dimensional model to simulate the chip formation mode and surface quality in the elliptic vibration-assisted cutting process. It was found that the elliptic vibration assistance achieved smoother surface quality compared to traditional cutting. Xu and Zhang [34] characterized the surface topography of the machined surface and showed that the elliptic vibration assistance resulted in smaller sub-surface damage depth. Xu and Zhang [35] extended their three-dimensional model to include the effect of heat on the chip formation mode. It was shown that the mechanical properties of CFRP material were influenced by the heat generated at the tool edge. Xu and Jin [36] considered the effects of oblique cutting

angle in the three-dimensional model when the fiber orientation is in the range of $[0°, 90°]$. The effect of the out-of-plane force owing to the oblique cutting edge on the chip formation process was analyzed.

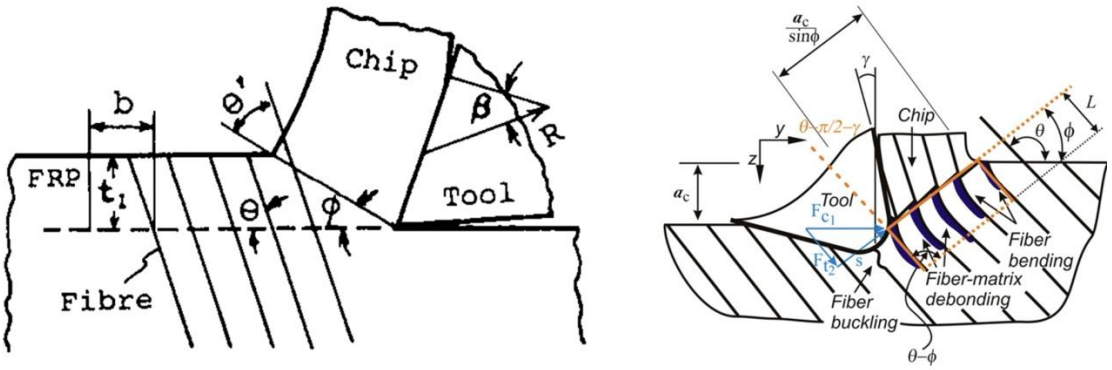

Figure 2.3 Analytical models for orthogonal cutting of UD CFRP [38, 45].

Analytical methods have also been used to develop the quantitative relationship between the cutting forces and the process parameters in orthogonal cutting of UD CFRP owing to its high computational efficiency, as shown in Fig. 2.3. Because the chip formation of CFRP [37] is strongly dependent on fiber orientation, the existing analytical models focus on force prediction by pre-defining the chip formation modes from experimental observations at different fiber orientation ranges. When fiber orientation is in the range of $[0°, 90°]$, the chip formation mode is assumed to be the shear failure. Takeyama and Iijima [38] proposed a mechanics model for cutting glass fiber reinforced polymer (GFRP) by treating the shear strength as a function of shear angle based on the shear tests. Through the identification of the shear strengths with various fiber orientations, the tangential and thrust forces were predicted using the minimum energy principle for $[0°, 90°]$ fiber orientation range [39]. Bhatnagar et al. [40] predicted the cutting forces assuming that the shear angle is equal to the fiber orientation, and the chips were formed due to the shear failure in the matrix layer. Zhang et al. [41] considered the geometry of the cutting edge and proposed three sub-models to predict the force components in three defined material deformation regions. Considering the brittle property of the CFRP material, the cutting forces were predicted assuming that the material compression ratio is equal to unity. Xu and Zhang [42] modeled the deformation of a single fiber in contact with the cutting tool edge, and predicted the cutting forces based on the beam-on-foundation theory. Bending failure was treated as the chip formation mode when the fiber orientation was $90°$. Puw and Hocheng [43] modeled the uncut

material as a cantilever beam subjected to the concentrated transverse loading at the sharp cutting edge. Xu and Zhang [44] modeled the fiber as a beam on an elastic foundation, and the deflection of the fiber was predicted to quantitatively analyze the surface quality. When the fiber orientation exceeds 90°, the effect of out-of-plane shear enlarges. Sahraie Jahromi and Bahr [45] developed an energy-based method to predict the cutting forces. The concept of representative volume element was introduced to predict the cutting forces in the deformation area. Buckling becomes the dominant chip formation mode when fibers are parallel to the cutting direction. Puw and Hocheng [43] modeled the uncut material as a cantilever beam with one end fixed and the cutting forces were predicted based on Euler buckling theory. Qi et al. [46] modeled the deflection of the single fiber surrounded by the matrix using the representative volume element (RVE) proposed by Jahromi and Bahr [45], and the chip formation mechanisms in different deformation areas were considered. Chen et al. [47] proposed three models to predict the cutting forces based on beam-on-foundation theory and the RVE method. Based on the micro buckling theory, Voss et al. [48] predict the chip formation and cutting force by adding up the force components in three deformation regions. Song and Jin [49] analyzed the periodic buckling failure process based on the energy method for zero fiber orientation. The nonlinear relationship between the chip lengths and the cutting forces was modeled.

2.3. Fundamental CFRP material failure criteria

Material failure occurs to form the chip in the machining process. Different from metal cutting in which shearing is the only failure mode, the failure criterion of CFRP is influenced by fiber and matrix, and is also direction-dependent. Over 50 failure criteria and their modification editions have been proposed since the 1960s to investigate and predict the structural performance of the CFRP components under complex loadings, such as fatigue, low-speed impact, and high-speed impact [50, 51]. In this thesis, I select the representative criteria, which have been widely used or implemented in commercial analyses package, to review their evolution of prediction accuracy.

The framework of CFRP failure criteria was originally from the yield criterion of a general orthotropic plastic material proposed by Hill [52] in 1948. By assuming that the superposition of the hydrostatic stresses does not affect the yield criterion of the transversely orthotropic material, he proposed a quadratic equation which is able to consider the interactive effect between the normal and shear stresses. The coefficients of all terms in the equation are related to characteristic

constants of the anisotropy. By citing Hill's failure criteria framework, Tsai [53] proposed a widely used failure criterion named 'Tsai-Hill', whose coefficients of all terms in the criterion equations can be experimentally determined. It achieved a smooth elliptical failure envelope in the stress coordinate to represent the stress states under failure condition. However, the predicted failure stresses are more conservative because the isotropic normal stresses are neglected. By assuming that the CFRP material is brittle, Hoffman [54] extended the 'Tsai-Hill' failure criteria by adding three terms which are proportional to the normal stresses in three orthogonal directions. Moreover, the differences between the compressive and tensile failure stress under three-dimensional loading conditions can be predicted. For the same purpose, Tsai and Wu [55] generalized the 'Tsai-Hill' criterion, which is able to include the interactive effect between stress and strength, and distinguish the tensile and compressive failure strengths.

To further distinguish the failure mode initiated by fiber and matrix, a new framework was proposed by Hashin and Rotem [56] in 1973, which defined the CFRP material failure mode as fiber tension, fiber compression, matrix tension, and matrix compression. The matrix compression is initiated by the micro cracks in the matrix, therefore, is also described as matrix shear under compression. This work proposed a quadratic failure criterion which can achieve a smooth transition between the tension and compression modes of the matrix under plane stress conditions. The interaction between the normal and shear stresses resulting in the matrix failure was discussed. For the fiber failure modes, the normal tensile and compressive stresses in the fiber direction caused fiber tension and fiber buckling (or micro buckling), respectively. This model was then extended to the three-dimensional case by Hashin [57], and could predict the enhancement effect of compressive stress on the shear stress. Besides, the shear stress was included in the fiber failure criterion which achieves higher prediction accuracy for the fiber failure mode. In this work, Hashin also developed a simple form for the matrix failure mode from the soil mechanics, but could not provide a physical explanation for predicting the fracture angle. Puck and Schürmann [58] used the Coulomb friction theory to explain that the 'internal friction' increases the shear strength. Even though the physical explanation can not be given, their failure criteria can achieve accurate prediction for fracture angle and include the increase of the shear strength by introducing an enhancement factor under transverse compression.

Based on the literature review, the existing models focused on the cutting force prediction using the pre-defined chip formation mechanism. However, the more fundamental problem, that

is, the prediction of the chip formation mechanism with various fiber orientations is not solved. In addition, the actual fracture plane can not be determined using the present cutting force prediction models. Following this explanation, this thesis aims to investigate the chip formation mechanism in machining UD and MD CFRPs using analytical methods, and the cutting forces and fracture direction of uncut material are experimentally measured to validate the chip formation model. Four failure modes defined by Hashin et al. [57] under general loading, are used to categorize the fracture pattern of the uncut material.

3. Shearing-buckling Mechanism in Orthogonal Cutting of Unidirectional CFRP at 0° Fiber Orientation

In this chapter, a new analytical model is proposed, including the shearing-buckling mechanism of the CFRP material to characterize the chip formation process in orthogonal cutting with 0° fiber orientation. The deformations of CFRP material in the chip formation region and tool pressing region are considered. In the chip formation region, the shearing deformation and fracture process at the shear interface layer caused by the relative sliding of the fibers is modeled. The uncut material keeps straight until the initiated fracture in the shear interface layer is long enough to activate either the Euler buckling or micro buckling of the uncut material. The machined chip length is then predicted as a function of the cutting parameters and the mechanical properties of the CFRP material. For the pressing region, the tool-workpiece contact force is obtained by treating the tool edge and flank face as a tilted indenter on the elastic half-space. The resultant cutting forces are predicted as explicit nonlinear functions of the uncut chip thickness, which are not available in the literature to my best knowledge. The predicted cutting forces and chip lengths are validated by experimental results from orthogonal cutting experiments on CFRP at different uncut chip thicknesses.

3.1. Cutting mechanics model for buckling failure

In order to investigate the buckling failure mechanism in the orthogonal cutting process of UD CFRP, the fiber orientation is adjusted to be parallel to the cutting direction, and the cutting tools with zero and negative rake angles are used. The setup of orthogonal cutting and its schematic representation are shown in Fig. 3.1. As the cutting tool moves forward, the tool keeps pressing the material, and the deformation region includes chip formation region in front of the tool rake face, and pressing region below the tool round edge, as shown in Fig. 3.2. The material in the chip formation region breaks and forms irregular contact surfaces which is the typical phenomenon of buckling failure due to longitudinal compression as explained by Wang et al. [13]. In the pressing region, the material bends along the round edge under transverse compression with elastic deformation, then bounces back and stays in contact with the flank face. Due to the bouncing-back effect, the nominal uncut chip thickness (h_0) is the summation of the real uncut chip thickness (h) and the bouncing back depth (h_b), as shown in Fig. 3.2.

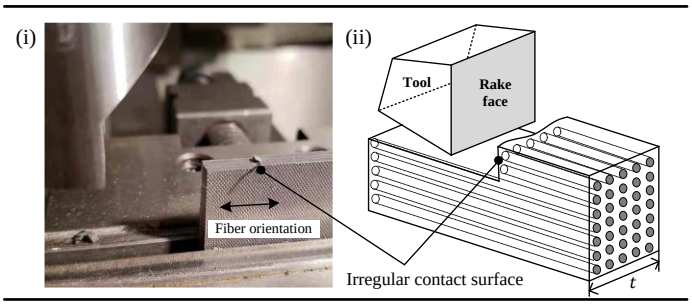

Figure 3.1 Cutting process and its schematic representation.

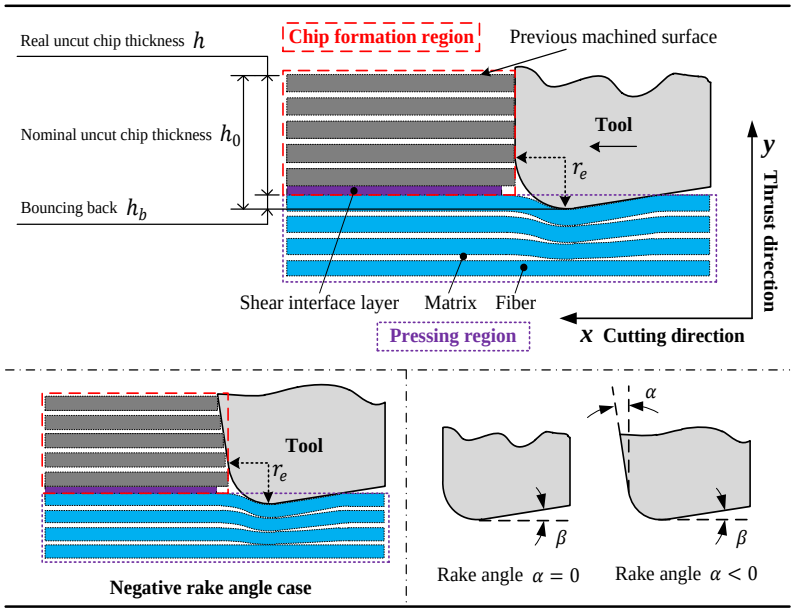

Figure 3.2 Chip formation region and pressing region.

3.2. Shearing-buckling mechanism in chip formation region

3.2.1. Modeling of shearing process

The uncut CFRP materials in the chip formation region experience three different deformation modes consecutively due to the longitudinal compression by the tool rake face: shearing, buckling, and bending-fracture.

As shown in Fig. 3.3, the material in front of rake face is under longitudinal compression, but has not buckled yet. Shearing occurs at the interface layer, which is located between the chip formation region and the tool pressing region. Since the real uncut chip thickness is much smaller compared to the remaining length of the uncut material in horizontal direction, the compression stress (σ) at the tool-workpiece interface in the longitudinal direction is assumed to be uniformly

distributed, and the CFRP material in the chip formation region is assumed as a long sheet with one-side constraint as explained by Nusayr and Paslay [59], as shown in Fig. 3.3. During this shearing process, the compressive stress continues increasing monotonically due to the compressive resistance of the sheet and shearing resistance of the shear interface layer. Once the relative sliding displacement reaches beyond the fracture limit of the material, mode II fracture is initiated at the shear interface, and the shear interface layer is composed of fracture zone with length L_c and shearing zone with length L_s. The purpose of the proposed shearing model is to build a bridge between the shearing process and the buckling process.

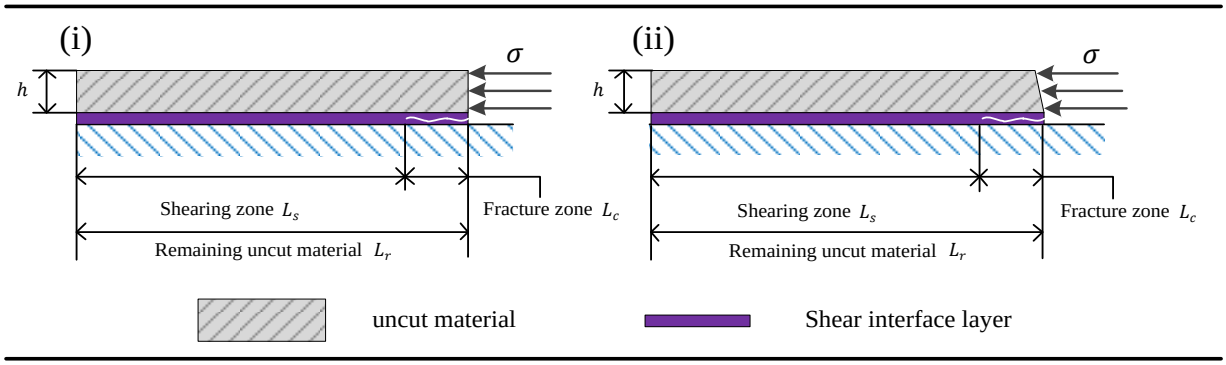

Figure 3.3 Shearing and fracture zones in shear interface layer.

To model the shearing-fracture process, the triangular type cohesive law is used to obtain the shear stress near the macro crack tip, as shown in Fig. 3.4(i). The shear softening behaviour after the elastic shear deformation period is mainly caused by the microcracks formed in the interface layer and the mechanical property of the workpiece material, as explained in the experimental study of CFRP fracture by Bradley [60]. The shear stress decreases to zero when the fracture initiates and grows inside the interface layer. The force equilibrium equation in the longitudinal direction for the workpiece material in the chip formation region is expressed as

$$\frac{dP}{dx} - \tau t = 0 \tag{3.1}$$

where P is the compressive force, t is the width of the workpiece and τ is the shear stress provided by the shear interface layer due to the longitudinal compression. The fracture region occurs and enlarges when the compressive stress reaches beyond a critical value determined by the shearing of the interface layer and the compression of the uncut material, resulting in interface layer fracture

with length of L_c, as shown in Fig. 3.4(ii). Since the shearing resistant capacity only exists in the shearing zone, Eq. (3.1) is updated to include the different stress states in the uncut material

$$\begin{cases} \dfrac{dP}{dx} - \tau t = 0 & \text{shearing zone} \\ \dfrac{dP}{dx} = 0 & \text{fracture zone} \end{cases} \tag{3.2}$$

When the cutting tool continues to move forward, the resistant capacity provided by the shear interface does not change due to the long sheet assumption, with the proof provided in Appendix A. Therefore, the compressive force (P) remains constant during the fracture growth process.

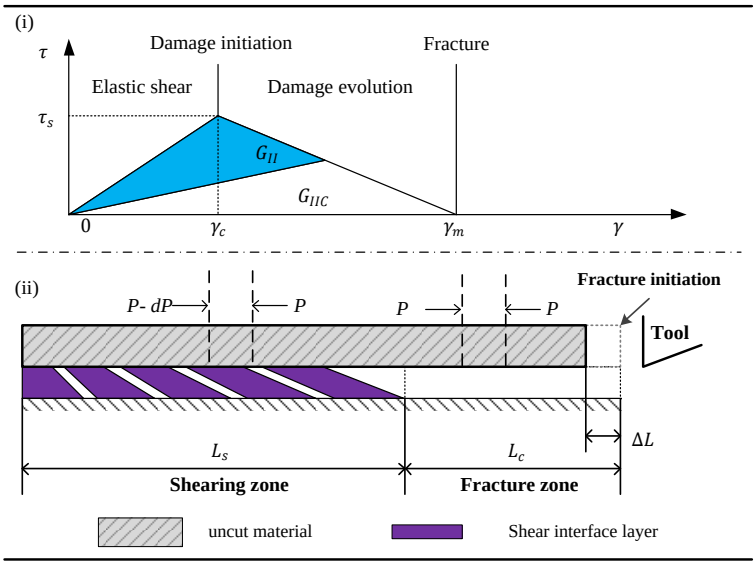

Figure 3.4 Triangular type cohesive law and shearing process.

To determine the maximum compressive force in this process, the work done (ΔW) by the constant compressive force is

$$\Delta W = P\Delta L \tag{3.3}$$

where ΔL is the relative displacement of the cutting tool during the fracture process as shown in Fig. 3.4(ii). The external work is converted to the strain energy (ΔN) inside the uncut material and energy (ΔS) to create the new fracture surfaces in the shear interface layer, which are given as

$$\Delta N = \frac{E_a \varepsilon^2}{2} thL_c \tag{3.4}$$

$$\Delta S = G_{IIC} tL_c \tag{3.5}$$

where G_{IIC} is the mode II fracture energy at the interface layer, h is the real uncut chip thickness, and ε is the normal strain with $\varepsilon = \Delta L / L_c$. According to Steif [61,62], the equivalent longitudinal elastic modulus (E_a) of the uncut material is determined by

$$E_a = E_f v_f + E_m (1 - v_f) \tag{3.6}$$

where v_f is the fiber content, E_f and E_m are the moduli of fiber and matrix respectively.

Correspondingly, the energy balance equation is expressed as

$$\Delta W = \Delta N + \Delta S \tag{3.7}$$

Substitute Eqs. (3.3)-(3.5) into Eq. (3.7), it is obtained that

$$P\Delta L = \frac{E_a \varepsilon^2}{2} thL_c + G_{IIC} tL_c = \frac{E_a \Delta L^2}{2L_c} th + G_{IIC} tL_c \tag{3.8}$$

Based on Eq. (3.8), the maximum compressive force is obtained

$$P = t\sqrt{2E_a G_{IIC} h} \tag{3.9}$$

Correspondingly, the relationship between the maximum compressive stress (σ_b) and the real uncut chip thickness (h) is obtained as

$$\sigma_b = \sqrt{\frac{2E_a G_{IIC}}{h}} \tag{3.10}$$

According to Eq. (3.9), the maximum compressive force in orthogonal cutting of CFRP is proportional to the square root of the real uncut chip thickness. The coefficient for the cutting force-real uncut chip thickness relationship is dependent on the width of the workpiece, the equivalent elastic modulus of the uncut CFRP material, and Mode II fracture energy at the interface

layer. Since the uncut material above the fracture zone is treated as a cantilever beam whose length (L_c) increases during the fracture propagation in the shear interface layer, the critical stress which is required for the buckling initiation continues decreasing. However, the compression stress (σ_b) is a constant due to the limited resistant capacity of the material during the fracture growth process. Thus, once the fracture length (L_c) is long enough to activate either micro buckling or Euler buckling of the uncut material which are main failure modes under longitudinal compression, the uncut material bends and breaks into chips. The details of the buckling of uncut material and chip formation are discussed in the next section.

3.2.2. Material buckling and chip formation

Rosen estimated the critical stress of micro buckling for UD fibrous composite plate under longitudinal compressive loading [63]. According to the two micro buckling modes he proposed, the fibers can buckle in phase (shear mode) or out of phase (extensional mode). Considering the internal imperfections of the UD CFRP material, the micro buckling is initiated due to the combined effects of these two modes. However, orthogonal cutting experiments of UD CFRP by Puw and Hocheng [37] showed that the machined chips are mainly in crumbled form, which suggests that the in-phase deflection (shear mode) dominates the buckling process. In fact, the shear mode is also the principal failure mode of UD CFRP under longitudinal compression tests with a wide range of fiber-matrix combinations as presented by Hahn and Sohi [64], since fiber separation (the results of extensional mode) is not observed.

Steif et al. [61] proposed a three-dimensional model for the prediction of the critical compression stress of fibers failing in micro buckling mode. According to the in-phase deformation assumption, a free body diagram of single fiber is shown in Fig. 3.5. M_b and V_b are the bending moment and shear force occurring at both ends of the fiber, P_b is the longitudinal compressive force, and τ_b is the shear stress provided by surrounding matrix.

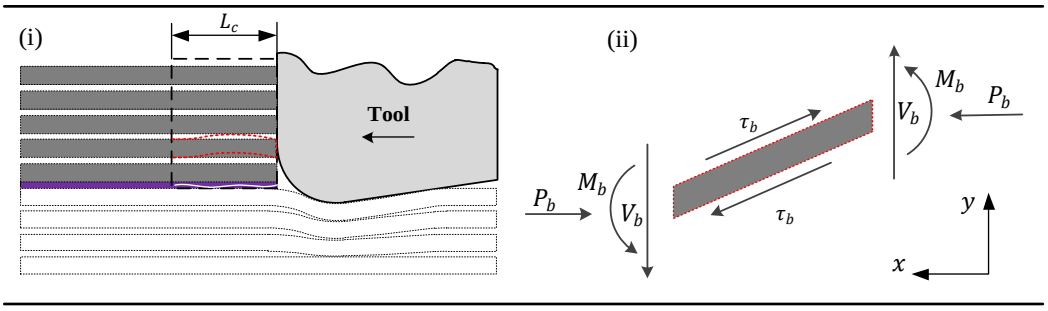

Figure 3.5 Schematic representation and fundamental element of micro buckling model.

Based on the moment balance condition, the equilibrium equation for an element of the fiber is governed by

$$E_f I_f \frac{d^4 u_y}{dx^4} + P_b \frac{d^2 u_y}{dx^2} - \pi r^2 G_m \frac{d^2 u_y}{dx^2} = 0 \tag{3.11}$$

where E_f is the fiber elastic modulus, I_f is the moment of inertia of the fiber, r is the fiber radius, and u_y is the transverse displacement.

The solution of transverse displacement (u_y) for Eq. (3.11) is in the form of

$$u_y = A_1 sin\left(\frac{\pi}{L_c} x\right) \tag{3.12}$$

where L_c is approximated by the fracture length formed in the shearing process.

By substituting Eq. (3.12) into Eq. (3.11), it is obtained that the longitudinal compressive force is

$$P_b = E_f I_f \frac{\pi^2}{{L_c}^2} + \pi r^2 G_m \tag{3.13}$$

Therefore, the corresponding compressive stress (σ_{mic}) is given by

$$\sigma_{mic} = E_a \frac{\pi^2 r^2}{4{L_c}^2} + \frac{E_a}{E_f} G_m \tag{3.14}$$

where the first term is contributed by the transverse deflection of the fiber, and the second term is caused by the matrix shearing deformation. Based on the shearing-fracture process shown in Fig

3.4(ii), the fracture length (L_c) is close to zero at the beginning of fracture growth process, where the critical stress required for micro buckling to occur is infinite due to the first term in Eq. (3.14). Therefore, the criterion for initiating micro buckling is not met. As the fracture grows in the shear interface layer, the fracture length keeps increasing, and the critical stress deceases and converges to a constant given by the second term. However, the maximum stress (σ_b) the material can provide is limited, which means the micro buckling failure mode is activated once the fracture length is long enough to satisfy the condition that $\sigma_{mic} = \sigma_b$. Therefore, based on Eq. (3.14), it is obtained that

$$\sigma_{mic} = \left(\frac{E_f \pi^2 r^2}{4{L_{mic}}^2} + G_m\right)\left(\frac{E_a}{E_f}\right) = \sigma_b \tag{3.15}$$

Therefore, the chip length (L_{mic}) due to micro buckling is obtained as

$$L_{mic} = \sqrt{\frac{E_f \pi^2 r^2}{4}\left(\sigma_b - \frac{G_m E_a}{E_f}\right)^{-1}} \tag{3.16}$$

It is noted that there exists a lower convergence limit $G_m E_a / E_f$ for the critical stress (σ_{mic}) in Eq. (3.15). Different from the micro-buckling theory which focuses on single fiber behavior, Euler buckling theory is used to describe the macro failure mode of UD CFRP plate by Soutis [65].

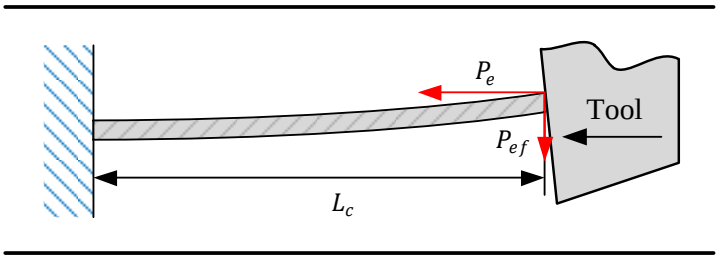

Figure 3.6 Euler buckling model and corresponding deflection.

According to the experimental observation, the deflection of the uncut workpiece material at Euler buckling mode and the boundary conditions are shown in Fig. 3.6. Since material fracture is already generated below the uncut material, there is no support from the bottom of the material. The cutting motion of the tool generates forces P_e and P_{ef} in horizontal and vertical directions respectively at the right end of the workpiece material, which are due to the compression and

friction at the tool rake face. According to buckling theory, the uncut workpiece material has elastic deflection until the buckling occurs, with the critical buckling force (P_e) satisfying the condition that

$$P_e = \frac{\pi^2 E_a I_b}{4L_{Eu}^2} = P \tag{3.17}$$

where I_b is the 2nd moment of area of the cross-section of the uncut material, and L_{Eu} is the chip length due to Euler buckling failure mode. It is noted that the critical force (P_e) is equal to critical force calculated in the pinned-free beam case. Therefore, when the fracture length in the interface layer increases from zero due to the compression of the tool, the critical stress needed for activating Euler buckling decreases from an infinite value and converges to zero. From Eq. (3.17), the chip length (L_{Eu}) is obtained as

$$L_{Eu} = \sqrt{\frac{\pi^2 E_a I_b}{4P}} \tag{3.18}$$

The buckling length is equal to the length necessary to activate either of the two failure mechanisms, expressed in Eq. (3.16) and Eq. (3.18). In fact, from the orthogonal cutting experiments of CFRP which will be further discussed in Section 3.5, the cutting force is stable during the cutting process, which means the uncut material does not buckle at the same time. This is due to the irregular tool-fiber contact at the tool rake shown in Fig. 3.1, which is a combined result of imperfections in fiber alignment, the irregular bent shape of uncut material after the buckling occurs, and irregular surface after bending-breakage process. Therefore, a coefficient (I_r) is introduced to account for there factors and needs to be identified through the experiments with real uncut chip thickness values. It should be noted that this coefficient does not influence the nonlinear relationship between the force and the real uncut chip thickness. The simulated cutting force from the developed model are validated by experiments with other real uncut chip thickness values as well. Furthermore, the identified irregular coefficient does not influence the prediction of chip length (Eq. (3.16) and Eq. (3.18)), which is also validated as explained in Section 3.5.

The cutting force component and the stress in the chip formation region is

$$F_{c,b} = I_r P = I_r t\sqrt{2E_a G_{IIC} h} \tag{3.19}$$

$$\sigma_{c,b} = \frac{F_{c,b}}{th} = I_r \sqrt{\frac{2E_a G_{IIC}}{h}} \tag{3.20}$$

The stress ($\sigma_{c,b}$) is equivalent to the cutting force coefficient (K_{tc}) which is used in mechanistic model in metal cutting theory. It can be seen from Eq. (3.20) that instead of a constant force coefficient which is generally used for force prediction for metal cutting, the stress ($\sigma_{c,b}$) decreases with the increase of real uncut chip thickness (h).

3.2.3. Thrust force prediction

As shown in Fig. 3.7, there exist two force components between the uncut material and the tool rake face in the chip formation region: compression force ($F_{r,n}$) which is perpendicular to the tool rake face, and friction force ($F_{r,f}$) which is along the tool rake face. The Coulomb friction force ($F_{r,f}$) is expressed as

$$F_{r,f} = \mu_b F_{r,n} \tag{3.21}$$

Thus, the relationship between thrust force ($F_{t,b}$) and cutting force ($F_{c,b}$) in the chip formation region is expressed as

$$\frac{F_{t,b}}{F_{c,b}} = \frac{F_{r,f}cos\alpha - F_{r,n}sin\alpha}{F_{r,n}cos\alpha + F_{r,f}sin\alpha} = \frac{\mu_b cos\alpha - sin\alpha}{cos\alpha + \mu_b sin\alpha}, \quad \alpha \leq 0 \tag{3.22}$$

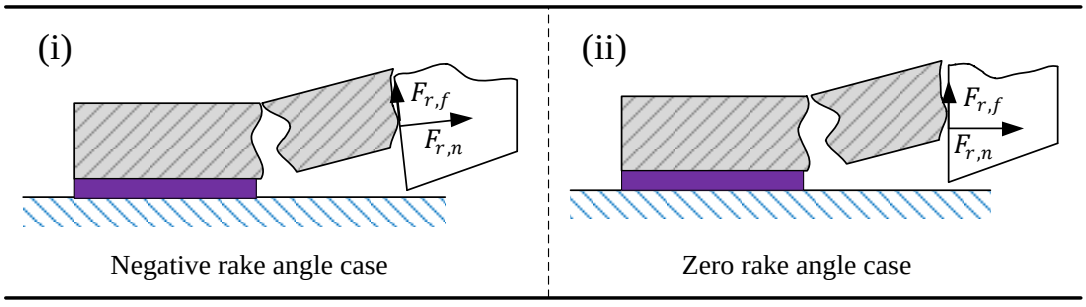

Figure 3.7 Force analysis at tool rake face in the chip formation process.

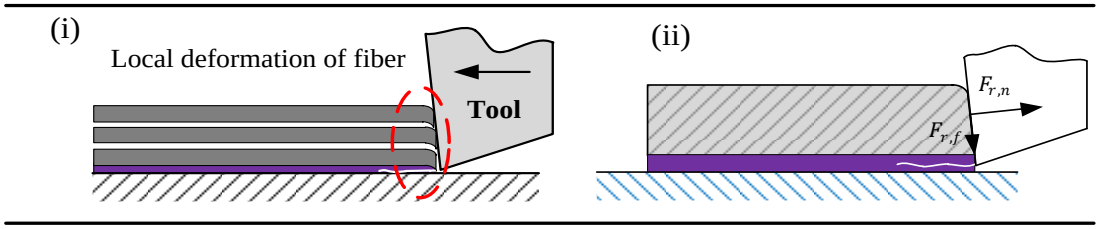

Figure 3.8 Local deformation of fibers and force analysis before buckling occurrence.

In the cutting process, the fibers near the rake face bend along the rake face before the buckling failure is activated, which results in downward friction as shown in Fig. 3.8. Then, the friction direction reverses to be upward due to the relative sliding during the chip formation process. Hence, the friction coefficient ($\mu_{b,n}$) for negative rake angle case should be smaller compared with friction coefficient ($\mu_{b,z}$) of zero rake angle case. According to Eq. (3.22), the relationship between the average cutting force ($F_{c,b}$) and thrust force ($F_{t,b}$) is updated as

$$F_{t,b} = K_t F_{c,b} \tag{3.23}$$

where the thrust coefficient K_t is given as

$$K_t = \begin{cases} \dfrac{\mu_{b,n} cos\alpha - sin\alpha}{cos\alpha + \mu_{b,n} sin\alpha} & \alpha < 0 \\ \mu_{b,z} & \alpha = 0 \end{cases} \tag{3.24}$$

3.3. Modeling of the pressing region

The material deformation in the pressing region is shown in Fig. 3.9(i). The deformation modes (buckling or bending) of the material between points *A* and *C* depend on the mechanical properties of the matrix and fiber, the transverse pressing, axial compression, friction imposed by the tool rounded edge, and the longitudinal and transverse matrix tractions which are sensitive to the spatial distribution and misalignment of the fibers.

The material deformation in the pressing region is assumed to be elastic and the pressed material in the transverse direction bounces back completely at the flank face, as shown in Fig. 3.9(i). Therefore, point *B*, which is the boundary of the pressing region, is located in the machined surface plane. The material deformation in pressing region is treated as the tool-workpiece contact

problem, with the cutting tool modeled by a tilted flat symmetric indenter with round edge, and CFRP materials modeled by an elastic half-space, as illustrated in Fig. 3.9(ii).

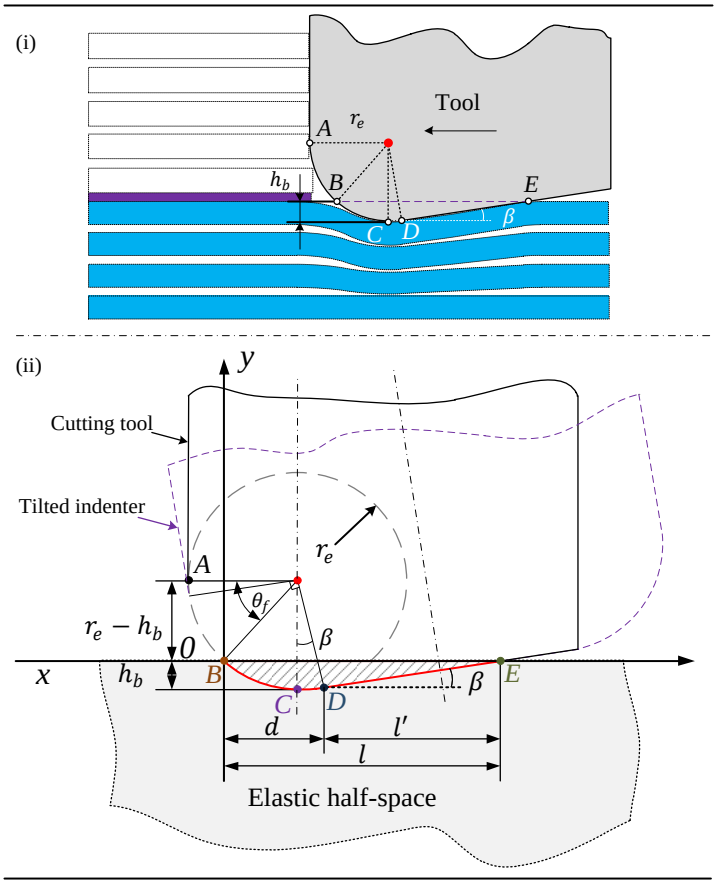

Figure 3.9 Fiber layer deflection and approximation in the pressing region.

As shown in Fig. 3.9(ii), the normal displacement (u) of the boundary surface follows the contour of the tool round edge and flank face, expressed as

$$u(x) = \begin{cases} \dfrac{(x-d)^2}{2r_e} - \dfrac{d^2}{2r_e} + \beta x, & 0 \le x \le d \\ -\dfrac{d^2}{2r_e} + \beta x & d < x \le l \end{cases} \tag{3.25}$$

where β is the slope of flank face, r_e is the tool edge radius. The distance (d) between points B and D is

$$d = \sqrt{r_e^2 - (r_e - h_b)^2} + r_e \, tan(\beta) \tag{3.26}$$

The contact length (l) between points *B* and *E* is

$$l = d + l' = d + \frac{r_e \, cos(\beta) - (r_e - h_b)}{tan\,(\beta)}. \tag{3.27}$$

The relationship between the displacement (u) and the surface normal stress (p) for a tilted flat symmetric indenter on an elastic half-space was originally developed by Sackfield et al. [66], and it is expressed in the analytical form by implementing the edge contour shown in Fig. 3.9(ii) in this chapter, shown as

$$p(x) = \frac{\gamma t}{A\pi}\left\{\frac{x-d}{d} ln \left|\frac{\sqrt{\frac{x}{l-x}} + \sqrt{\frac{d}{l-d}}}{\sqrt{\frac{x}{l-x}} - \sqrt{\frac{d}{l-d}}}\right| - \frac{\sqrt{x(l-x)}}{d} cos^{-1}(1 - \frac{2d}{l})\right\} \tag{3.28}$$

where A is the elastic composite compliance given as

$$A = \frac{2(1+v_p)}{E_t} = \frac{1}{G_t} \tag{3.29}$$

Here, the E_t and G_t are the elastic and shear moduli of the elastic half-space.

The normal force $(F_{t,p})$ is calculated by integrating the normal stress (p) in the whole contact area, expressed as

$$F_{t,p} = \int_0^l p(x)\, dx = \frac{ltd}{4A(1-c)}\left[cos^{-1} c - c\sqrt{1-c^2}\right] \tag{3.30}$$

where,

$$c = 1 - \frac{2d}{l} \tag{3.31}$$

Correspondingly, the force component in the cutting direction $(F_{c,p})$ is due to the friction generated by relative sliding movement between the tool and workpiece material, expressed as

$$F_{c,p} = \mu_p F_{t,p} \tag{3.32}$$

where (μ_p) is the Coulomb friction coefficient.

3.4. Force prediction

The overall forces in cutting and thrust directions are the summations of force components in chip formation region ($F_{c,b}$, $F_{t,b}$) and tool compression region ($F_{c,p}$, $F_{t,p}$), expressed as

$$F_c = F_{c,b} + F_{c,p} \tag{3.33}$$

$$F_t = F_{t,b} + F_{t,p}. \tag{3.34}$$

Substituting Eqs. (3.19), (3.23), (3.30), and (3.32) into Eqs. (3.33) and (3.34), the analytical expressions for predicting the resultant cutting and thrust forces are expressed as

$$F_c = F_{c,b} + F_{c,p} = I_r t\sqrt{2E_a G_{IIC} h} + \frac{\mu_p ltd}{4A(1-c)}\left[cos^{-1} c - c\sqrt{1-c^2}\right] \tag{3.35}$$

$$F_t = F_{t,b} + F_{t,p} = K_t I_r t\sqrt{2E_a G_{IIC} h} + \frac{ltd}{4A(1-c)}\left[cos^{-1} c - c\sqrt{1-c^2}\right]. \tag{3.36}$$

3.5. Experimental validation

3.5.1. Experimental setup for orthogonal cutting

Orthogonal cutting experiments of UD CFRP were performed on a CNC machine (Fadal VMC 2216), as shown in Fig. 3.10. A cylindrical steel bar was clamped in the tool holder, and the angular motion was locked during the experiments to keep the tool stationary. To investigate the effects of tool rake and clearance angles on the forces, the cutting tool is tilted with four different angles, as shown in Fig. 3.11. The fiber orientation of UD CFRP workpiece was adjusted to be parallel to the cutting direction. A three-axis dynamometer (Kistler 9257B) was mounted below the workpiece to measure the forces in the cutting and thrust directions. Two adapter plates were used to fix the vice and the dynamometer. The machined chips were collected and examined under an optical microscope. The chip lengths were measured in order to validate the predicted lengths by the developed model. The workpiece dimension, cutting insert information, and the cutting

parameters in the experiments are provided in Table 3.1. The mechanical properties of the CFRP materials used in the experiments are given in Table 3.2.

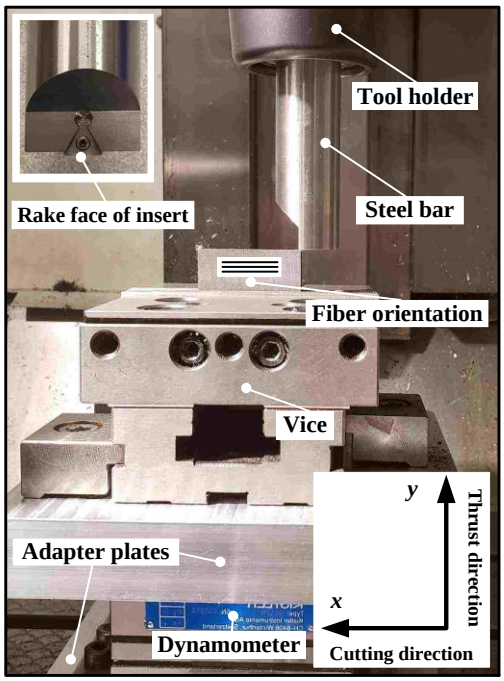

Figure 3.10 Experimental setup for orthogonal cutting of UD CFRP.

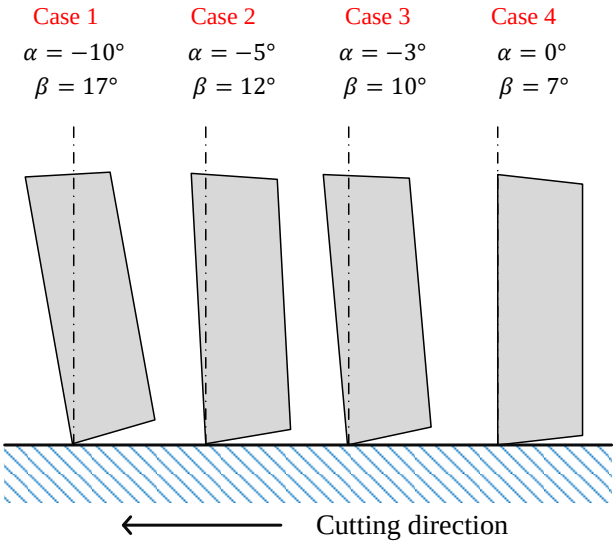

Figure 3.11 Inclined angles of the tool.

Table 3.1 Cutting condition.

Workpiece	Width/Length	4.5 $mm/50\ mm$
Cutting Insert	Rake angle α	$-10°, -5°, -3°, 0°$
	Clearance angle β	$17°, 12°, 10°, 7°$
	Tool edge radius	15 μm
Cutting Parameters	Fiber orientation	0° (Parallel cutting)
	Cutting velocity	2500 mm/min
	Real uncut chip thickness h	$0.01, 0.03, 0.05, 0.075, 0.1, 0.15, 0.20, 0.25, 0.30\ mm$

Table 3.2 UD CFRP mechanical properties.

Carbon fiber (T700)		**Epoxy resin (**301T, Toughened, RT**)**	
Tensile modulus $\boldsymbol{E_f}$	234 GPa	Tensile modulus $\boldsymbol{E_m}$	3.1 GPa
Tensile strength $\boldsymbol{\sigma_{fs}}$	4830 MPa	Shear modulus $\boldsymbol{G_m}$	1.16 GPa
Fiber diameter $\boldsymbol{d_f}$	7 μm	Epoxy proportion $\boldsymbol{v_m}$	45 %
Fiber proportion $\boldsymbol{v_f}$	55 %		
Material parameters. ([42], [49], [67], [68]. Parameters with $*$ are chosen in accordance with similar material and cutting conditions based on the availability of the literature data)			
Transverse modulus $\boldsymbol{E_t}$	5.53 GPa	Height of boundary $\boldsymbol{h_b}$ $*$	2.625 μm
Friction coefficient $\boldsymbol{\mu_p}$ $*$	0.13	Poisson's ratio $\boldsymbol{v_p}$	0.29
Fracture toughness $\boldsymbol{G_{IIC}}$ $*$	0.99 N/mm		

3.5.2. Identification of friction coefficient and irregular contact coefficient

For zero tool rake angle condition, the friction coefficient $\mu_{b,z}$ is identified by fitting the linear relationship between the experimental force data of F_t and F_c at four uncut chip thicknesses ($h = 0.15\ mm, 0.20\ mm, 0.25\ mm, 0.30\ mm$). The fitted line and the comparison with the forces in the whole range of uncut chip thicknesses is shown in Fig. 3.12. For negative rake angle, $\mu_{b,n}$ is identified from the cutting force data when the rake angle is $-3°$, and the identification procedure is the same as that with zero rake angle. Then, the identified friction coefficient ($\mu_{b,n}$) is used to predict the forces for all the negative rake angle cases shown in Fig. 3.11 at different uncut chip thicknesses.

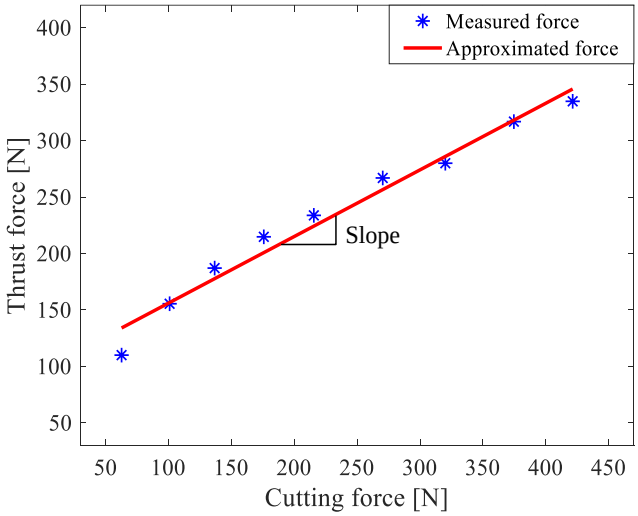

Figure 3.12 Thrust-cutting force relatinonship with friction coefficient identification.

The coefficient I_r was calibrated using experimental data of cutting forces at four uncut chip thicknesses values ($h = 0.15\ mm, 0.20\ mm, 0.25\ mm, 0.30\ mm$) for zero tool rake angle condition, while the cutting forces and chip lengths in the whole range of uncut chip thickness (0.01 mm - 0.30 mm) are predicted. It should be noted that the nonlinear relationship between the force and the uncut chip thickness is not affected by the I_r value. The identified friction coefficients and the irregular contact coefficient are listed in Table 3.3.

Table 3.3 Identified friction coefficients and irregular contact coefficient.

Irregular coefficient	I_r	0.311
Friction coefficient	$\mu_{b,z}$	0.59
Friction coefficient	$\mu_{b,n}$	0.35

3.5.3. Results and discussion

Fig. 3.13 shows the typical force evolution results in time domain. It is found that the forces in both cutting and thrust directions reach steady state during the cutting operation even though the amplitude of the vibration increases with the real uncut chip thickness.

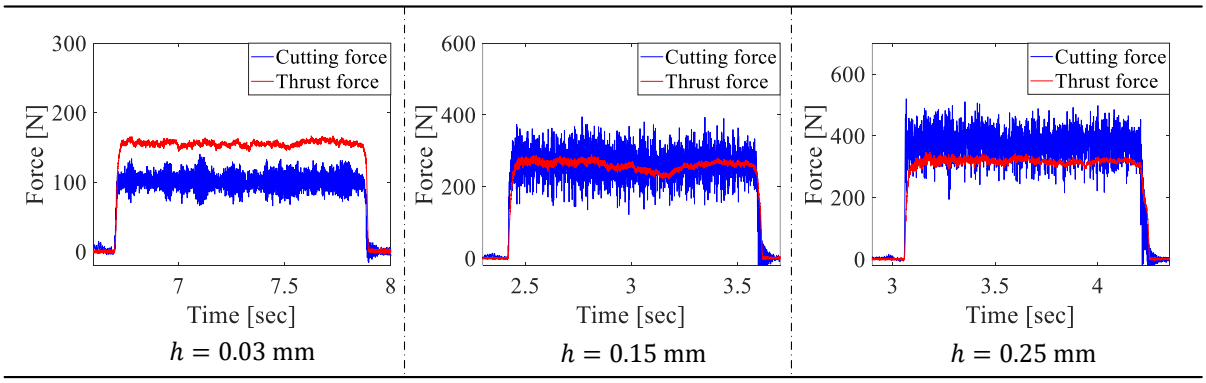

Figure 3.13 Typical measured cutting and thrust forces at various real uncut chip thicknesses.

Fig. 3.14 shows the simulated and experimental cutting and thrust forces with respect to the real uncut chip thicknesses at zero tool rake angle. It is proved that the relationship between the forces and the real uncut chip thickness is nonlinear. In metal cutting theory, the nonlinearity is mainly due to the ploughing and contact forces at the tool round edge and the flank face, while the nonlinearity for cutting UD-CFRP with zero fiber orientation is attributed to the shearing-buckling mechanism. The increments of the resultant forces are caused by the increase of real uncut chip thickness in the chip formation region, while the force components in the tool pressing region ($F_{c,p}$ and $F_{t,p}$) are not related to the real uncut chip thickness, and remain constant. Fig. 3.14(ii) and (iii) show the simulated and experimental results of the force components in chip formation region and tool pressing region respectively. The nonlinear relationship between the force in chip formation

region and the real uncut chip thickness is demonstrated, which is different from the mechanistic model from metal cutting theory assuming a linear force - uncut chip thickness relationship as proposed by Merchant [39]. Based on the cutting force results, the buckling stresses ($\sigma_{c,b}$) are obtained and shown in Fig. 3.14(iv). The buckling stresses decrease nonlinearly with the increase of real uncut chip thickness values, which shows a 'size effect' in orthogonal cutting of CFRP. It is noted that the "size effect" phenomenon in machining UD CFRP refers to the nonlinear relation between the buckling stress and real uncut chip thickness. This is different from the "size effect" in machining metal alloys, which is mainly attributed to the ploughing mechanism associated with cutting edge. The fundamental reason for the 'size effect' revealed from the developed physical model is that the chip formation mechanism is dominated by the fracture of CFRP material at the interface layer under the motion of the cutting tool, as expressed in Eq. (3.20). It is because the Mode II fracture energy at the interface layer is not related to the real uncut chip thickness, as shown in Eq. (3.5). In order to initiate the fracture of the interface layer, higher energy density is required in the chip formation region with smaller real uncut chip thickness value (h), which means higher buckling stresses.

In order to evaluate the effects of various negative tool rake angles on cutting and thrust forces, the comparisons between the simulations and experimental data for the three tool rake angles ($-3°$, $-5°$ and $-10°$) are provided in Figs. 3.15-3.17. The irregular cutting coefficient (I_r) identified from zero tool rake angle is also used for negative tool rake angle conditions. Besides, the friction coefficients in the chip formation region identified with $-3°$ rake angle is used for the prediction of $-5°$ and $-10°$ cases. The results show that the cutting force in the chip formation region increases with tool rake angle slightly due to higher friction between the fracture surfaces in the fracture zone with higher compression force; while the thrust force varies significantly with the rake angle, which is due to the reversal of friction direction and changes of geometric relation between the normal and friction forces on the rake face, as explained in Eq. (3.23) and (3.24). Overall, it is found that the forces can be predicted for different negative tool rake angles with acceptable accuracy.

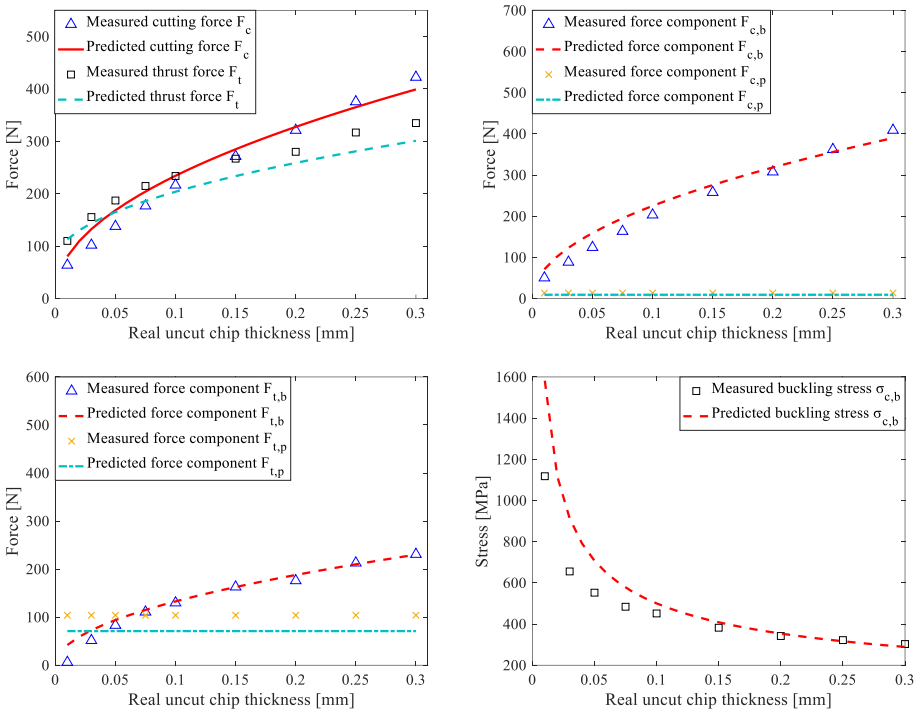

Figure 3.14 Comparisons of experimental measurements and predicted forces ($\alpha = 0°, \beta = 7°$).

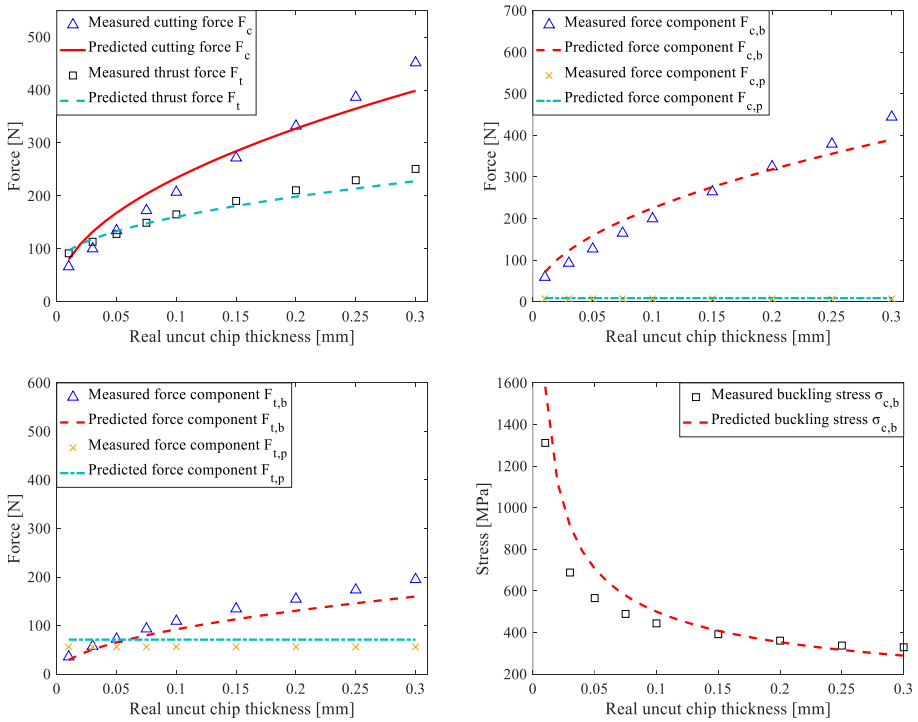

Figure 3.15 Comparisons of experimental measurements and predicted forces ($\alpha = -3°, \beta = 10°$).

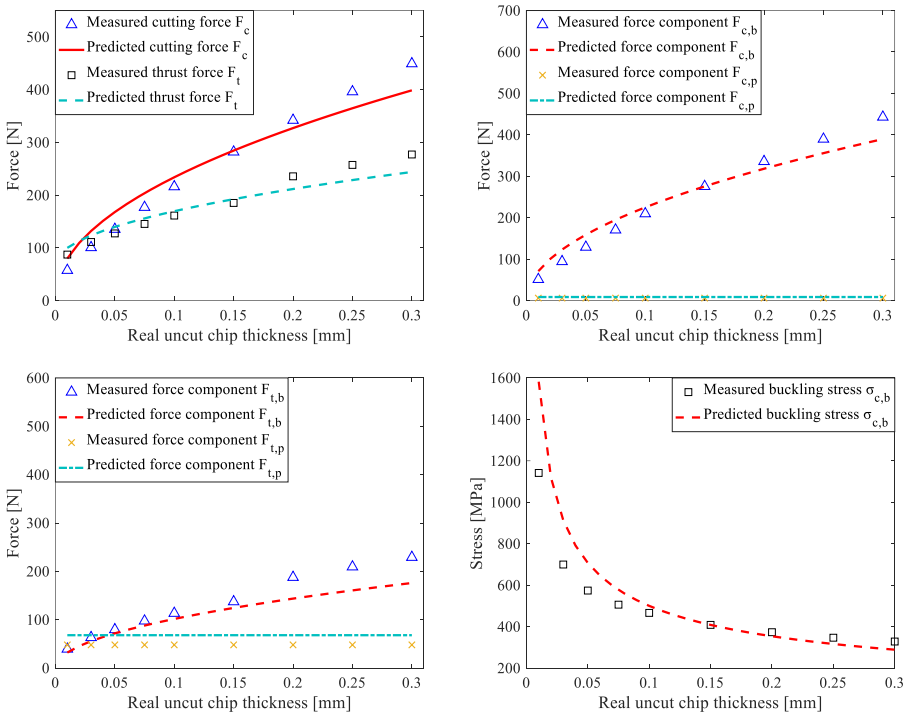

Figure 3.16 Comparisons of experimental measurements and predicted forces ($\alpha = -5°, \beta = 12°$).

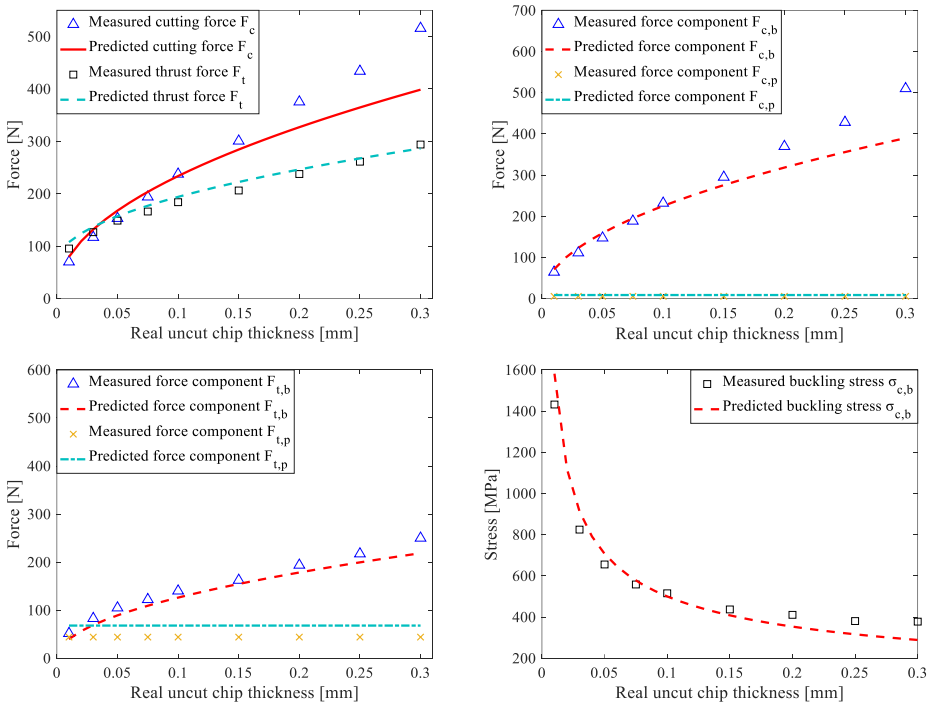

Figure 3.17 Comparisons of experimental measurements and predicted forces ($\alpha = -10°, \beta = 17°$).

Considering that the chip length measurements are similar for four cases, only the lengths of the machined chips for case 1 (zero rake angle) are given and compared with the predicted results, which are not related to the irregular coefficient (I_r) in the proposed model. Fig. 3.18(i) shows a pile of machined chips after the cutting experiments. According to the examinations by optical microscope, the machined chips are classified into four categories: block-like chips (type 1); adhesive chips (type 2); beam-like chips (type 3); and powder-like chips (type 4), as shown in Fig. 3.18(ii). The chip lengths for the first three categories were measured, since the powder-like chips do not have a regular geometry for proper measurement. For the type-2 chip shown in Fig. 3.18(ii), the adhesive chips are composed of four beam-like chips which are measured separately. In fact, based on the microscopic observations, the adhesive chips are always composed of around 2-6 beam-like chips.

Fig. 3.19(i) shows the distribution of measured chip lengths at different real uncut chip thicknesses, as well as the predicted chip lengths with micro buckling and Euler buckling modes. Fig. 3.19(ii) shows a close-up view when the uncut chip length is below 0.4 mm. The experimental data shows that the chip lengths are concentrated and distributed into two separated ranges. The lengths of the block-like chips are close to the prediction of due to Euler buckling, while the lengths for the adhesive chips and beam-like chips are close to the predicted values using micro buckling prediction. The chips for the real uncut chip thicknesses of $10, 30\ \mu m$ are mainly composed of powder-like chips which can not be measured. The number of block-like chips decreases significantly when the real uncut chip thickness decreases, and this category of chips is not observed when the real uncut chip thickness is smaller that $150\ \mu m$. However, the other three categories of chips exist in the whole range of the real uncut chip thicknesses.

It is noted that the length measurements of type 2 and type 3 chip lengths are higher than the prediction results. According to micro buckling and Euler buckling theories, the micro buckling failure starts from the failure of a single fiber, which results in stress concentration in the vicinity, while Euler buckling occurs like a macro deformation, that is, most or all of the fibers in the uncut material buckle at same time. In fact, it is the combination of Euler buckling mode and micro buckling mode that determines the chip formation process. Therefore, the chip length predicted by the micro buckling theory represents the lower boundary corresponding to type 2 and type 3 chip.

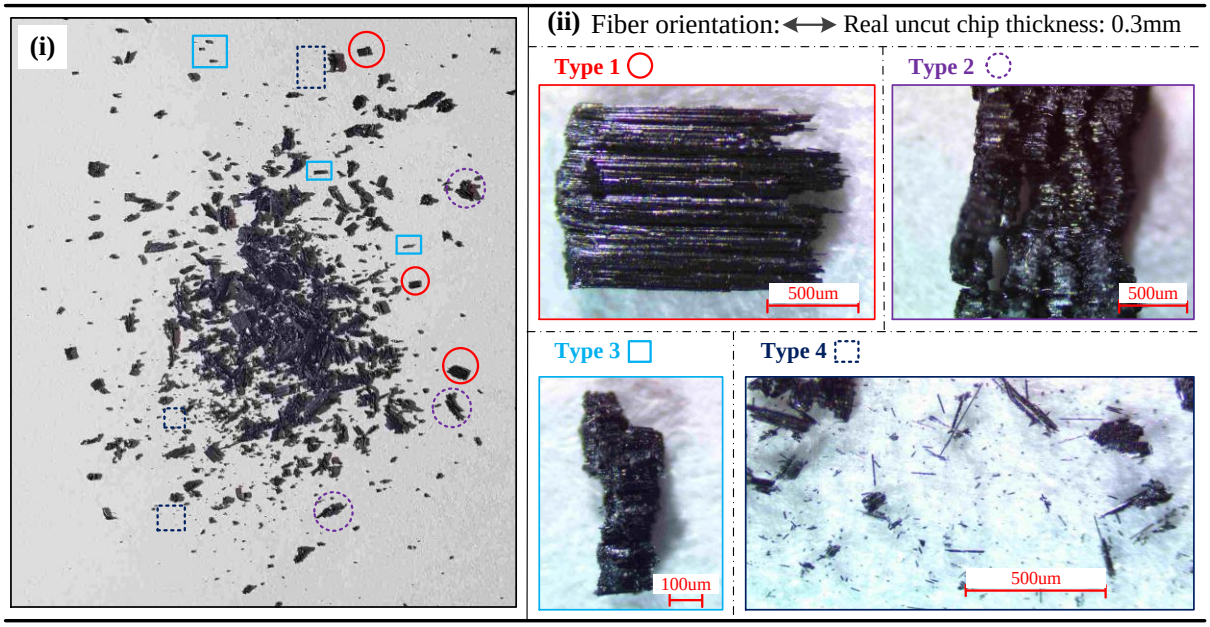

Figure 3.18 Typical chip geometry.

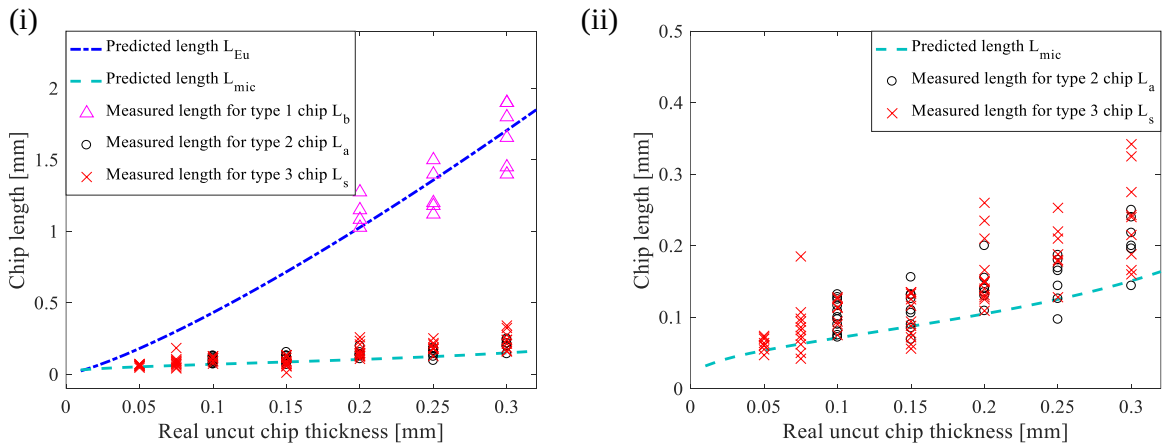

Figure 3.19 Comparisons of experimental measurements and predicted chip lengths.

3.6. Conclusion

The material deformation mechanism differs at different fiber orientation angles in orthogonal cutting of CFRP. This research focuses on the development of an analytical model to explain the nonlinear force – uncut chip thickness relationship due to the shearing-buckling deformation of CFRP material in orthogonal cutting. Energy method is used to predict the cutting force due to the shearing and fracture propagation in the shear interface layer of the workpiece. Material buckling occurs afterwards, with the chips formed in micro buckling and Euler buckling modes. The cutting

forces are predicted by integrating the force components in chip formation and tool pressing regions. It is found that the simulated cutting force and chip lengths match with the experimental results under different real uncut chip thickness values. The following conclusions are drawn:

(1) The shearing process inside the interface shear layer plays a key role for the determination of the critical buckling stress and cutting force. It is because the maximum resistance force provided by the workpiece material depends on the shear deformation and the fracture energy in the interface layer.

(2) The resistance force is constant when the fracture zone in the interface layer grows. The fracture energy is independent from the real uncut chip thickness. Therefore, the strain energy density required for the chip formation increases with the decrease of the real uncut chip thickness value, which shows a 'size effect' in orthogonal cutting process. The ratio of the fracture energy over strain energy keeps decreasing when the real uncut chip thickness increases. As a result, the buckling stress which is affected by the constant fracture energy and real uncut chip thickness-related strain energy changes with the real uncut chip thickness. This 'size effect' results in nonlinear force – real uncut chip thickness relationship, which is different from the mechanistic model in metal cutting theory.

(3) Material buckling is activated once the fracture length is beyond a critical value, which is determined by micro buckling and Euler buckling modes. In all four cases, Euler buckling occurs when the real uncut chip thickness is higher than $150\ \mu m$, while the micro buckling dominates the chip formation process in the whole range of real uncut chip thickness values used in this research.

(4) The friction coefficients and irregular contact coefficient should be experimentally identified for the force prediction. The comparisons between the simulations and experimental results show that the coefficients identified under certain uncut chip thicknesses and tool rake angle can be used to predict the forces at other cutting conditions with acceptable accuracy.

4. Analytical Modeling of Chip Formation Mechanism in Cutting Unidirectional CFRP

This chapter presents the analytical prediction of CFRP chip formation modes, including fiber tension, fiber compression, matrix tension, and matrix compression, based on the stress state in the chip formation region in the fiber orientation range of $[0°, 180°]$. The chip formation angle and the stresses activating the material failure on the chip formation plane are predicted with the minimum cutting energy principle. The transition of the chip formation mode as the fiber orientation increases, and the variations of the chip morphology and cutting forces owing to the change of chip formation mode are predicted and analyzed. The chip formation angle, chip morphology, and cutting forces are compared between the simulations and the measurements through orthogonal cutting experiments of UD CFRP at different uncut chip thicknesses and fiber orientations.

4.1. Orthogonal Cutting Mechanics Model of UD CFRP

Orthogonal cutting configuration is used in this chapter to understand the fundamental chip formation mechanism and the relationship between the cutting forces and process parameters. As shown in Fig. 4.1, θ is the fiber orientation in the range of $[0°, 180°]$, which is defined by the intersection angle between the fiber direction of CFRP and the cutting direction. Due to the compression and friction at the tool rake face, the fracture of the CFRP material occurs at a chip formation plane denoted by AB in Fig. 4.1, with the orientation determined by chip formation angle (φ). Due to the cutting tool motion, the CFRP workpiece material is separated after failure occurrence and moves along the tool rake and flank faces. The deformation zone is divided into chip formation, sliding, and pressing regions. In the chip formation region, the CFRP material approaches the tool rake face in the cutting velocity direction, and fracture occurs at the chip formation plane. Then, the formed chip moves upwards and slides along the tool rake face in the sliding region. During this chip formation process, the resultant cutting force (F_c) contributed by the force components perpendicular (F_n) and along (F_s) the chip formation plane AB is balanced by the resultant force of the normal compression (F_v) and sliding friction (F_u) force on the contact region AC between the chip and tool rake face, as shown in Fig. 4.1. It should be noted that different from metal cutting in which the chips are formed by the shearing of the metallic material or the shear force (F_s) on a shear plane, the chip formation for CFRP is caused by the fiber and matrix failure under both the normal and shear forces (F_n, F_s). In the pressing region, the sub-

surface material deforms under the compression of the cutting tool edge and stays in contact with the flank face AD owing to the spring-back effect. Because this chapter focuses on the material removal process, the model for the pressing region is not included. The following assumptions, which are used in the related work in the literature [38, 40], are applied in developing the mechanics model:

(1) The chips are formed owing to the quasi-continuous failure of uncut material.
(2) The chip formation region is treated as a flat plane with infinitely small thickness.
(3) This model mainly focuses on the effect of fiber orientation on the cutting mechanics, therefore, the effects of strain rate, temperature, and moisture on the CFRP mechanical property are neglected.
(4) The friction coefficient between the formed chip and rake face is determined by the tool and workpiece material, and is assumed to be a constant in the entire fiber orientation range of $[0°, 180°]$.

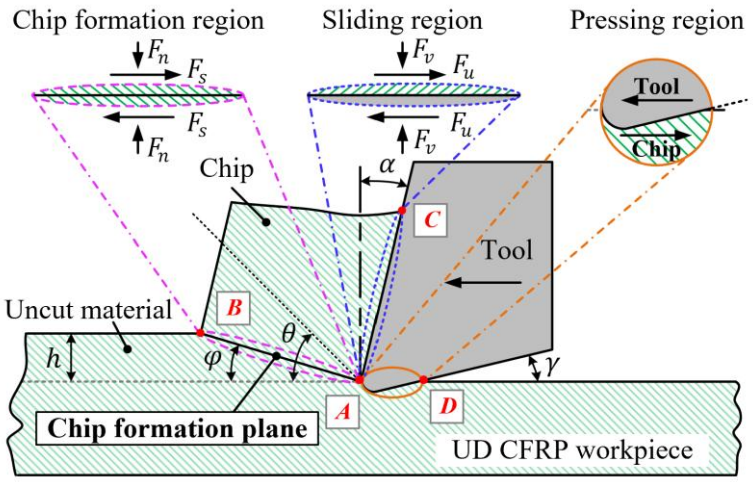

Figure 4.1 Chip formation and forces in three deformation regions in cutting UD CFRP.

In the orthogonal cutting process of CFRP, based on the fiber orientation (θ) and chip formation angle (φ), the intersection angle between the fiber direction and the chip formation plane is defined as the fiber cutting angle (δ), expressed as:

$$\delta = \varphi - \theta \tag{4.1}$$

The positive fiber cutting angle indicates a chip formation angle larger than the fiber orientation, and vice versa. The fiber orientation is a parameter provided based on the cutting condition and the chip formation angle is an unknown parameter to be determined. To evaluate the failure of the uncut material in the chip formation region, the stress state on the chip formation plane is transformed to the stress state in the CFRP ply coordinate system. As shown in Fig. 4.2, the $X-Y$ coordinate system is based on the chip formation plane, and $1-2$ coordinate refers to the CFRP ply orientation based on the fiber orientation. Three possible stress transformation cases when fiber orientation is smaller than, equal to, and larger than 90° are presented in Fig. 4.2. The stress transformation angle is equal to the fiber cutting angle. Let σ_n and τ_s be the compressive stress and shear stress on the chip formation plane respectively, the corresponding stress state $(\sigma_{11}, \sigma_{22}, \tau_{12})$ in the CFRP ply coordinate system through stress transformation is expressed as:

$$\begin{aligned}\sigma_{22} &= \sigma_n cos^2\delta + 2\tau_s sin\delta cos\delta \\ \sigma_{11} &= \sigma_n sin^2\delta - 2\tau_s sin\delta cos\delta \\ \tau_{12} &= -\sigma_n sin\delta cos\delta + \tau_s(cos^2\delta - sin^2\delta)\end{aligned} \tag{4.2}$$

where σ_{11} and σ_{22} are the normal stresses along and perpendicular to the carbon fibers respectively, and τ_{12} is the shear stress. The directions of the three stresses corresponding to their positive values are shown in Fig 4.3.

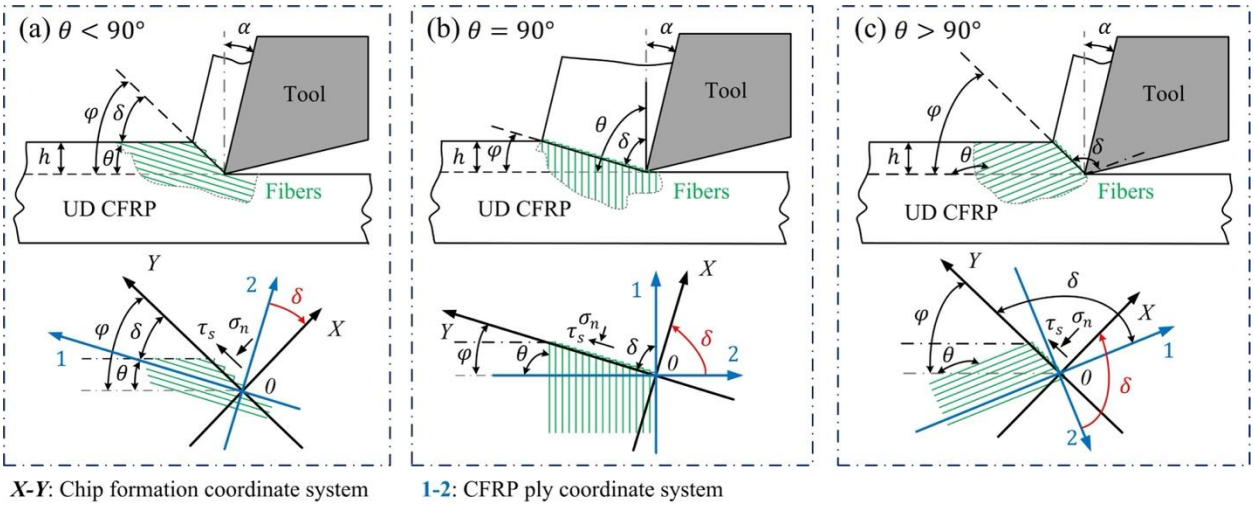

Figure 4.2 Relationship between chip formation angle and fiber orientation in different ranges. (a) Positive fiber cutting angle for $\theta < 90°$, (b) negative fiber cutting angle for $\theta = 90°$, (c) negative fiber cutting angle for $\theta > 90°$.

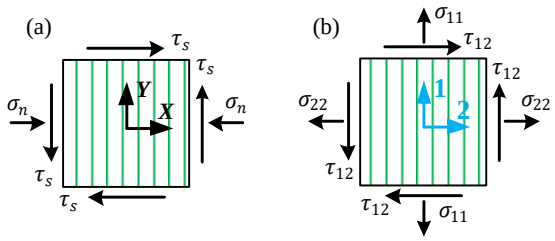

Figure 4.3 Stress states in the chip formation and CFRP ply coordinates. (a) Chip formation coordinate, (b) CFRP ply coordinate.

The ratio between the compressive stress (σ_n) and shear stress (τ_s) on the chip formation plane is derived from the force equilibrium condition of the machined chip similar to metal cutting mechanics [39], expressed as:

$$\frac{\sigma_n}{\tau_s} = -\frac{\frac{F_n}{A_c}}{\frac{F_s}{A_c}} = -tan\left(\varphi + \beta_f - \alpha\right) = -T \tag{4.3}$$

where the negative sign in front of the fraction indicates the relationships between the negative (compressive) normal stress (σ_n) and the positive shear stress (τ_s) corresponding to the stress directions as shown in Fig. 4.3. α and β_f are the tool rake angle and the friction angle at the tool rake face. β_f is determined from the tool-chip friction coefficient $\beta = tan^{-1}(\mu)$. A_c is the area of the chip formation plane as:

$$A_c = \frac{bh}{sin(\varphi)} \tag{4.4}$$

where b and h are the width of cut and uncut chip thickness of the CFRP workpiece, respectively. Therefore, the stress state $(\sigma_{22}, \sigma_{11}, \tau_{12})$ with respect to the CFRP ply coordinate system is updated by replacing σ_n in Eq. (4.2) from Eq. (4.3), expressed as:

$$\begin{aligned} \sigma_{22} &= \tau_s(2sin\delta cos\delta - Tcos^2\delta) \\ \sigma_{11} &= \tau_s(-2sin\delta cos\delta - Tsin^2\delta) \\ \tau_{12} &= \tau_s(cos^2\delta - sin^2\delta + Tsin\delta cos\delta) \end{aligned} \tag{4.5}$$

From Eq. (4.5), the stress state $(\sigma_{22}, \sigma_{11}, \tau_{12})$ in the CFRP ply coordinate system is determined by fiber cutting angle (δ), the shear stress (τ_s), and the ratio (T) between the compressive stress and shear stresses. Therefore, for a certain cutting condition with the defined tool rake angle (α), tool-chip friction angle (β_f), and fiber orientation (θ), the stresses σ_{22}, σ_{11}, and τ_{12} are functions of two variables: shear stress (τ_s) and chip formation angle (φ) (or fiber cutting angle (δ), see Eq. (4.1)). In the orthogonal cutting process, the failure of CFRP workpiece material occurs to form the chip, which suggests the direction of shear stress (τ_s) shown in Figs. 4.2 and 4.3 to be positive. Therefore, the signs of the three stresses σ_{22}, σ_{11}, and τ_{12} are known for a potential chip formation angle (to be determined) under given cutting condition parameters.

To determine the failure of uncut material in the chip formation, the combined Hashin's and Puck's failure criteria [57, 58] which define the failure modes of CFRP based on the directions of the normal stresses are implemented in this chapter. Hashin's failure criterion is used for fiber tension, fiber compression, and matrix tension failure modes, and Puck's failure criterion is used for matrix compression failure mode. In Puck's failure criterion, the enhancement of the transverse compression on the shear strength is considered. The Hashin's and Puck's failure criteria corresponding to the four failure modes are explained below:

(i). Fiber-dominated failure

Fiber tension $(\sigma_{11} \geq 0)$ and compression $(\sigma_{11} < 0)$ failure.

$$HP_{f,t} = \left(\frac{\sigma_{11}}{X_{11}^t}\right)^2 + \left(\frac{\tau_{12}}{S_{12}}\right)^2 = 1, \qquad for\ \sigma_{11} \geq 0$$
$$HP_{f,c} = \left(\frac{\sigma_{11}}{X_{11}^c}\right)^2 = 1, \qquad for\ \sigma_{11} < 0 \tag{4.6}$$

(ii). Matrix failure

Matrix tension $(\sigma_{22} \geq 0)$ and compression $(\sigma_{22} < 0)$ failure.

$$HP_{m,t} = \left(\frac{\sigma_{22}}{X_{22}^t}\right)^2 + \left(\frac{\tau_{12}}{S_{12}}\right)^2 = 1, \qquad for\ \sigma_{22} \geq 0 \tag{4.7}$$

$$HP_{m,c} = \left(\frac{\tau_{12}}{S_{12} + e_{nl}\sigma_{22}}\right)^2 = 1, \qquad for \quad \sigma_{22} < 0$$

where X_{11}^t and X_{11}^c are the tensile and compressive strengths in the fiber direction. X_{22}^t is the tensile strength in the transverse direction. e_{nl} is the 'internal friction' coefficient which represents the enhancement effect of the shear strength (S_{12}) under compressive stress in the transverse direction. The chip formation occurs when the stress state on the chip formation plane satisfies any one of the failure modes of CFRP in Eqs. (4.6) and (4.7).

By replacing the stresses $\sigma_{22}, \sigma_{11}, \tau_{12}$ in Eqs. (4.6) and (4.7) from Eq. (4.5), four failure modes of CFRP under a certain cutting condition (tool rake angle (α), tool-chip friction angle (β_f), and fiber orientation (θ)) are related to the strength constants (X_{11}^t, X_{11}^c, X_{22}^t, S_{12}, e_{nl}) of CFRP, with chip formation angle (φ) and shear stress (τ_s) to be identified, expressed as:

$$\begin{aligned}
&\left(\frac{\tau_s(-2sin\delta cos\delta - Tsin^2\delta)}{X_{11}^t}\right)^2 + \left(\frac{\tau_s(cos^2\delta - sin^2\delta - Tsin\delta cos\delta)}{S_{12}}\right)^2 = 1 && \text{Fiber tension}\\
&\left(\frac{\tau_s(-2sin\delta cos\delta - Tsin^2\delta)}{X_{11}^c}\right)^2 = 1 && \text{Fiber compression}\\
&\left(\frac{\tau_s(2sin\delta cos\delta - Tcos^2\delta)}{X_{22}^t}\right)^2 + \left(\frac{\tau_s(cos^2\delta - sin^2\delta - Tsin\delta cos\delta)}{S_{12}}\right)^2 = 1 && \text{Matrix tension}\\
&\left(\frac{\tau_s(cos^2\delta - sin^2\delta - Tsin\delta cos\delta)}{S_{12} + e_{nl}\tau_s(2sin\delta cos\delta - Tcos^2\delta)}\right)^2 = 1 && \text{Matrix compression}
\end{aligned} \tag{4.8}$$

Because the only two unknown parameters are the shear stress (τ_s) and chip formation angle (φ) under a certain cutting condition, I can build the analytical relationship between the shear stress and the potential chip formation angle by solving the Eq. (4.8). In addition, Fig. 4.3 shows that there are four stress states considering the signs of two normal stresses (σ_{11}, σ_{22}): (1) fiber tension-matrix tension ($\sigma_{11} \geq 0$ & $\sigma_{22} \geq 0$) ; (2) fiber tension-matrix compression ($\sigma_{11} \geq 0$ & $\sigma_{22} < 0$); (3) fiber compression-matrix tension ($\sigma_{11} < 0$ & $\sigma_{22} \geq 0$); (4) fiber compression-matrix compression ($\sigma_{11} < 0$ & $\sigma_{22} < 0$). The signs of the normal stresses σ_{22}, σ_{11} are known given a potential chip formation angle from Eq. (4.5). Therefore, I am able to calculate one shear stress ($\tau_{s,1}$) using the fiber-dominated failure modes (tension/compression) and one shear stress

($\tau_{s,2}$) using the matrix failure mode (tension/compression) for a potential chip formation angle. According to Hashin's and Puck's failure criteria, the failure of the CFRP material is initiated when any one of four failure indices ($HP_{f,t}, HP_{f,c}, HP_{m,t}, HP_{m,c}$) reaches unity. The smaller value of two shear stresses $\tau_{s,1}$ and $\tau_{s,2}$:

$$\tau_s = min\ (\tau_{s,1}, \tau_{s,2}) \tag{4.9}$$

is used as the actual shear stress (τ_s) by satisfying the Hashin's and Puck's failure criteria, and the corresponding failure mode is identified as the primary mode for chip formation in the cutting of UD CFRP. The failure mode which refers to the smaller shear stress corresponds to the secondary chip formation mode, because it can occur at the same chip formation angle owing to the uncertainty of local material property, mainly caused by CFRP defects such as voids, fiber misalignment, and uneven distribution of fibers. This is proven by the experimental results showing the co-existence of two types of chip morphology corresponding to the transition of the chip formation mode, which will be discussed in detail in section 4.2.2.

After the quantitative relationship between the shear stress (τ_s) and the chip formation angle (φ) is developed after Eq. (4.9), the tangential cutting force [39] is calculated based on the potential chip formation angle under a given fiber orientation, expressed as:

$$F_{tc} = A_c \frac{\tau_s(\delta, \theta) cos\ (\beta_f - \alpha)}{cos\ (\varphi + \beta_f - \alpha)} = bh \frac{\tau_s(\varphi - \theta, \theta) cos\ (\beta_f - \alpha)}{sin(\varphi) cos\ (\varphi + \beta_f - \alpha)} \tag{4.10}$$

For a constant cutting velocity (V), the cutting power (W) is expressed as:

$$W = F_{tc} V = bhV \frac{\tau_s(\varphi - \theta, \theta) cos\ (\beta_f - \alpha)}{sin(\varphi) cos(\varphi + \beta_f - \alpha)} \tag{4.11}$$

In Eq. (4.11), the only independent parameter to be determined is the chip formation angle (φ). In this model, for a given fiber orientation (θ), I scan the potential chip formation angles in the entire range of $[0°, 180°]$, which refers to the fiber cutting angle (δ) of $[-\theta, 180° - \theta]$. The cutting power is calculated for the entire range of potential chip formation angle, and then the chip formation angle which corresponds to the minimum cutting power is identified based on the minimum energy principle. With the identified chip formation angle, the shear stress is calculated

using Eq. (4.9), and the corresponding failure mode is determined accordingly. Then, the tangential cutting force (F_{tc}) is calculated by Eq. (4.10), and the feed cutting force (F_{fc}) and resultant force (F_c) are obtained as:

$$F_{fc} = F_{tc} tan(\beta_f - \alpha) \tag{4.12}$$

$$F_c = \frac{F_{tc}}{sin\,(\beta_f - \alpha)} \tag{4.13}$$

Therefore, the failure modes, chip formation angle, and cutting forces for the entire fiber orientation range from 0° to 180° can be predicted using a unified cutting mechanics model. The flowchart of the proposed mechanics model is summarized in Fig. 4.4. The input parameters are the cutting conditions (α, β_f, θ) and the CFRP mechanical properties ($X_{11}^t, X_{11}^c, X_{22}^t, S_{12}, e_{nl}$), and the outputs include chip formation modes, chip formation angle, and cutting forces.

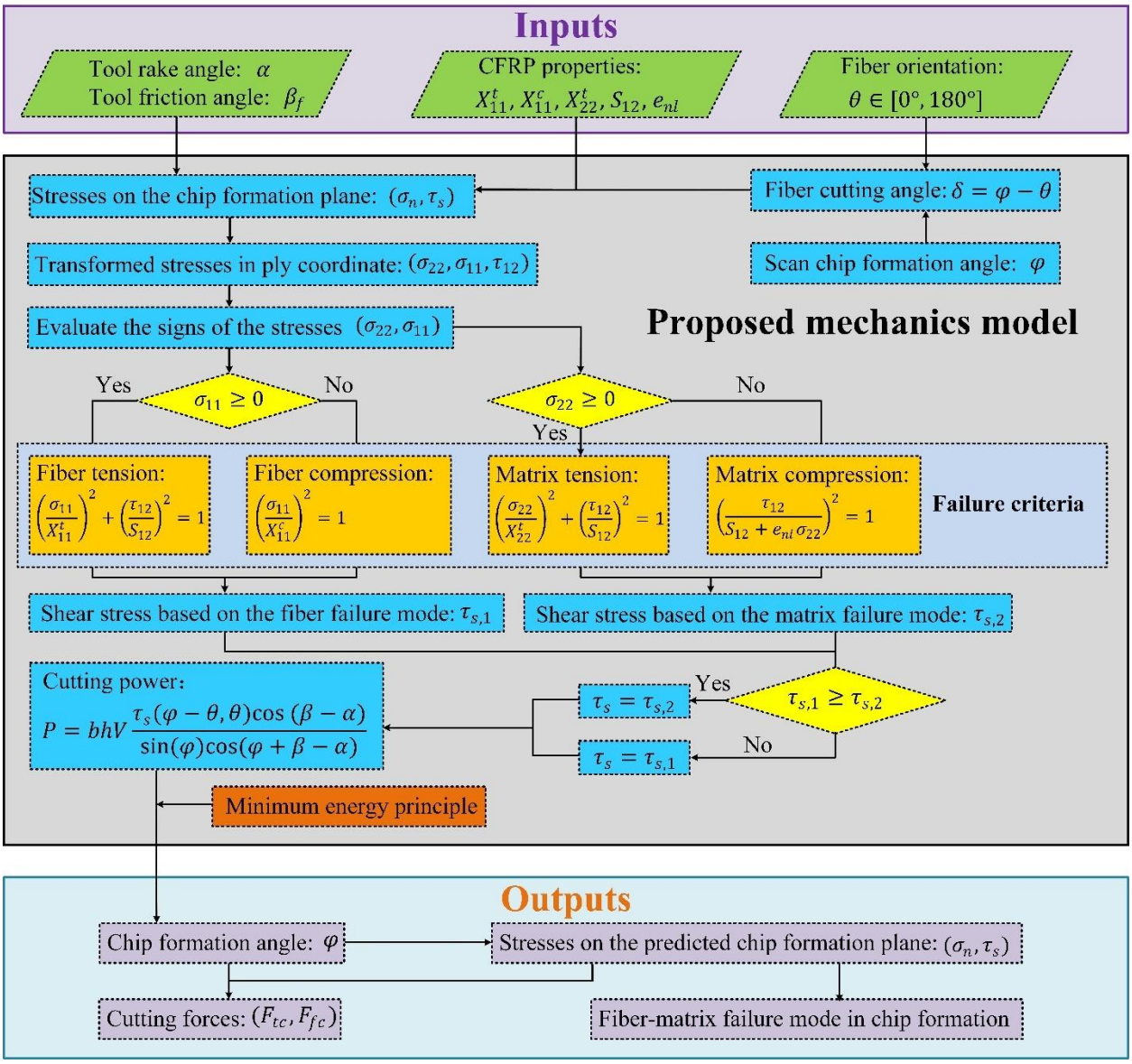

Figure 4.4 Flowchart of the proposed mechanics model.

4.2. Predictions and Experimental Validation

The experimental setup for orthogonal cutting experiments of UD CFRP is shown in Fig. 4.5. A tool holder is designed to clamp the rectangular turning tool into the spindle of the CNC machine tool (Fadal VMC 2216). The angular motion of the spindle is locked to avoid rotation during the cutting process and ensure orthogonal cutting configuration. The model of the cutting insert is Sandvik TPUN 11 03 04 H13A, and the CFRP workpiece is Mitsubishi/UNI/UTS 700/NCT 304-1. UD CFRP plates with different fiber orientations in the range of $[0°, 180°]$ and an interval of $15°$ is used. A three-axis dynamometer (Kistler 9257B) is fixed under the CFRP workpiece to

measure the cutting forces in the tangential and thrust directions. An aluminum plate is used as an adapter between the vise and the dynamometer. The cutting condition, the mechanical properties of the fibers and the matrix materials of the CFRP are listed in Table 4.1. Since this chapter focuses on the mechanics model with different fiber orientations, a constant cutting speed of 5 m/min is used in the experiments, and the effect of high cutting speed on the cutting temperature and matrix property change is not considered. For each cutting condition, in addition to the force measurement, the machined chips are collected and the chip morphology is examined using an optical microscope. Besides, in order to measure the chip formation angle, the machine is stopped when the tool is in cutting with the workpiece, then the tool is retracted to avoid further damage on the chip formation plane, and the 3-D surface topography of the chip formation plane is examined using a confocal laser scanning microscope (Olympus LEXT OLS3100).

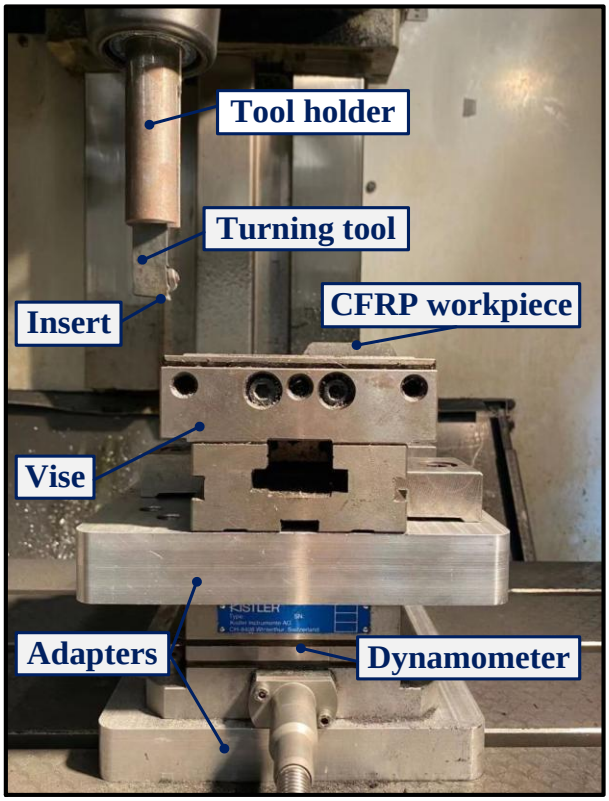

Figure 4.5 Experimental setup of orthogonal cutting of UD CFRP.

Table 4.1 Cutting parameters and mechanical properties of UD CFRP.

Cutting parameters

Fiber orientations $[0°, 180°]$	θ	$0°/180°, 15°, 30°, 45°, 60°,$ $75°, 90°, 105°,$ $120°, 135°, 150°, 165°$
Width of cut	b	$4.4\ mm$
Uncut chip thickness	h	$0.03, 0.06, 0.09, 0.12, 0.15, 0.18\ mm$
Rake angle/ Friction angle	α/β_f	$7°/20°$
Cutting speed	V	$5\ m/min$
Mechanical properties (Mitsubishi Chemical Carbon Fiber and Composite 304-1)		
Shear strength of matrix failure	S_{12}	$97\ MPa$
Tensile strength of matrix failure	X_{22}^t	$83\ MPa$
Tensile strength of fiber failure	X_{11}^t	$2903\ MPa$
Compressive strength of fiber failure	X_{11}^c	$1675\ MPa$
Internal friction coefficient	e_{nl}	-0.3566 [87]

4.2.1. Comparison of the chip formation mechanism

In this section, the predicted chip formation modes and chip formation angle in the entire fiber orientation range of $[0°, 180°]$ from the developed model are presented and compared with the experimental results. To determine the chip formation mechanism, the chip formation modes and their transitions are analyzed in terms of the stress states on the predicted chip formation plane at various fiber orientations. In addition, the relationship between the predicted primary and secondary chip formation modes and the measured chip morphology is discussed.

Fig. 4.6 shows the procedure of chip formation angle measurements using three-dimensional confocal microscopy. The measured results in the figure correspond to 0° fiber orientation, and

the procedures for all other fiber orientations are the same. The color in the three-dimensional topography represents the height of the surface profile, which is composed of the uncut material surface, the machined surface, and the chip formation plane connecting the two surfaces. The image processing software of the confocal microscope is used to obtain the 2D height information in the plane parallel to the cutting direction. The projection of the chip formation plane in the 2D image is fitted by a straight line, and the corresponding chip formation angle (φ) is obtained. The angles are measured using five different chip formation planes at the same uncut chip thickness, and the average value is then calculated. The measured 3-D topographies of the chip formation plane at all fiber orientations are shown in Fig. 4.7.

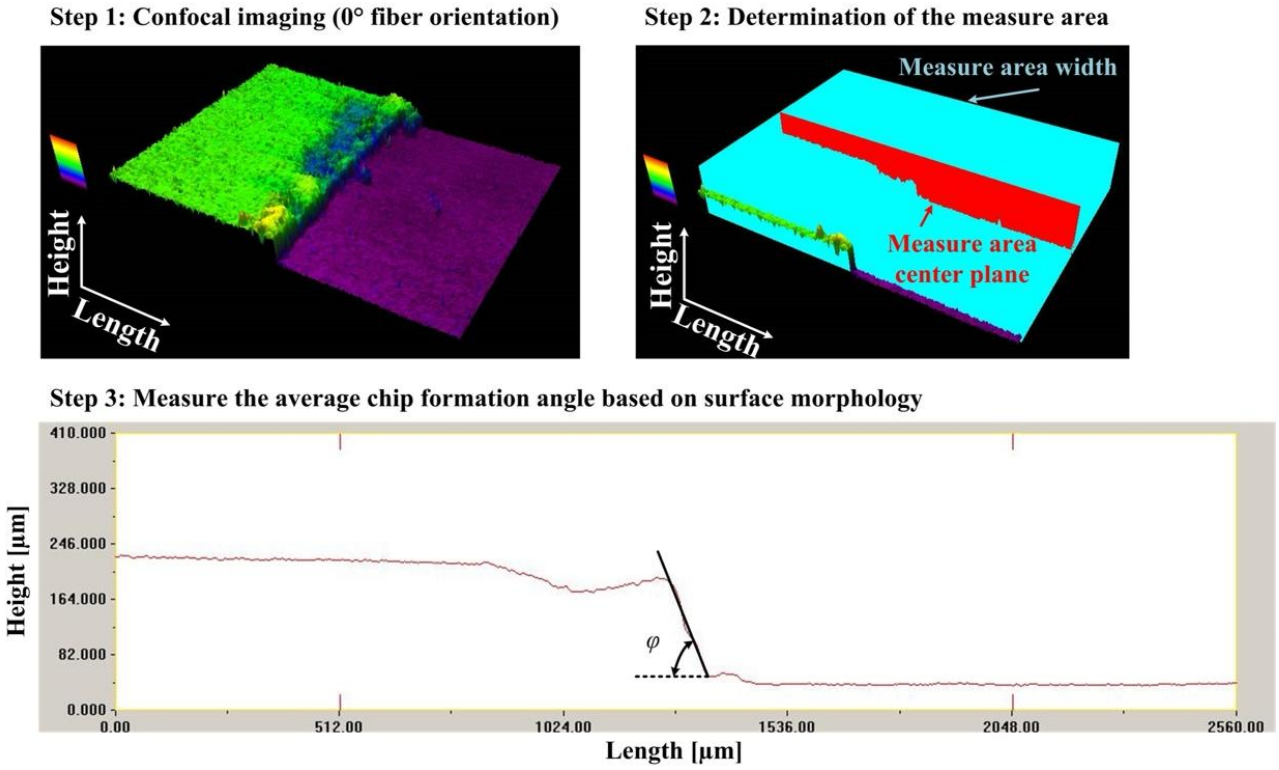

Figure 4.6 Measurement process of chip formation angle.

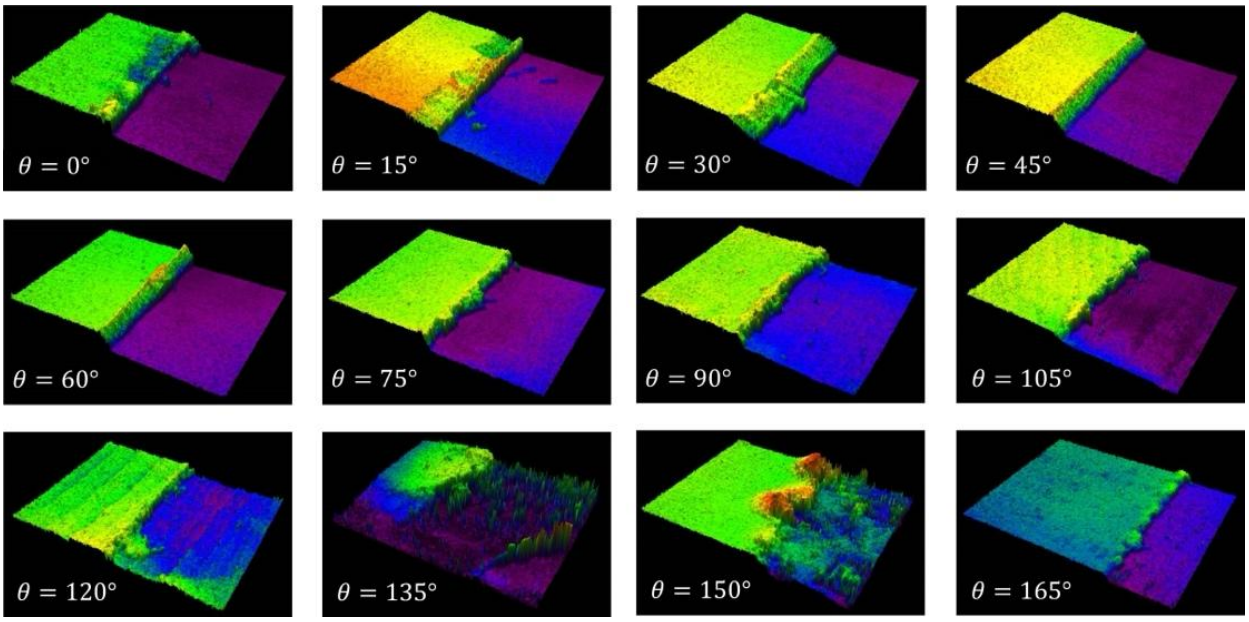

Figure 4.7 Measured three-dimensional confocal microscopy images at various fiber orientations.

The comparison between the predicted chip formation angle from the developed model and the experimental measurements at the fiber orientation range of $[0°, 180°]$ is shown in Fig. 4.8. The results of chip formation angle from Bhatnagar et al. [40] and Zhang et al. [41] applicable to the fiber orientation range of $[0°, 90°]$ are also included. In [30], the chip formation angle is assumed to be the same as the fiber orientation, and [41] models a constant chip formation angle based on the assumption of unity chip ratio. It is found that the proposed model is able to capture the variation of the chip formation angles in the entire fiber orientations, although the prediction errors are comparably larger for the fiber orientations at $0°$, $15°$, and $165°$. Besides, the assumption of Bhatnagar et al. is closer to the measurements at $30°$ and $60°$ fiber orientation, which means that the fracture occurs in the fiber direction. The possible explanation is that the variation of material mechanical properties for corresponding chip formation modes is more significant compared with other fiber orientations owing to the sub-surface damages. The chip formation angle measurements for $135°$ and $150°$ are not given because the chip formation planes can not be identified owing to the severe damage of uncut material in front of the rake face, as shown in Fig. 4.7. The variation of the chip formation angle with respect to the fiber orientation is determined by the change of the CFRP failure modes, which are further analyzed below.

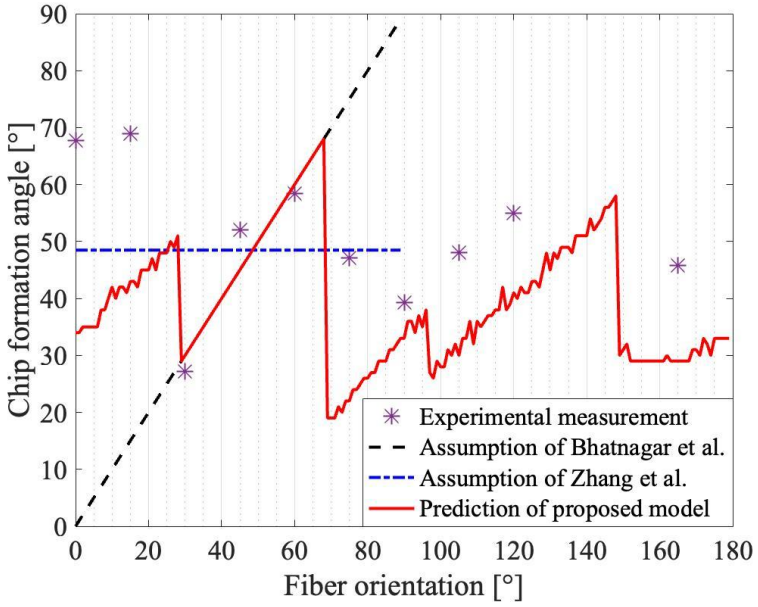

Figure 4.8 Comparison of chip formation angle between predictions and experimental results.

Fig. 4.9 shows the predicted primary and secondary chip formation modes in relation to the chip formation angle variation in the entire range of fiber orientations. In addition, the chip formation modes for all potential chip formation angles at different fiber orientations are presented. For example, Fig. 4.9(a) shows that the primary chip formation mode changes from fiber tension to matrix compression when the potential chip formation angle increases to 30° for 30° fiber orientation. Meanwhile, the secondary chip formation mode changes from matrix compression to fiber compression, as shown in Fig. 4.9(b). The various areas where the predicted chip formation angle is located refer to the primary failure modes at different fiber orientations. The chip formation in the fiber orientation ranges of $[7°, 30°]$ and $[97°, 150°]$ are dominated by matrix compression as the primary chip formation mode. The fiber compression mode which is defined as micro-buckling acts as the secondary chip formation mode. When the fiber orientation increases to the range of $[31°, 96°]$, matrix compression switches to be the secondary chip formation mode, and the primary chip formation mode changes to the fiber tension. The chip formation angle is equal to the fiber orientation in the fiber orientation range of $[30°, 70°]$, which leads to the fracture along the fiber direction. As the fiber orientation exceeds 70°, the difference between the chip formation angle and the fiber orientation gradually increases to 58°. The fiber cutting angle keeps increasing to 59° in the fiber orientation range of $[97°, 150°]$, where the matrix compression and the fiber compression are attributed to the primary and secondary chip formation modes. Besides,

the primary chip formation mode changes to be matrix tension in the fiber orientation range of $[151°, 180°]$. Four fiber orientations (7°, 30°, 97°, and 150°) which correspond to the transitions of the primary chip formation mode when the fiber orientation increases from 0° to 180° are observed: matrix tension → matrix compression → fiber tension → matrix compression → matrix tension. Similarly, Fig. 4.9(b) shows two transitions of the secondary chip formation mode: fiber compression → matrix compression at 30° fiber orientation, and matrix compression → fiber compression at 97° fiber orientation. It is found that the matrix compression failure exists as the primary or secondary chip formation mode in the entire fiber orientation range. In addition, the fiber compression failure which refers to the micro-buckling does not play a role in the primary chip formation mode to cause the primary chip formation, because it requires higher cutting energy to be activated.

The stress state on the chip formation plan determines the fundamental relationship between the material failure modes and the chip formation angle. In this chapter, the chip formation planes at three representative fiber orientations $(0°, 90°, 160°)$ and the directions of stress states in the chip formation coordinate and CFRP ply coordinate are included in Fig. 4.9. The directions of the force components (F_n, F_s) on the chip formation plane are known once the chip formation angle is predicted, because the direction of the resultant force (F_c) only depends on the tool-chip friction angle and tool rake angle. Correspondingly, the directions of the stress state (σ_n, τ_s) on the chip formation plane can be determined by dividing the force components (F_n, F_s) by the area of the chip formation plane (A_c). When the fiber orientation is 0°, the predicted chip formation plane 35°. According to the stress transformation, the normal stress in the transverse direction (σ_{22}) is positive and the stress in the fiber direction (σ_{11}) is negative, which refers to matrix tension failure and fiber compression failure. For 90° fiber orientation, the predicted chip formation angle is approaching the boundary between two chip formation modes (fiber tension and matrix compression), where the chip formation angle is equal to 35°. The primary chip formation mode keeps being fiber tension. Meanwhile, the transverse stress (σ_{22}) in the matrix direction is negative (see Eq. (4.5)), which means that the matrix compression failure occurs as the secondary chip formation mode at the mode transition boundary. When fiber orientation is 160°, the fiber orientation is apparently larger than the chip formation angle. Both the normal stresses in fiber direction (σ_{11}) and transverse direction (σ_{22}) are positive which indicates matrix tension as the

primary and fiber tension as the secondary chip formation modes, respectively. Overall, the change of the stress states on the chip formation plane due to the increase of fiber orientation influences the critical shear stresses needed to initiate one of the failure criteria of CFRP expressed in Eq. (4.8), therefore determining the corresponding chip formation mode. This phenomenon can be quantitatively predicted and analyzed from the developed model.

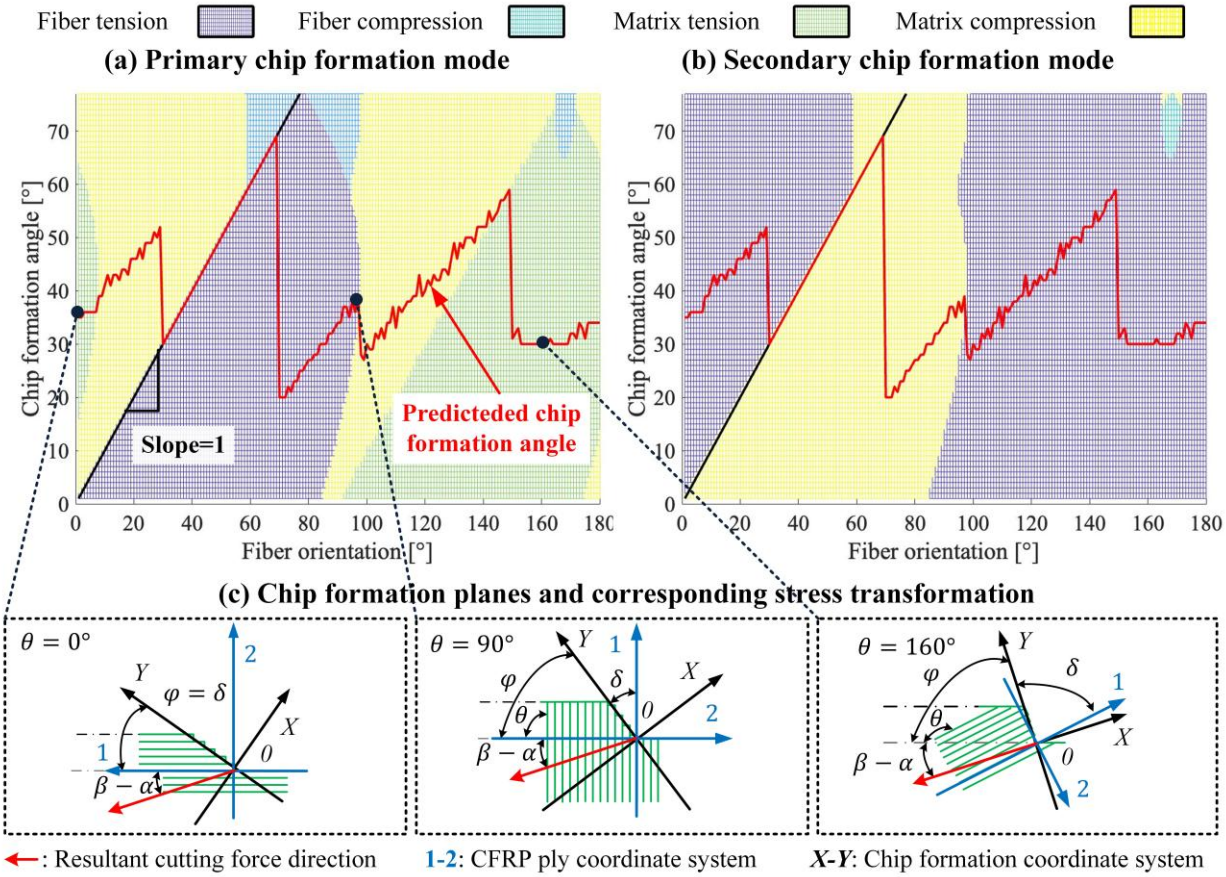

Figure 4.9 Predicted failure mode and chip formation angle. (a) Primary chip formation mode, (b) secondary chip formation mode, and (c) chip formation planes and corresponding stress states in the CFRP ply coordinate.

4.2.2. Experimental examination of machined chips

Experimental examinations on the machined chips are performed to determine the relationship between the distribution of chip morphology in various categories and the predicted chip formation modes. According to the measured morphologies, the machined chips are categorized into: (1) attached chips, (2) block-like chips, (3) belt-like chips, and (4) crushing chips (see Fig. 4.10(a)). Considering that the powder-like chips are generated in the entire fiber orientation range during the fracture process of the chip formation plane, contact between the

formed chips and uncut material, and sliding of the chips on the tool, this category is not included in this analysis. As shown in Fig. 4.10(a), block-like chips are dominant in the fiber orientation range of $[0°, 105°]$, and their sizes decrease significantly with the increase of the fiber orientation. An opposite trend is found for the crushing fibers whose sizes increase when fiber orientation increases from $75°$ to $165°$. The distributions of the chip morphologies (see Fig. 4.10(b)) and their features in different fiber orientation ranges are explained as:

(1) Fiber orientation range of $[0°, 15°]\&[165°, 180°]$

a. Both attached chips and block-like chips are observed;
b. The number of attached chips is larger compared to block-like chips.

(2) Fiber orientation range of $[15°, 75°]$

a. The block-like chips are the only observed chips when the fiber orientation exceeds $45°$;
b. The belt-like chips are the only chip geometry for the fiber orientation range of $[30°, 45°]$ when the uncut chip thickness is equal to and larger than 0.15mm. However, belt-like chips and a small number of block-like chips are observed when the uncut chip thickness is smaller than 0.15 mm.
c. According to the experimental observations, the belt-like chips are another form of block-like chips due to incomplete separation.

(3) Fiber orientation range of $[75°, 105°]$

a. Both block-like chips and crushing chips are observed;
b. The number of crushing chips is larger compared to the block-like chip, and increases with the increase of fiber orientation.

(4) Fiber orientation range of $[105°, 165°]$

a. Only crushing chips are observed;
b. The dimensions of the crushing chips increase with the increase of fiber orientation.

Three fiber orientations (or ranges) corresponding to the transitions of chip morphologies are observed: $15°$ and $165°$ where the chip morphology changes suddenly, $[75°, 105°]$ where the chips of two different morphologies co-exist. The change of chip morphology in these three fiber orientations (or ranges) indicates the transitions of chip formation modes. For the rest of the fiber orientation ranges, only one chip geometry is observed, and the chip formation process is dominated by one primary chip formation mode without chip formation transition. To understand

the distribution of chip morphologies from the perspective of chip formation mechanism, quantitative analyses of the chip formation modes and their transitions with respect to the fiber orientation are shown in Fig. 4.10(c). Because the belt-like chips are another form of block-like chips due to incomplete separation, they are not distinguished in the figure. For the fiber orientation ranges of $[0°, 15°]$ and $[165°, 180°]$, the attached chips represent the majority of chip morphology, and the number of block-like chips increases slightly when the fiber orientation increases. One possible explanation is that the effect of the secondary chip formation mode (fiber compression or buckling failure) becomes more obvious in this fiber orientation range with the increase of fiber orientation. It is also found that the four fiber orientations (or ranges) ($[0°, 15°]$, $[30°, 45°]$, $[75°, 105°]$, and $165°$) corresponding to the transitions of the chip morphologies from the experimental measurements are close to the fiber orientations at the transitions of the chip formation modes (7°, 30°, 97°, and 150°) from the prediction.

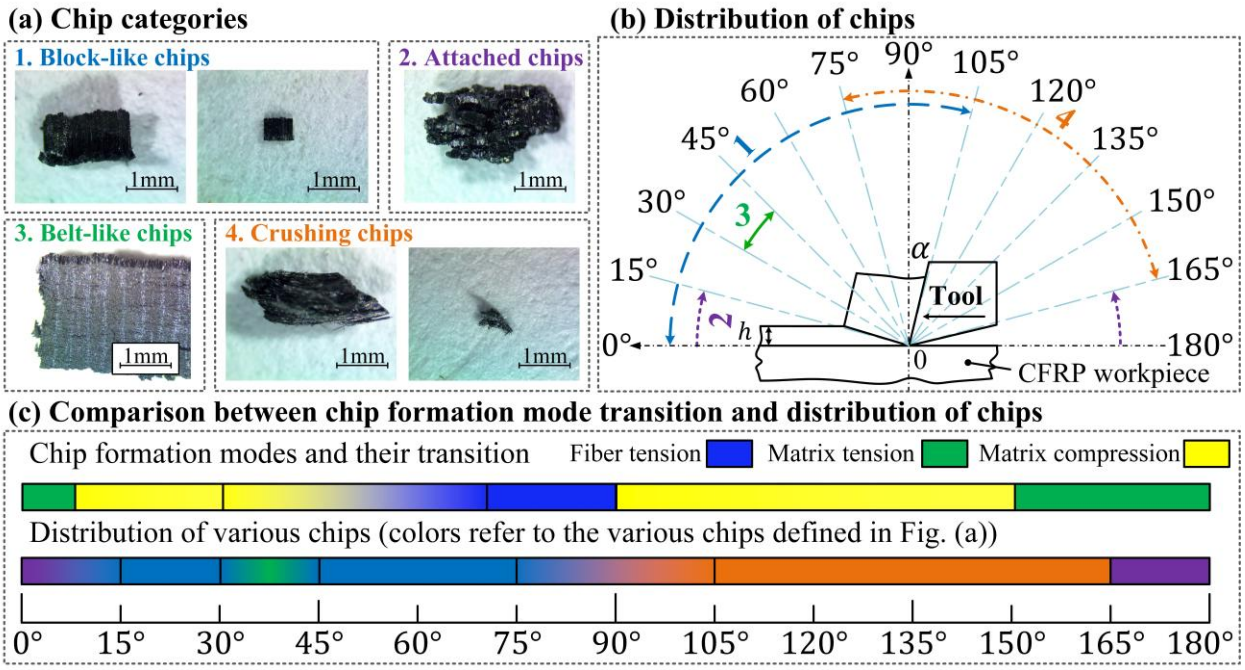

Figure 4.10 Chip geometries and distribution in the CFRP cutting. (a) Chip categories, (b) distribution of chips, and (c) comparison between predicted chip formation mode transition and chip distribution

4.2.3. Comparison of cutting forces

The comparison between the predicted and experimentally measured cutting forces with 0.18 mm uncut chip thickness is presented in Fig. 4.10. The predicted primary chip formation modes

which influence the cutting force variations at different fiber orientation ranges are also included in the figure. In the fiber orientation ranges of $[97°, 150°]$ and $[7°, 30°]$ where the chips are formed owing to the matrix compression, a decrease of the tangential cutting force with the fiber orientation is observed. Considering that the chip formation angle increases with the fiber orientation as shown in Fig. 4.8, the tangential cutting force is mainly influenced by the variation of the internal friction under normal compression on the chip formation plane (see Eqs. (4.10)). Therefore, the decrease of the cutting forces is caused by the decrease of the force component in the cutting firection when the fiber orientation increases, explained by Eq. (4.7). The tangential cutting force reaches a local maximum at $15°$ fiber orientation and starts to increase slightly in the fiber orientation ranges of $[16°, 30°]$, which corresponds to the transition of chip formation mode from matrix compression to fiber tension. In this range, the chip formation angle is larger than the fiber orientation, and the effect of the decrease of shear stress (τ_s) on the tangential cutting force is compensated by the decrease of the terms influenced by the chip formation angle in Eq. (4.10), resulting in a slight decrease of the tangential cutting force. As the fiber orientation increases to the range of $[31°, 69°]$, fiber tension failure is the primary chip formation mode. The chip formation angle is equal to the fiber orientation [30]. Both the tangential and feed cutting forces increase in this fiber orientation range because the increase of the shear strength owing to the internal friction blocks the occurrence of the matrix failure and it is easier to activate the fiber tension failure. The difference between the chip formation angle and fiber orientation enlarges from $0°$ to $50°$ as the fiber orientation increases beyond $70°$ (see Fig. 4.8), which increases the variation of the tangential cutting force. Considering the angle between the direction of resultant cutting force and chip formation plane increases from $32°$ to $51°$, the normal compression on the chip formation plane or in the transverse direction increases which blocks the occurrence of matrix failure mode by providing the larger internal friction. Therefore, the tension stress (σ_{11}) need to increase with the fiber orientation and form the chips according to the fiber tension failure criterion in Eq. (4.6). When the fiber orientation exceeds $97°$, the chip formation mode changes from fiber tension to matrix compression, and a significant decrease of the tangential cutting force with the fiber orientation is observed. It is because the enhancement effect of the normal compression on the shear stress under the matrix compression failure criterion is not large enough to change the failure mode to the fiber tension. According to Eq. (4.8), this enhancement effect decreases when the fiber orientation increases in the range of $[97°, 150°]$, causing the decrease of the tangential

cutting force. A slight decrease of tangential cutting force is observed in the fiber orientation range $[150°, 180°]$, where the matrix tension is the primary chip formation mode. It is because the shear strength is a constant under the matrix tension failure (Eq. 4.7), and the chip formation angle is also a constant. The results show that the experimentally measured tangential cutting forces are close to zero at $135°$ and $150°$ fiber orientations. This is because of severe bulk damages of the CFRP workpiece due to the cutting process at these fiber orientations, as also demonstrated from the three-dimensional surface profile of the chip formation plane in Fig. 4.7. The measured feed force shares the same trend with the tangential cutting force, while apparent errors are noticed for fiber orientations of $15°$ and $30°$. In the experiment, the measured feed force is composed of the feed force components in the chip formation region and the pressing region at the tool edge. The force component in the pressing region has significant fluctuations because the depth of the sub-surface damage varies with the fiber orientation and the uncut chip thickness, which change the mechanical properties of CFRP in the pressing region. However, this phenomenon does not have a major effect on the tangential cutting force, owing to its relatively smaller value compared to the feed force component under Coulomb friction condition at the tool edge.

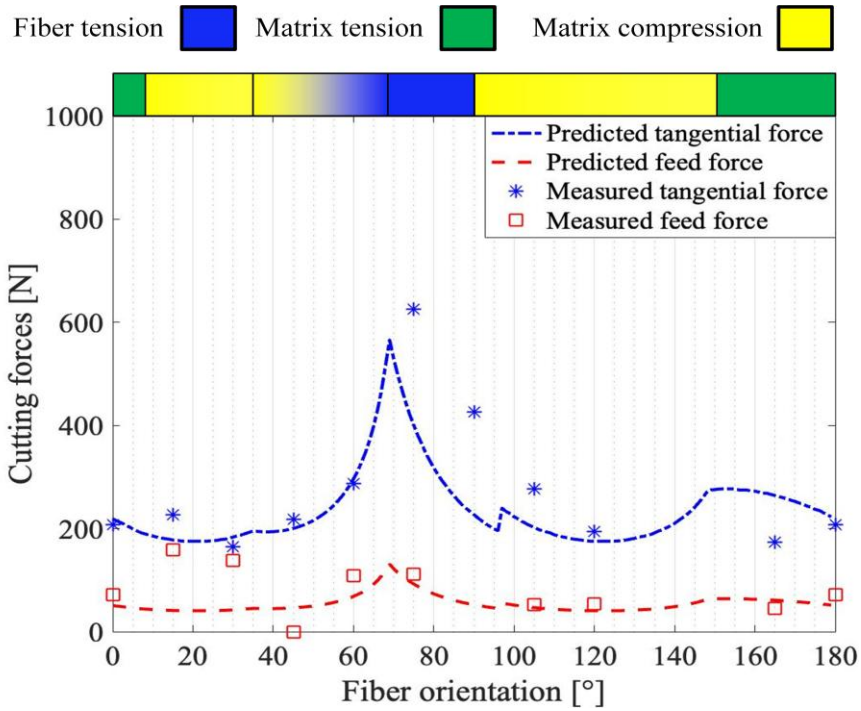

Figure 4.11 Comparison of predicted cutting forces and experimental measurements.

4.3. Conclusion

This work presents a unified analytical mechanics model to predict the chip formation mechanism, chip formation angle, and cutting forces in the entire fiber orientation range. Instead of pre-defining the chip formation modes in specific fiber orientation ranges, the model predicts the stress state on the chip formation plane and determines the chip formation mode based on general CFRP failure criteria. The minimum energy principle is used to identify the chip formation angle with respect to the fiber orientation. Experimental measurements on the chip formation plane and the chip formation angle are performed, and the chip morphologies and cutting forces are measured to evaluate the predictions of the mechanics model.

The following main conclusions are drawn:

(1) The stress state on the chip formation plane varies with the fiber orientation, therefore changing the CFRP failure criteria (fiber tension, fiber compression, matrix tension, and matrix compression) required for the chip formation. The orientation of the chip formation plane defined by the chip formation angle corresponds to the minimum energy consumed in the cutting process. The primary chip formation modes include matrix compression, fiber tension, and matrix tension. The transition of the chip formation mode corresponds to the change of the failure criterion at specific fiber orientations.

(2) The predicted change of chip formation modes with the fiber orientation influences the morphologies of the machined chip. There exist three fiber orientations (or ranges) corresponding to the transitions of the chip morphology categories in the fiber orientation range of $[0°, 180°]$, and they match with the fiber orientations for the transitions of CFRP failure mode.

(3) The developed model is able to predict the variations of the cutting forces with the fiber orientation, which are contributed by the changes of the chip formation angle and the shear stress on the chip formation plane. The transitions of the chip formation modes at the fiber orientations of $7°, 30°, 97°,$ and $150°$ cause the changes of force variation trend with the increase of fiber orientation.

5. Fracture Angle Prediction of UD CFRP Using Energy Method

In Chapter 4, it is found that the chip formation is highly dominated by matrix compression, fiber tension, and matrix tension. For the matrix compression criterion in Eq. (4.7), the 'internal friction' is introduced to model the enhancement effect of the compression on the shear strength. Even though it achieves accurate predictions for chip formation modes and angle, the existence of 'internal friction' is questioned. It is because the physical meaning of 'internal friction' in the CFRP material can not be explained.

Here, an alternative method for modeling the matrix failure modes of UD CFRP based on the energy approach is proposed. The variation of the complementary free energy density with the potential fracture angle is modeled by considering the stress status on the fracture planes. The failure of the material starts from the distributed microcracks inside the matrix and fiber–matrix interface. The direction of crack propagation in the damage evolution stage determines the fracture angle. Based on the CDM theory, the effect of the cracks on the material behavior is characterized as a damage variable in the range from zero to unity, where zero represents no damage occurrence and unity represents complete damage of the matrix material. Correspondingly, the fracture plane is divided into an undamaged elastic section and a damaged section. The variation in the complementary free energy density with the potential fracture angle during the failure process is expressed as a function of the damage variable. Based on the energy principle, the fracture angle is predicted by the fracture plane direction, which corresponds to the fastest dissipation of the complementary free energy density.

5.1. Prediction of Fracture Angle Based on Energy Method

Fig. 5.1 shows the UD CFRP components under the ply coordinate ($X_1 - X_2 - X_3$) and the stress states on a fracture plane parallel to the fiber direction, with the fracture angle (θ_p) to be determined. Fiber failure, including tensile and compressive failure (kinking), is mainly initiated by the normal stress in the fiber direction (σ_{11}). Matrix failure modes, such as shearing failure, tensile failure, and their combinations, are caused by other stress components, including in-plane shear stress (τ_{12}, τ_{13}), out-of-plane shear stress (τ_{23}), and transversely normal stress (σ_{22}, σ_{33}). The failure behavior of the matrix depends directly on the stress components on the fracture plane (σ_{nn}, τ_{nt}, τ_{nl}). In this chapter, the stress state was divided into tensile and compressive ranges,

depending on the direction of the normal stress on the fracture plane. Correspondingly, matrix failure was divided into tensile and compressive modes.

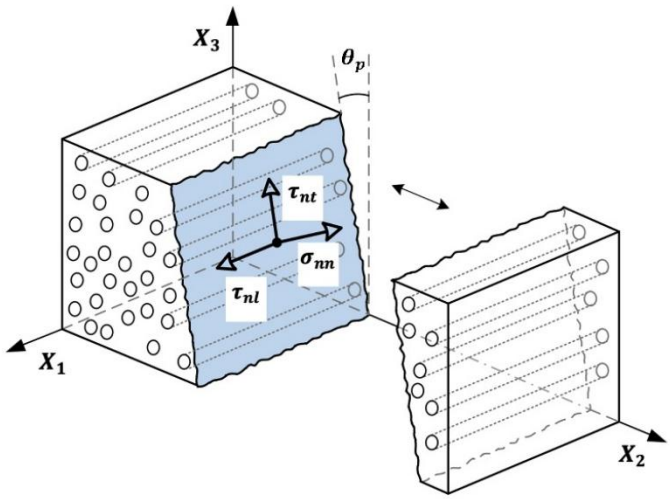

Figure 5.1 Stress state on a potential plane.

5.2. Coupled friction-damage model for matrix failure

The damage of CFRP material is initiated at weaker locations [70], such as voids and defects in the matrix or the fiber–matrix interface before the stresses reach the strength limit. The majority of early-stage cracks are formed in the vicinity of the fiber–matrix interface owing to its lower bonding strength compared to the strengths of the fiber and matrix. The remaining microcracks are distributed inside the matrix material [71]. As the stress increases, more cracks are formed and concentrated, which causes a gradual occurrence of the fracture plane. The fracture angle corresponds to the direction of crack propagation with the lowest material resistance. In this chapter, CDM theory was used to model the mechanical behavior of CFRP during the failure process, and the effect of the microdefects on the mechanical properties was expressed as the effective stress at the macroscale. The effective stress describes the degradation of the modulus with a damage variable represented by the ratio of the damaged area A_0 to the original undamaged area A. The external load can only be resisted by stresses generated in the undamaged area during material deformation, until complete damage occurs when the material loses its ability to bear the load.

According to the experimental observations of failure tests of CFRP [58], the fracture plane was found to be normal to the loading direction under pure transverse tension. For pure transverse

compression, the fracture angle was observed to be in the range of 50°–55°. Experimental results have demonstrated that CFRP failure under transverse compression is dominated by the shear failure of the matrix [72]. In this chapter, a bilinear law was assumed to describe the effect of compression on the material shear behavior on a potential fracture plane, as shown in Fig. 5.2. When the compressive stress (σ) is zero, the shear stress–strain relationship follows a triangular law, and the stress–strain relationship proceeds from linearly elastic until damage initiation occurs when the strain reaches s_o. As the strain increases further, the effective shear stress decreases linearly until complete failure when the strain is s_f. When the normal compressive stress is applied, the damaged area generates two contacting surfaces, and the friction between the two surfaces provides additional resistance to shear deformation. A damage variable (d) is introduced in the damage evolution stage and is expressed as

$$d = \frac{s_f}{s}\left(\frac{s - s_o}{s_f - s_o}\right), d \in [0,1] \tag{5.1}$$

The damage variable starts from zero at the damage initiation strain (s_o) to unity at the complete failure strain (s_f). Two shear stress components on the potential fracture plane must be included: (1) the elastic shear stress (τ) contributed by the undamaged area, and (2) the frictional shear stress ($\mu_m\sigma$) contributed by the contacting surfaces in the damaged area, where μ_m is the Coulomb friction coefficient between the fractured surfaces. Because the damage growth results in larger fractured surfaces, the resultant shear stress is influenced by the increased friction in the damaged area when compression is applied. Therefore, the overall shear stress on the fracture plane to balance the external stress is expressed as

$$\tau_f = (1 - d)\tau + d(\mu_m\sigma) \tag{2}$$

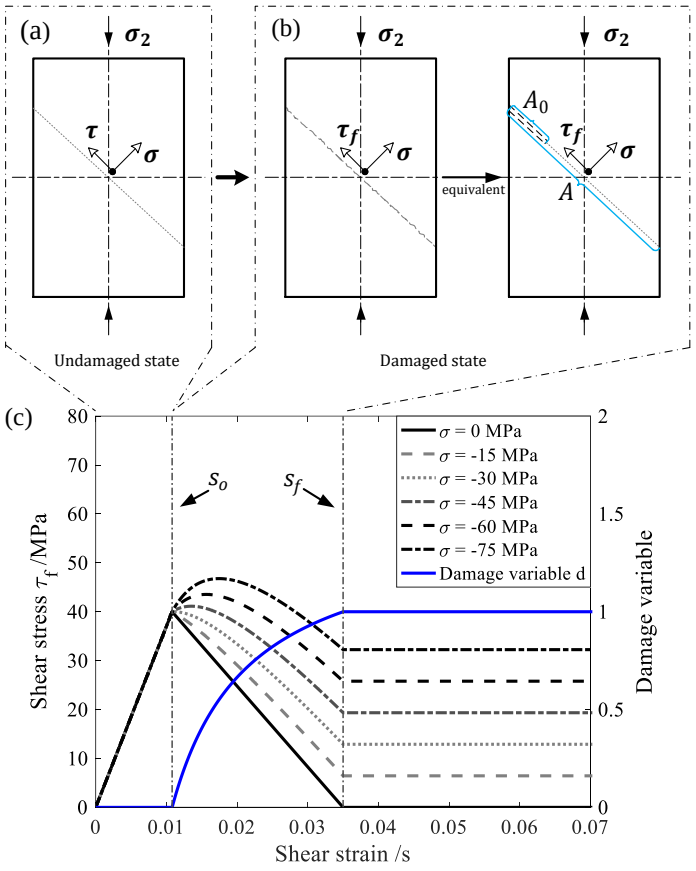

Figure 5.2 Shear stress–strain behavior based on the friction damage model.

Fig. 5.2(c) shows the relationship between the overall shear stress and the shear strain under different compressive normal stress values obtained from Eq. (5.2). Because of the frictional resistance in the damaged area, the shear stress (τ_f) increases in the damage evolution period when the compressive stress (σ) is applied, compared with the condition with no normal stress. Moreover, the shear stress (τ_f) reaches a constant value after the complete failure of the material because of the limited contact area of the fractured surfaces. When the magnitude of the compressive stress (σ) has smaller values (e.g., $\sigma = -15$ MPa $and -30$ MPa) as shown in Fig. 5.2(c), the stress–strain curve decreases with the increase in shear strain after the damage initiation. However, when the magnitude of the compressive normal stress becomes larger (e.g., $\sigma = -45, -60, and -75\ MPa$), the shear stress increases after the damage initiation and then decreases as the shear strain increases further. Therefore, the overall shear stress depends on the combined effects of the elastic shear stress in the undamaged area and the compressive normal

stress in the damaged area. This stress–strain relationship based on the friction damage model is used to determine the fracture angle using the energy method, with the details described below.

5.3. Energy method for fracture angle prediction

The transformed stress tensor with respect to the fracture plane coordinate defined by the fracture angle $\theta \in [-90°, 90°]$ is calculated from the loading stress in the ply coordinate as

$$\boldsymbol{\sigma_{NLT}} = \boldsymbol{T}(\theta_p)\boldsymbol{\sigma_{123}}\boldsymbol{T}(\theta_p)^{\boldsymbol{T}} \tag{5.3}$$

where $\boldsymbol{\sigma_{123}}$ is the stress tensor in the ply coordinate system. The transformation matrix $T(\theta_p)$ is expressed as

$$T(\theta_p) = \begin{bmatrix} 1 & 0 & 0 \\ 0 & cos(\theta_p) & sin(\theta_p) \\ 0 & -sin(\theta_p) & cos(\theta_p) \end{bmatrix} \tag{5.4}$$

Therefore, the elements of the stress tensor $\boldsymbol{\sigma_{NLT}}$ in the transformed coordinate system are

$$\begin{bmatrix} \sigma_{ll} \\ \sigma_{nn} \\ \sigma_{tt} \\ \tau_{nl} \\ \tau_{nt} \\ \tau_{tl} \end{bmatrix} = \begin{bmatrix} 1 & 0 & 0 & 0 & 0 & 0 \\ 0 & \cos^2\theta_p & \sin^2\theta_p & 0 & 2\cos\theta_p \sin\theta_p & 0 \\ 0 & \sin^2\theta_p & \cos^2\theta_p & 0 & -2\cos\theta_p \sin\theta_p & 0 \\ 0 & 0 & 0 & \cos\theta_p & 0 & \sin\theta_p \\ 0 & -\cos\theta_p \sin\theta_p & \cos\theta_p \sin\theta_p & 0 & \cos^2\theta_p - \sin^2\theta_p & 0 \\ 0 & 0 & 0 & -\sin\theta_p & 0 & \cos\theta_p \end{bmatrix} \begin{bmatrix} \sigma_{11} \\ \sigma_{22} \\ \sigma_{33} \\ \tau_{12} \\ \tau_{23} \\ \tau_{13} \end{bmatrix} \tag{5.5}$$

Because the fracture angle (θ_p) under an arbitrary three-dimensional loading is unknown in advance, the stress state $\boldsymbol{\sigma_{NLT}}$ must be calculated for the entire potential fracture angle range of $[-90°, 90°]$. The mechanical behavior of the potential fracture plane depends on the normal stress direction—that is, the closed cracks caused by the compressive normal stress provide additional friction or shear resistance, while no shear stress can be transferred through the opened fractured surfaces under tension. During the deformation process, local damage, such as debonding of the fiber–matrix interface or failure of matrix material, starts at a lower stress than the ultimate strength owing to the existence of microdefects, voids, and misalignment of the fibers. Considering the transverse isotropy of the UD CFRP, the complementary free energy density [73, 74] for the undamaged material in the transformed coordinate ($l - n - t$) is represented as

$$\psi = \frac{\sigma_{ll}^2}{2E_1} + \frac{\sigma_{nn}^2 + \sigma_{tt}^2}{2E_2} - \frac{v_{12}}{E_1}\sigma_{ll}\sigma_{nn} - \frac{v_{13}}{E_1}\sigma_{ll}\sigma_{tt} - \frac{v_{23}}{E_2}\sigma_{nn}\sigma_{tt} + \frac{\tau_{nl}^2}{2G_{12}} + \frac{\tau_{tl}^2}{2G_{12}} + \frac{\tau_{nt}^2}{2G_{23}} \tag{5.6}$$

$$+[\alpha_{11}\sigma_{ll} + \alpha_{22}(\sigma_{nn} + \sigma_{tt})]\Delta T + [\beta_{11}\sigma_{ll} + \beta_{22}(\sigma_{nn} + \sigma_{tt})]\Delta M$$

where E_1 and E_2 are the longitudinal and transverse elastic moduli of the material, respectively. Here, $v_{i,j}(i,j = 1,2,3)$ represents Poisson's ratio in the related directions, G_{12} and G_{13} are the in-plane shear moduli of the material, G_{23} is the out-of-plane shear modulus, α_{11} and α_{22} are the coefficients of thermal expansion in the longitudinal and transverse directions, respectively, β_{11} and β_{22} are the coefficients of hygroscopic expansion in the longitudinal and transverse directions, respectively, and ΔT and ΔM are the differences between the CFRP temperature and moisture content, respectively, with respect to the reference values. The closed cracks provide additional friction on the potential fracture plane under compression ($\sigma_{nn} < 0$), while the friction does not play a role in the tension ($\sigma_{nn} \geq 0$) condition. In this chapter, the effective stresses in the undamaged area of the transformed potential plane are defined as

$$\begin{aligned}
\tilde{\sigma}_{nn} &= \frac{\sigma_{nn}}{1 - d_2 H(\sigma_{nn})} \\
\tilde{\tau}_{nl} &= \frac{\tau_{nl} - d_2 t(\tau_{nl}) C_1 \mu_{nl} \sigma_{nn} H(-\sigma_{nn})}{1 - d_2} \\
\tilde{\tau}_{nt} &= \frac{\tau_{nt} - d_2 t(\tau_{nt}) C_2 \mu_{nt} \sigma_{nn} H(-\sigma_{nn})}{1 - d_2}
\end{aligned} \tag{5.7}$$

where $H(\cdot)$ is the Heaviside step function used to determine the effect of tensile or compressive normal stress on the shear stresses along the fracture plane, μ_{nl} and μ_{nt} are the Coulomb friction coefficients in the corresponding directions, respectively, d_2 is the damage variable of matrix failure, and C_1 and C_2 are the ratios of the friction components in the longitudinal and transverse directions, respectively, with respect to the resultant frictional shear stress, defined as

$$C_1 = \frac{|\tau_{nl}|}{\sqrt{\tau_{nl}^2 + \tau_{nt}^2}}, C_2 = \frac{|\tau_{nt}|}{\sqrt{\tau_{nl}^2 + \tau_{nt}^2}}. \tag{5.8}$$

The step function $t(\cdot)$ used to determine the direction of frictional stresses on the fracture plane is defined as

$$t(x) = \begin{cases} 1, x < 0 \\ -1, x \geq 0 \end{cases}$$

Therefore, the proposed complementary free energy density based on the effective stresses in the transformed coordinate system is given as

$$\psi = \frac{\sigma_{ll}^2}{2(1-d_1)E_1} + \frac{\sigma_{nn}^2}{2[1-d_2\cdot H(\sigma_{nn})]E_2} + \frac{\sigma_{tt}^2}{2E_2} - \frac{v_{12}}{E_1}\sigma_{ll}\sigma_{nn} - \frac{v_{13}}{E_1}\sigma_{ll}\sigma_{tt} - \frac{v_{23}}{E_2}\sigma_{nn}\sigma_{tt} + \frac{[\tau_{nl} - d_2 t(\tau_{nl})C_1\mu_{nl}\sigma_{nn}H(-\sigma_{nn})]\tau_{nl}}{2(1-d_2)G_{12}} + \frac{[\tau_{nt} - d_2 t(\tau_{nt})C_2\mu_{nt}\sigma_{nn}H(-\sigma_{nn})]\tau_{nt}}{2(1-d_2)G_{23}} + \frac{\tau_{tl}^2}{2G_{13}} + [\alpha_{11}\sigma_{ll} + \alpha_{22}(\sigma_{nn}+\sigma_{tt})]\Delta T + [\beta_{11}\sigma_{ll} + \beta_{22}(\sigma_{nn}+\sigma_{tt})]\Delta M \tag{5.9}$$

where d_1 is the damage variable of fiber failure. The stress statuses in the damaged area under tension ($\sigma_{nn} \geq 0$) and compression ($\sigma_{nn} < 0$) failure cases are shown in Fig. 5.3.

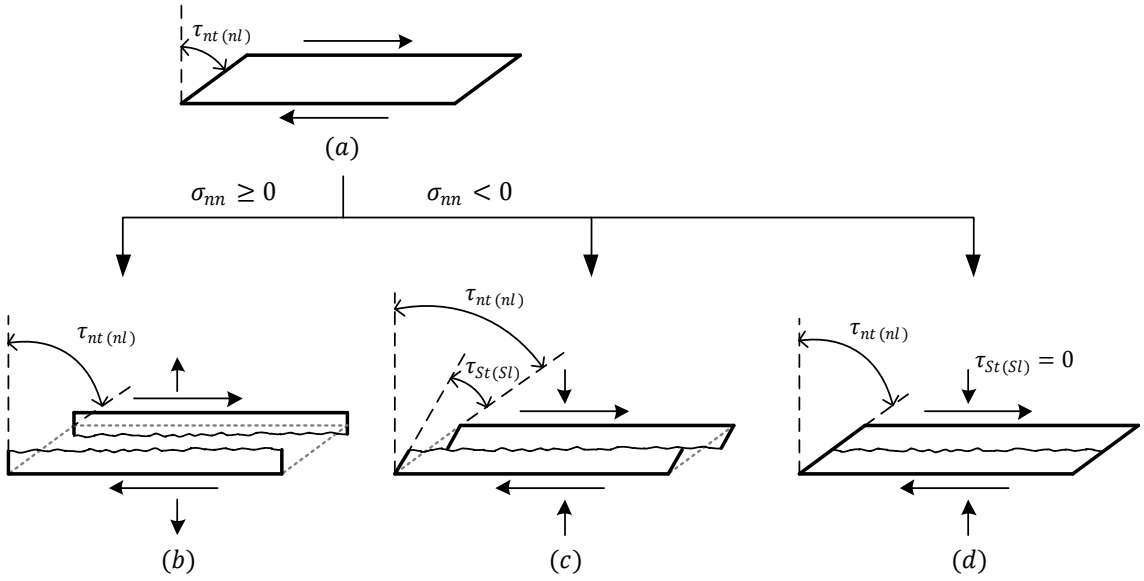

Figure 5.3 Stress states in the damaged area under shear: (a) general shear state, (b) shear/tension state, (c) shear/compression state with sliding movement, and (d) shear/compression state without sliding movement.

(1) Tension case: As shown in Fig. 5.3(b), because the opened fractured surfaces in the damaged area cannot transfer the traction and friction, it is only necessary to include the complementary free energy density of the undamaged area, expressed as

$$\psi = \frac{\sigma_{ll}^2}{2(1-d_1)E_1} + \frac{\sigma_{nn}^2}{2(1-d_2)E_2} + \frac{\sigma_{tt}^2}{2E_2} - \frac{v_{12}}{E_1}\sigma_{ll}\sigma_{nn} \tag{5.10}$$

$$-\frac{v_{13}}{E_1}\sigma_{ll}\sigma_{tt}-\frac{v_{23}}{E_2}\sigma_{nn}\sigma_{tt}+\frac{\tau_n^2}{2(1-d_2)G_{12}}+\frac{\tau_{tl}^2}{2G_{13}}+\frac{\tau_{nt}^2}{2(1-d_2)G_{23}}$$
$$+[\alpha_{11}\sigma_{ll}+\alpha_{22}(\sigma_{nn}+\sigma_{tt})]\Delta T+[\beta_{11}\sigma_{ll}+\beta_{22}(\sigma_{nn}+\sigma_{tt})]\Delta M$$

Therefore, the dissipation rate of the complementary free energy density with an increase in the damage variable is given as

$$Y=\frac{\partial\psi}{\partial d_2}=\frac{1}{2(1-d_2)^2}(\frac{\sigma_{nn}^2}{E_2}+\frac{\tau_{nl}^2}{G_{12}}+\frac{\tau_{nt}^2}{G_{23}}) \tag{5.11}$$

(2) Compression case: When the normal stress σ_{nn} is compressive, the friction on the fractured surfaces resists the material in the damaged area to further deformation—that is, the shear stress originally provided by the undamaged material changes to the frictional stress in the damaged area because of compression. Therefore, the shear deformation in the undamaged area and the frictional resistance in the damaged area determine the energy stored in the material. To determine the complementary free energy density considering the friction at the fractured surfaces, the frictional stress on the fractured surfaces must be obtained. When a sliding movement occurs, as shown in Fig. 3(c), the frictional stress of the material in the damaged area is given as

$$\tau_{nt}=G_{23}(\varepsilon_{nt}-\varepsilon_{St})=\mu_{nt}\sigma_{nn}, \qquad (\varepsilon_{St}\neq 0) \tag{5.12}$$

where G_{23} is the out-of-plane shear modulus, and ε_{nt} and ε_{St} are the shear and sliding strains on the fractured surfaces, respectively.

The shear stress (τ_{nt}) in the damaged material depends on the sliding strain ε_{St} and reaches a maximum when the sliding strain reaches zero, as shown in Fig. 5.3(d). In this case, the friction under a large transverse compressive stress resists the relative sliding movement on the fractured surfaces. Correspondingly, the effective shear stress is lower than the sliding friction ($\mu_{nt}\sigma_{nn}$) and is determined by the shear deformation itself. Because the minimum sliding strain (ε_{St}) is zero, the maximum shear stress provided by the material is

$$\tau_{nt}=G_{23}\varepsilon_{nt}, \qquad (\varepsilon_{St}=0). \tag{5.13}$$

The procedure for calculating the in-plane shear stress (τ_{nl}) is the same as that for the out-of-plane shear stress (τ_{nt}). Therefore, the free energy density under compressive normal stress—see Fig. 5.3(d)—is updated as

$$\psi = \frac{\sigma_{ll}^2}{2(1-d_1)E_1} + \frac{\sigma_{nn}^2}{2E_2} + \frac{\sigma_{tt}^2}{2E_2} - \frac{v_{12}}{E_1}\sigma_{ll}\sigma_{nn} - \frac{v_{13}}{E_1}\sigma_{ll}\sigma_{tt} - \frac{v_{23}}{E_2}\sigma_{nn}\sigma_{tt} + \frac{\tau_{nl}^2}{2G_{12}} + \frac{\tau_{tl}^2}{2G_{13}} + \frac{\tau_{nt}^2}{2G_{23}} + [\alpha_{11}\sigma_{ll} + \alpha_{22}(\sigma_{nn} + \sigma_{tt})]\Delta T + [\beta_{11}\sigma_{ll} + \beta_{22}(\sigma_{nn} + \sigma_{tt})]\Delta M \tag{5.14}$$

Eq. (5.14) shows that the free energy is no longer related to the damage variable d_2 because the fractured surfaces cannot move relative to each other, which makes the mechanical behavior in the damaged material the same as in the undamaged material. Therefore, the free energy density does not dissipate during the loading process, even after damage initiation. Correspondingly, the dissipation rate of the free energy at the beginning of the damage propagation is calculated as

$$Y = \frac{\partial \psi}{\partial d_2} = 0. \tag{5.15}$$

This means that the free energy of the material is not released, even after damage initiation and propagation. However, in the case shown in Fig. 5.3(c), the fractured surfaces exhibit relative movement to provide friction under compression. Thus, the complementary free energy density and its dissipation rate are

$$\psi = \frac{\sigma_{ll}^2}{2(1-d_1)E_1} + \frac{\sigma_{nn}^2}{2E_2} + \frac{\sigma_{tt}^2}{2E_2} - \frac{v_{12}}{E_1}\sigma_{ll}\sigma_{nn} - \frac{v_{13}}{E_1}\sigma_{ll}\sigma_{tt} - \frac{v_{23}}{E_2}\sigma_{nn}\sigma_{tt} + \frac{[\tau_{nl} - d_2 t(\tau_{nl})C_1\mu_{nl}\sigma_{nn}]\tau_{nl}}{2(1-d_2)G_{12}} + \frac{\tau_{tl}^2}{2G_{13}} + \frac{[\tau_{nt} - d_2 t(\tau_{nt})C_2\mu_{nt}\sigma_{nn}]\tau_{nt}}{2(1-d_2)G_{23}} + [\alpha_{11}\sigma_{ll} + \alpha_{22}(\sigma_{nn} + \sigma_{tt})]\Delta T + [\beta_{11}\sigma_{ll} + \beta_{22}(\sigma_{nn} + \sigma_{tt})]\Delta M \tag{5.16}$$

$$Y = \frac{\partial \psi}{\partial d_2} = \frac{1}{(1-d_2)^2}\left(\frac{[\tau_{nl} - t(\tau_{nl})C_1\mu_{nl}\sigma_{nn}]\tau_{nl}}{2G_{12}} + \frac{[\tau_{nt} - d_2 t(\tau_{nt})C_2\mu_{nt}\sigma_{nn}]\tau_{nt}}{2G_{23}}\right) \tag{5.17}$$

Here, the dissipation rate Y represents the variation in the free energy density on a potential fracture plane during the failure process. The differential defines the relationship between the increment of the damage variable d_2 and the energy dissipation rate. In Eqs. (5.11), (5.15), and (5.17), the stresses corresponding to the fracture plane ($\sigma_{nn}, \tau_{nl}, \tau_{nt}$) are functions of the stresses in the ply coordinate system and the fracture angle caused by stress transformation. In addition, the coefficients of the term $(1-d_2)^{-2}$ in Eqs. (5.11) and (5.17) determine the maximum energy dissipation rate. Therefore, the variation in the dissipation rates with respect to the fracture angle was obtained. In this chapter, the fracture angle is determined when the nonnegative dissipation rate (Y) of a fracture plane reaches the maximum—that is, the direction that achieves the highest

energy dissipation rate. The energy dissipation rate with the potential fracture angle in the range of $[-90°, 90°]$ is predicted, and the value corresponding to the maximum dissipation rate represents the predicted fracture angle.

5.4. Results and Discussion

The combined matrix failure criteria [75, 76] based on Hashin's matrix tension failure criterion [57] and Puck's matrix compression failure criterion [58] have been extensively used in the literature to predict the failure of CFRP materials. Compared with the predicted and experimental data of the combined matrix failure criteria, the fracture angle prediction based on the proposed energy-based method is validated and discussed using the mechanical parameters of CFRP listed in Table. 5.1.

Table 5.1 Parameters used for the comparison [76, 77].

Mechanical properties used in the proposed energy-based model			
Moduli			
	Young's modulus	E_2	10.3 GPa
	In-plane shear modulus	G_{12}, G_{13}	6.0 GPa
	Out-of-plane shear modulus	G_{23}	3.7 GPa
Friction coefficients			
	In-plane friction coefficient	μ_{nl}	0.2
	Out-of-plane friction coefficient	μ_{nt}	0.43
Mechanical properties used in the combined Hashin's and Puck's model			
Strengths			
	Transverse tensile strength	Y_t	82 MPa
	Transverse compressive strength	Y_c	236 MPa
	In-plane shear strength	S_{12}	90 MPa
	Out-of-plane shear strength	S_{23}	40 MPa
		S_{23}^*	89 MPa

The combined matrix failure criteria for the matrix modes based on Hashin's tension failure and Puck's compression failure criteria are given as

$$p(\theta) = \begin{cases} \left(\frac{\sigma_{nn}}{Y_t}\right)^2 + \left(\frac{\tau_{nl}}{S_{12}}\right)^2 + \left(\frac{\tau_{nt}}{S_{23}}\right)^2 = 1, & for\ \sigma_{nn} \geq 0 \\ \left(\frac{\tau_{nl}}{S_{12} - e_{nl}\sigma_{nn}}\right)^2 + \left(\frac{\tau_{nt}}{S_{23}^* - e_{nt}\sigma_{nn}}\right)^2 = 1, & for\ \sigma_{nn} < 0 \end{cases} \tag{5.18}$$

where Y_t, S_{12}, and S_{23} are the transverse tensile strength, in-plane shear strength, and out-of-plane shear strength, respectively, e_{nl} and e_{nt} are the in-plane and out-of-plane "internal friction"-related coefficients, respectively [78, 79], and S_{23}^* is the calculated out-of-plane shear strength for Puck's compression criterion,

$$S_{23}^* = \frac{Y_c}{2tan\,(\theta_f)} \tag{5.19}$$

where Y_c is the transverse compression strength, and θ_f is the measured fracture angle. Puck's failure criterion determines the failure envelope for the stress state at all potential fracture angles θ_p. Matrix failure occurs when the maximum value of $p(\theta_p)$ exceeds unity. The fracture angle prediction flowcharts for the proposed method and the existing combined prediction method are presented in Fig. 5.4. The combined prediction method assumes that the increase of shear strength is owing to the 'internal friction' under compression without explaining the source of this enhancement effect. Different from the strength-based method, the proposed method considers the Coulomb friction on the fractured surfaces in the damaged area based on the framework of CDM. The formation of friction reduces the effective stress left in the undamaged area which affects the propagation direction of the fracture. The fracture angle is determined by the effective stress in the undamaged area and Coulomb friction in the damaged area. Therefore, the fracture angle is predicted based on the maximum energy dissipation principle rather than the strength-based approach. Considering the numerical efficiency and reliability of the algorithm, the Selective Range Golden Section Search algorithm (SRGSS) [80] is adapted for two methods to localize the maximum values.

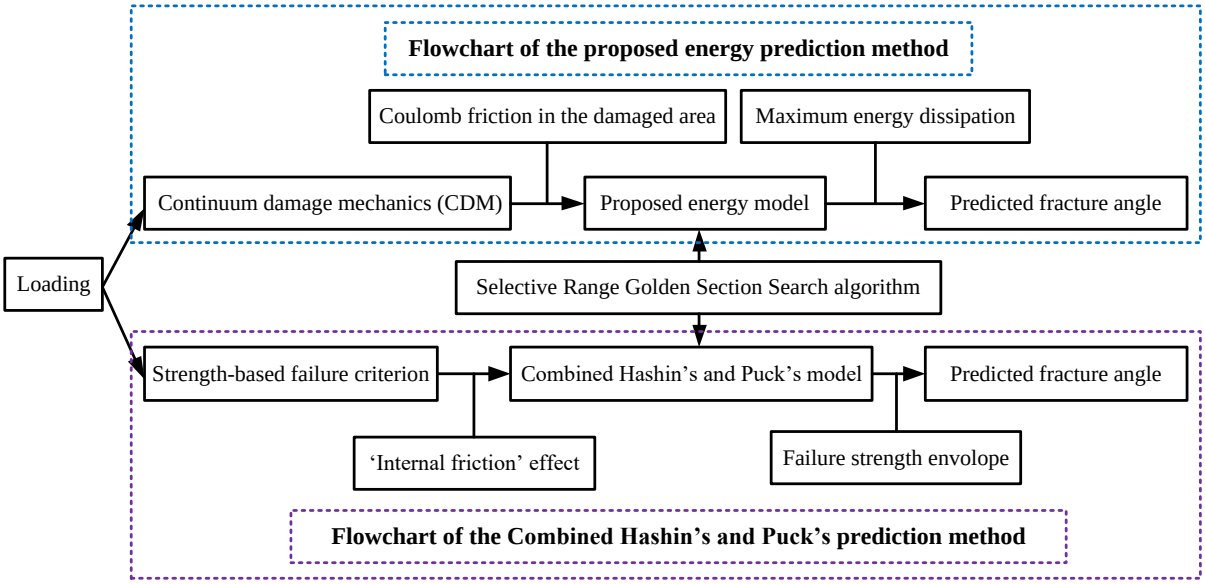

Figure 5.4 The comparison of two fracture angle prediction methods.

Table 5.2 lists the fracture angle prediction results under different stress states, including (1) pure tension, (2) pure shear, (3) pure compression, (4) arbitrary loading I, (5) arbitrary loading II, (6) arbitrary loading III, and (7) arbitrary loading IV. For the arbitrary loading states, the reference stress s_r is used to describe the ratios between the stresses. The predicted fracture angles using the combined failure criteria and the proposed energy-based method under different loading states are listed in Table 2. The comparison shows that the predicted results from the energy-based method agree with the predictions from the combined matrix failure criteria. The predicted results between the two methods are closer for the loading states (2)–(5), while a larger error ($-7°$) is observed for the pure tension case (1). The equations for obtaining the fracture angle for the tension case are in the same form based on the two methods in Eqs. (5.11) and (5.18). The difference in the predictions is because moduli values of the material are used in the proposed energy-based method rather than the strengths.

Table 5.2 Loading states and comparison of fracture angle prediction.

Loading State	Stress Status						Predicted Fracture Angle		
	σ_{11}	σ_{22}	σ_{33}	τ_{12}	τ_{23}	τ_{13}	Combined Hashin's and Puck's model	Proposed energy-based method	Error
1. Pure tension	0.0	≥ 0.0	0.0	0.0	0.0	0.0	$35°$	$28°$	$-7°$
2. Pure shear	0.0	0.0	0.0	$\neq 0.0$	0.0	0.0	$0°$	$0°$	$0°$
3. Pure compression	0.0	< 0.0	0.0	0.0	0.0	0.0	$53°$	$52.4°$	$-0.6°$
4. Arbitrary state I	0.0	$-1.0s_r$	$4.0s_r$	$2.3s_r$	$3.0s_r$	$-1.5s_r$	$65.1°$	$64°$	$-1.1°$
5. Arbitrary state II	0.0	$1.0s_r$	$2.0s_r$	$1.8s_r$	$1.0s_r$	$-2.5s_r$	$-10°$	$-11°$	$-1°$
6. Arbitrary state III	0.0	$-1.0s_r$	$-4.0s_r$	$2.3s_r$	$3.0s_r$	$-1.5s_r$	$25.5°$	$28.6°$	$3.1°$
7. Arbitrary state IV	0.0	$-3.0s_r$	$-8.0s_r$	$0.3s_r$	$1.7s_r$	$-0.5s_r$	$33.8°$	$33.4°$	$-0.4°$

Note: s_r is the positive reference value that results in constant stress ratios.

Fig. 5.5 shows the variation in the fracture indicator (p) in the combined matrix failure criteria and the energy dissipation rate (Y) in the proposed energy-based method with respect to the potential fracture angle in the range of $[-90°, 90°]$ under the five stress states. For comparison purposes, the coefficient of energy dissipation rate (Y) in the proposed model is normalized in the range of $[0, 1]$ in this work. Similar trends are observed in the predicted results of these two models. When Y is positive, the free energy density in the damaged area depends on the compression stress because of the friction on the fracture surfaces. The predicted value for state (3) (pure compression) is zero with the proposed method when θ_p is in the range of $[-23°, 23°]$. Also, this phenomenon occurs for the state (7) (arbitrary state IV) in the ranges of $[-90°, -67°]$, $[-21°, 8°]$, $[-59°, 79°]$ and $[-89°, 90°]$. It means that the free energy density does not change when the damage grows inside the matrix. This is because the increment of free energy density in the damaged area equals the free energy density dissipation in the undamaged area. Under this condition, the friction on the fracture surfaces is sufficiently large to resist their relative movement in the damaged area, as

shown in Fig. 5.3(d). Therefore, the material deforms as an undamaged material (see Eq. (5.14)) even after the damage is initiated, and it is not physically feasible for these angles to form the fracture plane from the perspective of energy dissipation. This demonstrates that the proposed method provides a physical explanation for determining the fracture angle based on the energy approach.

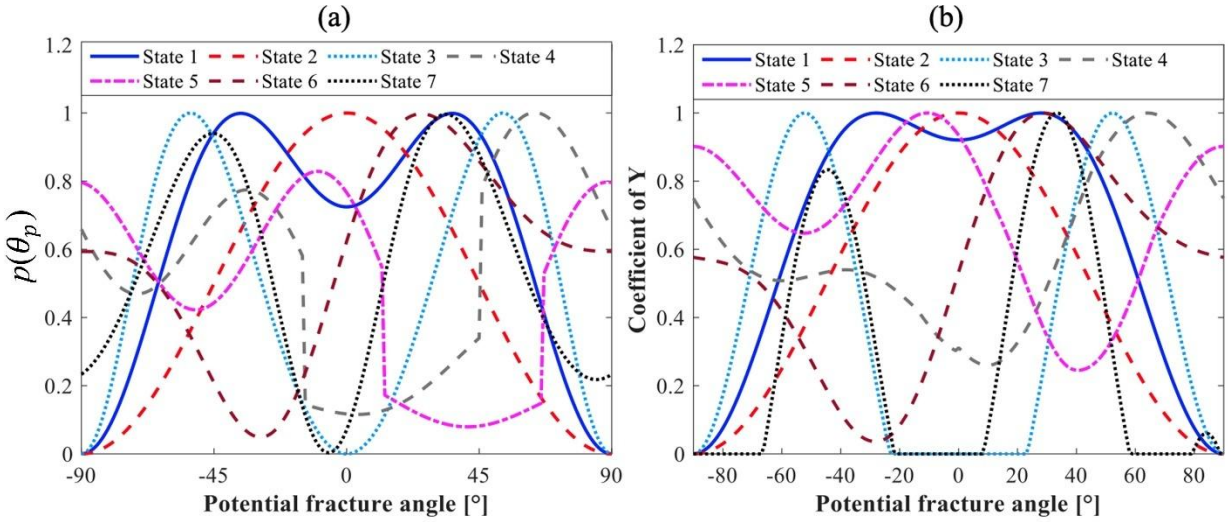

Figure 5.5 (a) $p(\theta)$ with potential fracture angle based on the combined failure criteria and (b) coefficient of energy dissipation rate (Y) based on the proposed energy method.

To achieve a fast and reliable prediction, the precision of 1° is requested in calculating the fracture angle using SRGSS. The computational costs for the two methods are compared in terms of the number of supporting points as given in Table. 5.3. It is shown that the proposed method shares almost the same computational cost with the combined failure criteria method owing to similar prediction trends (see Fig. 5.5). For the arbitrary state IV, values of 6 more points need to be calculated for the proposed method because there exists one more local maximum point as shown in Fig 5.5.

Table 5.3 Number of iterations and variation of predicted fracture angles.

Loading States	Number of supporting points		Variation of predicted fracture angle	
	Combined Hashin's and Puck's model	Proposed energy-based method	Combined Hashin's and Puck's model	Proposed energy-based method
1	30	30	0°	0°
2	24	24	0°	0°
3	30	30	8.0°	0°
4	30	30	0°	0°
5	30	30	0°	0°
6	24	24	$-10.3°$	0°
7	30	36	$-8.6°$	0°

Fig. 5.6 illustrates the iteration of the supporting points for two methods using SRGSS during the pure compression and arbitrary loading processes. It is shown that the number of supporting points does not change with the loading stress for two prediction methods. Besides, the fracture angle predicted by the combined failure criteria method changes from $46.2°$ to $53.0°$ and $35.8°$ to $25.5°$ during the loading process, while it remains constant for the proposed energy method. In addition, the proposed energy method processes high-order derivatives and achieves smoother prediction curves (see Eq. (5.9) and Fig. (5.5b)). It makes the proposed method have the advantage of using algorithms of higher convergence order such as Newton's method.

Moreover, in the combined matrix failure criteria in the literature, the calibration of the terms e_{nl} and e_{nt} is sensitive to the fracture angle measurement. When the measured θ_e ranges from $50°$ to $55°$, the calibrated e_{nt} increases from 0.176 to 0.364. This results in uncertainty in the calibration, considering the measurement error of the fracture angle in the experiment. However, in the proposed energy-based matrix failure criterion, these two frictional stress-related terms (e_{nl} and e_{nt}) are not involved. Instead, the actual in-plane and out-of-plane Coulomb friction coefficients identified from the friction tests [77] are directly used to model the friction on the fractured surfaces. As a result, the calibration procedure from the fracture angle measurement can be avoided using the proposed energy-based method.

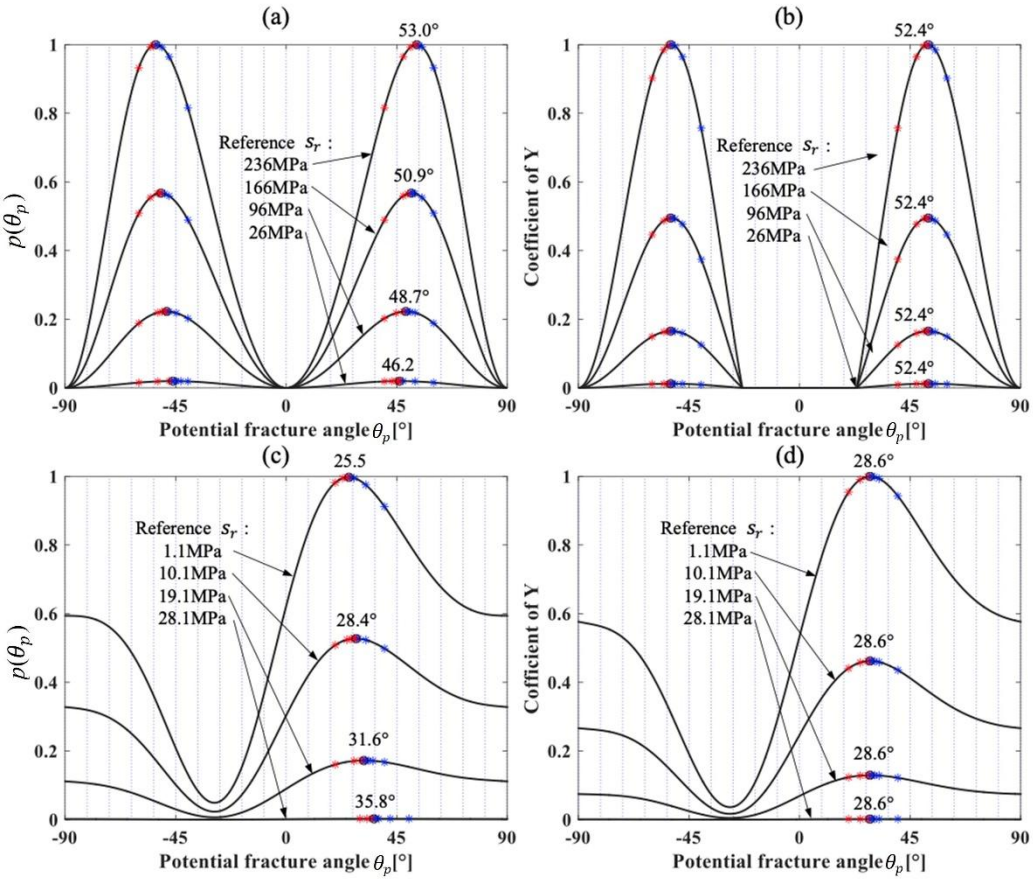

Figure 5.6 Fracture angle predictions and their variations during loading process based on SRGSS. (a) and (b): Pure compression, (c) and (d): arbitrary loading III.

5.5. Conclusion

A new energy-based approach for predicting the fracture angle of CFRP under three-dimensional mechanical loading is presented. The effect of frictional stress on the fractured surfaces under compressive normal stress is considered in modeling the complementary free energy density during the failure process. The fracture angle is determined according to the direction of the maximum energy dissipation rate. The accuracy of the fracture angle prediction is validated in comparison with the strength-based Hashin's tensile failure criterion and Puck's compressive failure criterion using SRGSS. The proposed energy-based model demonstrates that the friction at the fractured surfaces plays an important role in the fracture plane orientation, which is quantitatively determined under different stress states. The model provides the physical basis of the damage propagation and fractured plane formation from an energy perspective, and there is no need to identify the friction-related term from the fracture angle measurement.

6. Material Removal Mechanism in Machining UD CFRP Based on Frictional-damage Mechanics

In Chapter 5, the stress in the shear direction of the fracture plane is divided into the elastic shear stress component in the undamaged area, and the Coulomb friction component on the formed cracked surfaces in the damaged area. Therefore, the energy stored in the material is influenced by these two components during the failure process, and the friction on the cracked surfaces in the damaged area increases the ultimate strength and determines fracture propagation direction [82]. In this chapter, a new failure criterion for CFRP failure is developed to evaluate the direction of the fracture on the chip formation plane and the corresponding failure mode. The fracture area of uncut material is treated as an interface bonding layer with direction to be determined. The elastic stress and Coulomb friction on the chip formation plane are predicted, which provides a physical explanation for the enhancement effect of the defined 'internal friction'. The proposed method is validated with experimental measurements of the orthogonal cutting at various uncut chip thicknesses, including the chip formation modes, chip formation angle, and cutting forces in the fiber orientation range of $[0°, 180°]$.

6.1. Mechanics model for CFRP cutting

6.1.1. Cutting mechanics model

The schematic of the orthogonal cutting process at various fiber orientations is shown in Fig. 6.1. The uncut material located in front of the tool rake face moves towards the rake face in the cutting direction, and flows along the rake face once the fracture is initiated on the chip formation plane which resembles the shear plane in metal cutting. The material deformation in the pressing region flows along the contour of the flank face and is not relevant to the chip formation. This chapter focuses on the chip formation region, so the material deformation and force generation in the pressing region is not discussed.

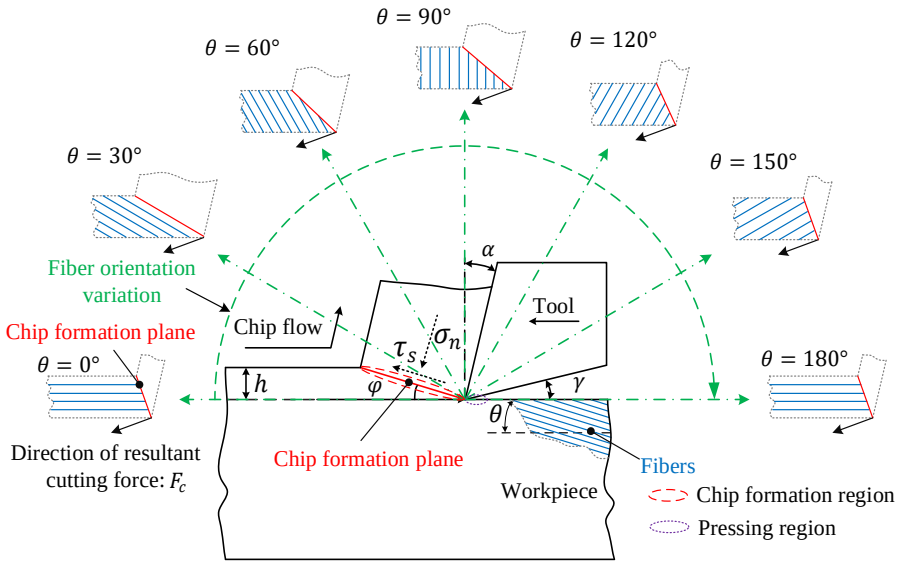

Figure 6.1 Schematic representation of chip formation process at various fiber orientations.

Considering that the chip formation angle varies with fiber orientation, there may exist two potential relationships between the chip formation angle and fiber orientation: (i) chip formation angle $>$ fiber orientation, (ii) chip formation angle $\leq$ fiber orientation. The schematic representation of the chip formation for an arbitrary fiber orientation in the entire range of $[0°, 180°]$ with undetermined chip formation mode, chip formation angle, and cutting forces (or chip formation mechanism) is shown in Fig. 6.2(a). The following assumptions, which are used in the related work in the literature [38, 40], are applied in developing the mechanics model:

(1) The chips are formed owing to the quasi-continuous failure of uncut material.

(2) The chip formation region is treated as a flat plane with infinitely small thickness.

(3) This model mainly focuses on the effect of fiber orientation on the cutting mechanics, therefore, the effects of strain rate (or cutting speed), temperature, and moisture on the CFRP mechanical property are neglected.

(4) The friction coefficient between the formed chip and rake face is assumed to be a constant in the fiber orientation range of $[0°, 180°]$.

To determine the unknown stresses (σ_n, τ_s) on the chip formation plane and chip formation angle (φ) under a given fiber orientation (θ), the stress transformation is performed from the chip formation plane to the ply coordinate $(X_1 - X_2)$, as shown in Fig. 6.2(b):

$$\begin{aligned}\sigma_{22} &= \sigma_n \cos^2(\varphi-\theta) + 2\tau_s \sin(\varphi-\theta)\cos(\varphi-\theta)\\ \sigma_{11} &= \sigma_n \sin^2(\varphi-\theta) - 2\tau_s \sin(\varphi-\theta)\cos(\varphi-\theta)\\ \tau_{12} &= -\sigma_n \sin(\varphi-\theta)\cos(\varphi-\theta) + \tau_s[\cos^2(\varphi-\theta) - \sin^2(\varphi-\theta)]\end{aligned} \quad (6.1)$$

According to the relationship between the shear stress (τ_s) and normal stress (σ_n), Eq. (6.1) can be re-organized as:

$$\begin{aligned}\sigma_{22} &= \tau_s[2sin(\varphi-\theta)cos(\varphi-\theta) - Tcos^2(\varphi-\theta)]\\ \sigma_{11} &= \tau_s[-2sin(\varphi-\theta)cos(\varphi-\theta) - Tsin^2(\varphi-\theta)]\\ \tau_{12} &= \tau_s[cos^2(\varphi-\theta) - sin^2(\varphi-\theta) + Tsin(\varphi-\theta)cos(\varphi-\theta)]\end{aligned} \quad (6.2)$$

where T is determined by the cutting mechanics related to parameters and chip formation angle:

$$T = \tan(\varphi + \beta - \alpha) \quad (6.3)$$

β is the friction angle between the formed chips and rake face, α is the tool rake angle.

Therefore, under a given fiber orientation, the stresses $(\sigma_{11}, \sigma_{22}, \tau_{12})$ in the ply coordinate $(X_1 - X_2)$ are only related to the undetermined shear stress (τ_s) on the chip formation plane and chip formation angle (φ). By substituting the stresses $(\sigma_{11}, \sigma_{22}, \tau_{12})$ into the failure criterion, the quantitative relationship between the shear stress on the chip formation plane and chip formation angle can be obtained, which will be discussed in the next section.

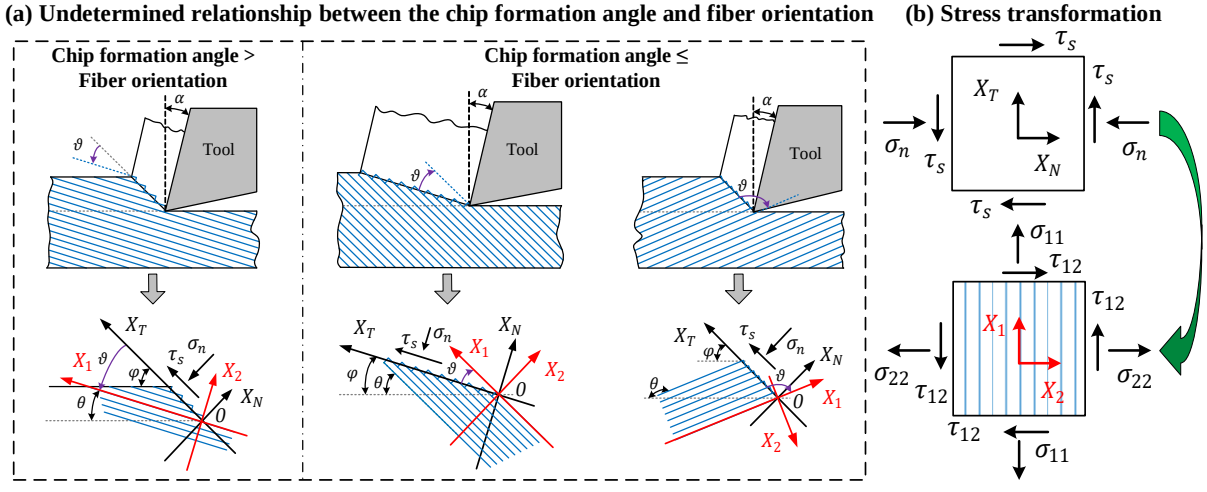

Figure 6.2 Undetermined relationship between the chip formation angle and fiber orientation, and stress transformation.

6.1.2. Frictional-damage based CFRP failure criterion

Various strength-based failure criteria which divide the failure process into four modes: fiber tension, fiber compression, matrix tension, and matrix compression have been proposed to capture the chip formation behaviour of the UD CFRP failure process using stresses ($\sigma_{11}, \sigma_{22}, \tau_{12}$) in the ply coordinate. Considering that it has been proved that the damage propagation has a significant effect on the failure of UD CFRP [82], this chapter proposes a new failure criterion using damage mechanics, which focuses on the formation of the fracture in the uncut material. In addition, the widely used strength-based criteria, including Hashin-Rotem failure criterion [56] and combined Hashin-Puck failure criterion [76] which introduces the 'internal friction' concept under matrix compression are used in comparison with the proposed failure criterion for the cutting process modeling. Fig. 6.3 illustrates the two strength-based failure criteria that use fiber tension strength (X_{11}^t), fiber compression (micro-buckling) strength (X_{11}^c), matrix tension strength (X_{22}^t), matrix compression strength (X_{22}^c), in-plane shear strength (τ_{12}), and enhancement factor (e_{nl}) owing to the 'internal friction'.

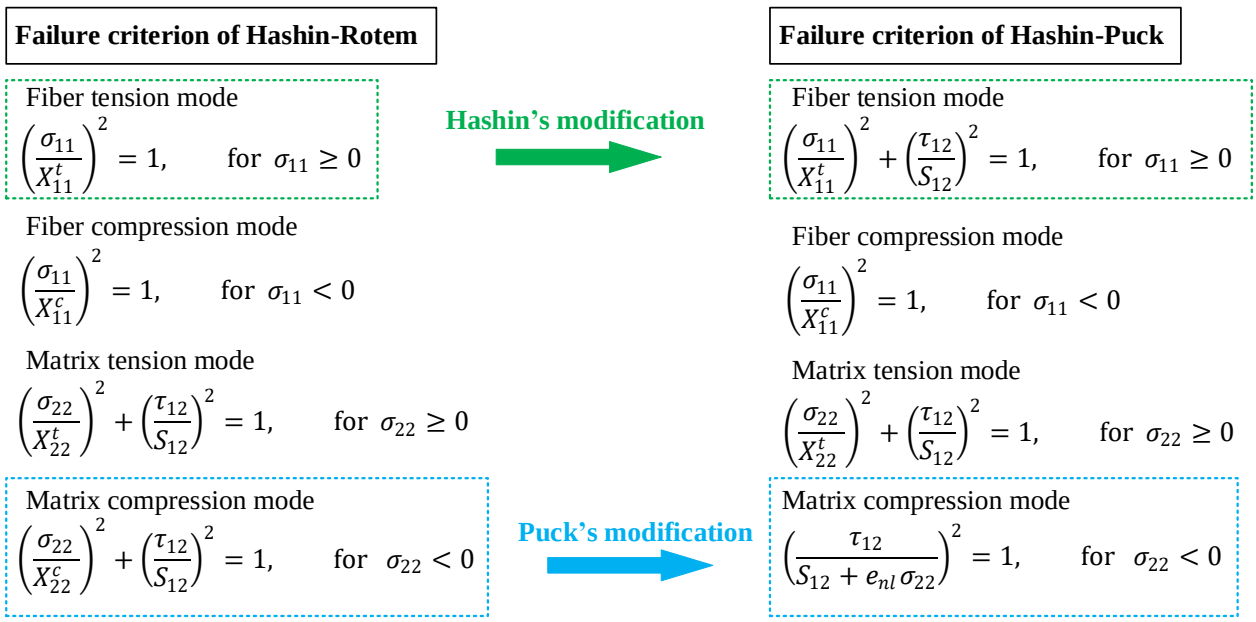

Figure 6.3 Strength-based failure criteria.

The modification by Hashin-Puck criterion under fiber tension mode [57] in Fig 6.3 considers the weakening effect of the shear stress on the tension failure in the fiber direction (X_1). For matrix compression mode, it was noticed by Hashin [57] that the expression for the matrix failure mode

based on Hshin-Rotem criterion is not able to predict the fracture angle under transverse compression which lies in the range of $[50°, 55°]$ instead of the maximum shear direction (45°). Therefore, Puck [48] modified the matrix failure criterion by introducing the 'internal friction' term and claimed that the normal compression increased the shear strength, even though the existence and the physical meaning for such an 'internal friction' in this nonhomogeneous UD CFRP material are questioned [83, 84].

According to the experimental observations, cracks are formed and distributed in the vicinity of the fracture direction inside the matrix and fiber-matrix interface owing to the significant difference between the moduli of fibers and matrix under external loading. These cracks are closed under compression and provide additional friction, and therefore propagate along the direction where the energy dissipation rate reaches the maximum [82]. Based on this understanding, a new failure criterion is proposed to evaluate the fracture and its propagation direction of the uncut material (or chip formation angle) using frictional-damage mechanics. The ultimate strengths before the complete failure of the CFRP material, instead of yield strengths, are used in this work because the resultant shear stress for matrix failure mode can still increase when the friction in the damaged area is large enough to compensate for the decrease of the stress in the undamaged area, as shown in Fig. 6.4.

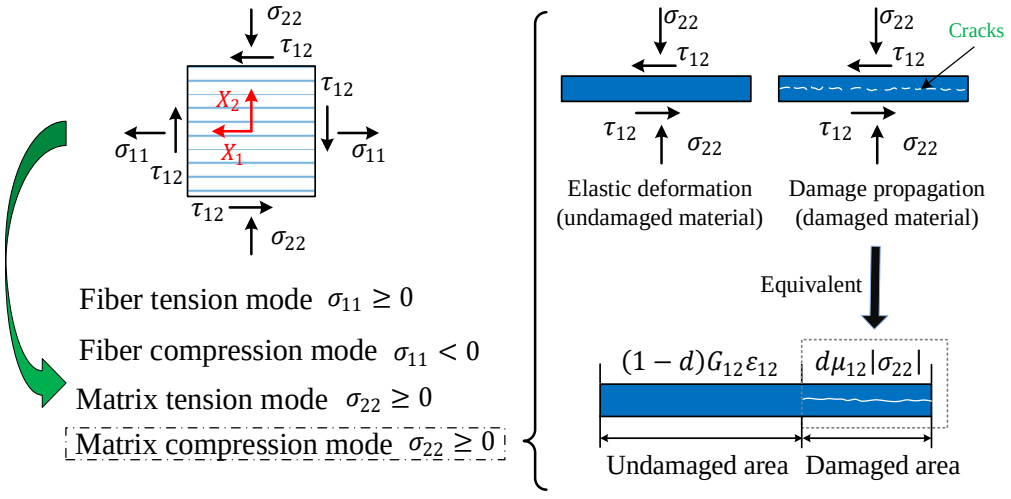

Figure 6.4 Four chip formation modes and frictional-damage behavior of the uncut material.

For the tension modes of matrix and fiber, the cracks open under the normal tension. In such cases, there is not friction existing on the cracked surfaces in the damaged area. Therefore, the CFRP material fails when the yield strengths are reached. For the fiber compression mode, the

damage process starts from the in-plane shear deformation in the matrix (rotation of the CFRP material in the kinking band) and ends up with material crushing of the kinking band. In this buckling process, the friction on the cracked surfaces does not play a role, because there is no transverse compression in the X_2 direction which can provide the normal compression for the in-plane shear. Therefore, the proposed failure criteria for these three failure modes follow the Hashin criterion [57]. The failure process for the matrix compression mode has been experimentally observed and investigated [71]. This process starts from the cracks owing to the shearing in the matrix, and the crack direction varies with the value of the compressive stress applied in the transverse (X_2) direction. By introducing the friction on the closed crack surfaces to the damaged area, the failure process in the fracture direction, which refers to the direction of the maximum free energy dissipation stored in the uncut material, is modeled [82]. Since the thermal and hygroscopic expansions are not considered in this study, the complementary free energy density for the deformed material during the failure process in the transformed coordinate ($X_1 - X_2$) is represented as:

$$\psi = \frac{\sigma_{11}^2}{2(1-d_1)E_1} + \frac{\sigma_{22}^2}{2[1-d_2 \cdot H(\sigma_{22})]E_2} - \frac{v_{12}}{E_1}\sigma_{11}\sigma_{22} + \frac{[\tau_{12} - d_2 t(\tau_{12})\mu_{12}\sigma_{22}H(-\sigma_{22})]\tau_{12}}{2(1-d_2)G_{12}} \tag{6.4}$$

where E_1 and E_2 are elastic moduli of the material in the longitudinal (X_1) and transverse (X_2) directions. G_{12} is the shear modulus. v_{12} is the Poisson's ratio of the material in the material coordinate. $H(\cdot)$ is the Heaviside step function used to distinguish the compression and tension conditions. μ_{12} is the coefficient of Coulomb friction in the longitudinal (X_1) direction because the friction only exists on the closed damaged surfaces in the matrix. The step function $t(\cdot)$ is used to determine the direction of the frictional stresses:

$$t(x) = \begin{cases} 1, & x < 0 \\ -1, & x \geq 0 \end{cases}. \tag{6.5}$$

d_1 and d_2 are defined as the damage variables for the fiber and matrix failure modes, respectively. The damage variables change from 0 at the initiation of the failure (or when the elastic strength is reached) to 1 at the complete failure. Meanwhile, the relevant stress component decreases linearly

from the strength to zero during the degradation of the material modulus. Therefore, the two damage variables (d_1, d_2) which follow the linear degradation law with respect to the relative displacement (ζ) are given as:

$$d_1 = \zeta_1^f \frac{\zeta_1 - \zeta_1^0}{\zeta_1(\zeta_1^f - \zeta_1^0)} \tag{6.6}$$

$$d_2 = \zeta_2^f \frac{\zeta_2 - \zeta_2^0}{\zeta_2(\zeta_2^f - \zeta_2^0)} \tag{6.7}$$

where two subscripts 1 and 2 refer to the longitudinal and transverse directions, respectively. ζ_1^0 and ζ_2^0 are the relative displacements when the elastic (or yield) strengths are achieved for fiber and matrix failure modes, respectively. The superscripts 0 and f represent the initiation of the failure and complete failure, respectively. For the matrix compression failure mode, the friction provided in the matrix (failure mode) is considered and the relative displacements are given as:

$$\zeta_2^0 = \frac{S_{12}}{G_{12}} \tag{6.8}$$

$$\zeta_2^f = \frac{2G_{II}}{S_{12}} \tag{6.9}$$

where the S_{12} is the elastic (or yield) shear strength. G_{II} is the mode II fracture energy under compression (σ_{22}) defined as:

$$G_{II} = (1 - \omega_{12}\sigma_{22})G_{II}^0 \tag{6.10}$$

where G_{II}^0 is the mode II fracture energy without compression, and $\omega_{12}(= 0.0245\ \text{MPa}^{-1})$ [85] is the factor which describes the increase of the fracture energy under the compression (σ_{22}). The dissipation rate of the complementary free energy density, which defines the fracture direction during the failure process, is given as:

(1) Fiber failure mode

$$Y_1 = \frac{\partial \psi}{\partial d_1} = \frac{1}{2(1-d_1)^2}\frac{\sigma_{11}^2}{E_1} \tag{6.11}$$

(2) Matrix failure mode

$$Y_2 = \frac{\partial \psi}{\partial d_2} = \frac{1}{2(1-d_2)^2}(\frac{\sigma_{22}^2}{E_2} + \frac{\tau_{12}^2}{G_{12}}) \tag{6.12}$$

Then, the fracture propagation direction for the fiber and matrix failure modes can be determined by searching for the stress state ($\sigma_{11}, \sigma_{22}, \tau_{12}$) which achieves the maximum value of dissipation rate. For the fiber failure modes, the fracture plane of the uncut material is normal to the fiber direction (X_1) in which the normal stress (σ_{11}) is the maximum. However, for the matrix failure modes, the fracture plane of the uncut material is determined by both the shear stress (τ_{12}) and normal stress (σ_{22}). Once the yield strength is achieved ($d_1, d_2 = 0$), the modulus of the material in the fracture direction starts to degrade until the complete failure ($d_1, d_2 = 1$). During this process, the resultant stress in the fracture propagation direction is composed of the decreased elastic stress in the undamaged area and the increased friction in the damaged area when the cracks are closed under compression ($\sigma_{22} < 0$). Therefore, the resultant shear stress can keep increasing to the ultimate shear strength after the elastic shear strength is reached owing to the increase of friction at the closed cracked surfaces, as shown in Fig. 6.4.

Considering the undamaged and damaged areas, the resultant shear stress for the matrix compression failure is expressed as:

$$S_{12}^d(d_2) = (1-d_2)G_{12}\varepsilon_{12} + d_2\mu_{12}\sigma_{22} \tag{6.13}$$

where $\mu_{12}\sigma_{22}$ is the friction under compression. Here, the resultant shear stress (S_{12}^d) in the matrix is equal to the shear strength (S_{12}) at the initiation of the failure ($d_2 = 0$) and is equal to the pure friction ($d_2\tau_d$) at the complete failure. The ultimate failure strength for the matrix compression failure is given as the maximum value of the equation, represented as:

$$S_{12}^m = \max(S_{12}^d(d_2)), \qquad (0 \le d_2 \le 1) \tag{6.14}$$

Considering that the ultimate strengths for the fiber tension, fiber compression, and matrix tension modes are equal to the yield strengths because there is no additional friction in the damaged area, the proposed failure criterion is given as:

(i) Fiber failure modes

Fiber tension ($\sigma_{11} \geq 0$) and compression ($\sigma_{11} < 0$) failure.

$$\begin{aligned} &\left(\frac{\sigma_{11}}{X_{11}^{t}}\right)^{2} + \left(\frac{\tau_{12}}{S_{12}}\right)^{2} = 1, && \text{for } \sigma_{11} \geq 0 \\ &\left(\frac{\sigma_{11}}{X_{11}^{c}}\right)^{2} = 1, && \text{for } \sigma_{11} < 0 \end{aligned} \tag{6.15}$$

(ii) Matrix failure modes

Matrix tension ($\sigma_{22} \geq 0$) and compression ($\sigma_{22} < 0$) failure.

$$\begin{aligned} &\left(\frac{\sigma_{22}}{X_{22}^{t}}\right)^{2} + \left(\frac{\tau_{12}}{S_{12}}\right)^{2} = 1, && \text{for } \sigma_{22} \geq 0 \\ &\left(\frac{\tau_{12}}{S_{12}^{m}}\right)^{2} = 1, && \text{for } \sigma_{22} < 0 \end{aligned} \tag{6.16}$$

By replacing the stresses σ_{22}, σ_{11}, and τ_{12} in Eqs. (4.10) and (4.11) with Eq. (6.2), the relationship between the shear stress (τ_s) and chip formation angle (φ) at an arbitrary fiber orientation in the entire range of $[0°, 180°]$ is determined using the proposed failure criterion for relevant failure modes. The shear stress (τ_s) on the chip formation plane and corresponding failure mode are determined using the minimum energy principle as shown in Fig. 4.4. The flowchart which shows the detailed procedure of predicting the chip formation mechanism and cutting forces by the proposed model is presented in Fig. 6.5.

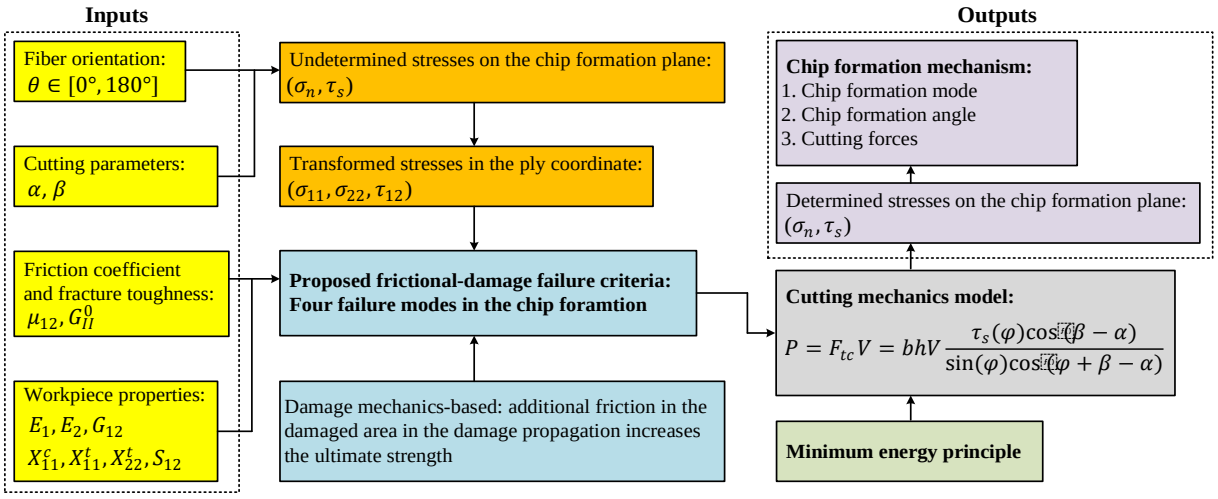

Figure 6.5 Flowchart of the proposed cutting mechanics model.

6.2. Chip formation mechanism analyses and experimental validation

6.2.1. Experimental setup

The orthogonal cutting experiments are conducted on a milling machine (Fadal VMC 2216) with the angular movement of the spindle locked as shown in Fig. 4.5. The uncoated cutting tool is used to cut the CFRP workpiece whose fiber orientation is in the range of $[0°, 180°]$ with a constant cutting speed $V = 5$ m/min. The cutting parameters and mechanical properties of the UD CFRP workpiece are given in Table. 6.1 and Table 4.1. A dynamometer (Kistler 9257B) was mounted under the workpiece to measure the cutting forces in the tangential and thrust directions. The chip formation angle is measured using a 3D confocal microscope (Olympus LEXT OLS3100). In addition, to validate the effect of the friction on the chip formation mechanism, the predictions of Hashin-Rotem criterion which does not consider the friction on the cracked surfaces in the damaged area, and Hashin-Puck criterion that introduces the concept of 'internal friction' are included in the following analyses. The analyses include the chip formation angle (fracture angle of uncut material), cutting forces, and the prediction of the chip formation modes.

Table 6.1 Cutting parameters and workpiece properties.

Cutting parameters		
Fiber orientations	θ	$[0°, 180°]$ with interval of $30°$
Width of cut	b	4.4 mm
Uncut chip thickness	h	0.03 mm to 0.18 mm with interval of 0.03 mm
Rake angle/ Friction angle	α/β	$7°/25°$
Mechanical properties (Mitsubishi Chemical Carbon Fiber and Composite 304-1**)**		
Elastic and shear moduli		
Elastic modulus in longitudinal (X_1) direction	E_{11}	131 GPa
Elastic modulus in transverse (X_2) direction	E_{22}	8.9 GPa
Shear modulus	G_{12}	6.0 GPa
Yield strengths (provided by manufacturer)		
Shear strength of matrix failure	S_{12}	97 MPa
Tensile strength of matrix failure	X_{22}^t	83 MPa
Tensile strength of fiber failure	X_{11}^t	2903 MPa
Compressive strength of fiber failure	X_{11}^c	1675 MPa
Internal friction coefficient	μ_{12}	-0.3566 [87]
Fracture energy	G_{II}^0	1.0 N/mm [86]

6.2.2. Validations of failure criterion using chip formation angle and cutting forces

Fig. 6.7 shows the chip formation angles predicted at various fiber orientations in the range of $[0°, 180°]$ using the proposed failure criterion, Hashin-Rotem failure criterion, and Hashin-Puck failure criteria with experimental measurements. According to Fig. 6.7, all three failure criteria are able to capture the variation trend of the chip formation angle when the fiber orientation increases from $0°$ to $180°$. *V*-shape variations in the middle fiber orientation range. A close agreement is observed for the predictions by Hashin-Puck failure criterion and the proposed failure criterion, which can capture the sudden decrease of the chip formation angles at $70°$ and $150°$ fiber orientations, and the increase of the cutting forces at $70°$ fiber orientation as shown in Fig. 6.8. For the fiber orientations of $0°$ and $15°$, however, Hashin-Rotem failure criterion achieves a higher accuracy for both the chip formation angle and cutting force. Because the cutting forces and chip formation plane are determined by the stress state on the chip formation plane and relevant failure criteria, the chip formation modes predicted using the proposed failure criteria are discussed in the next section.

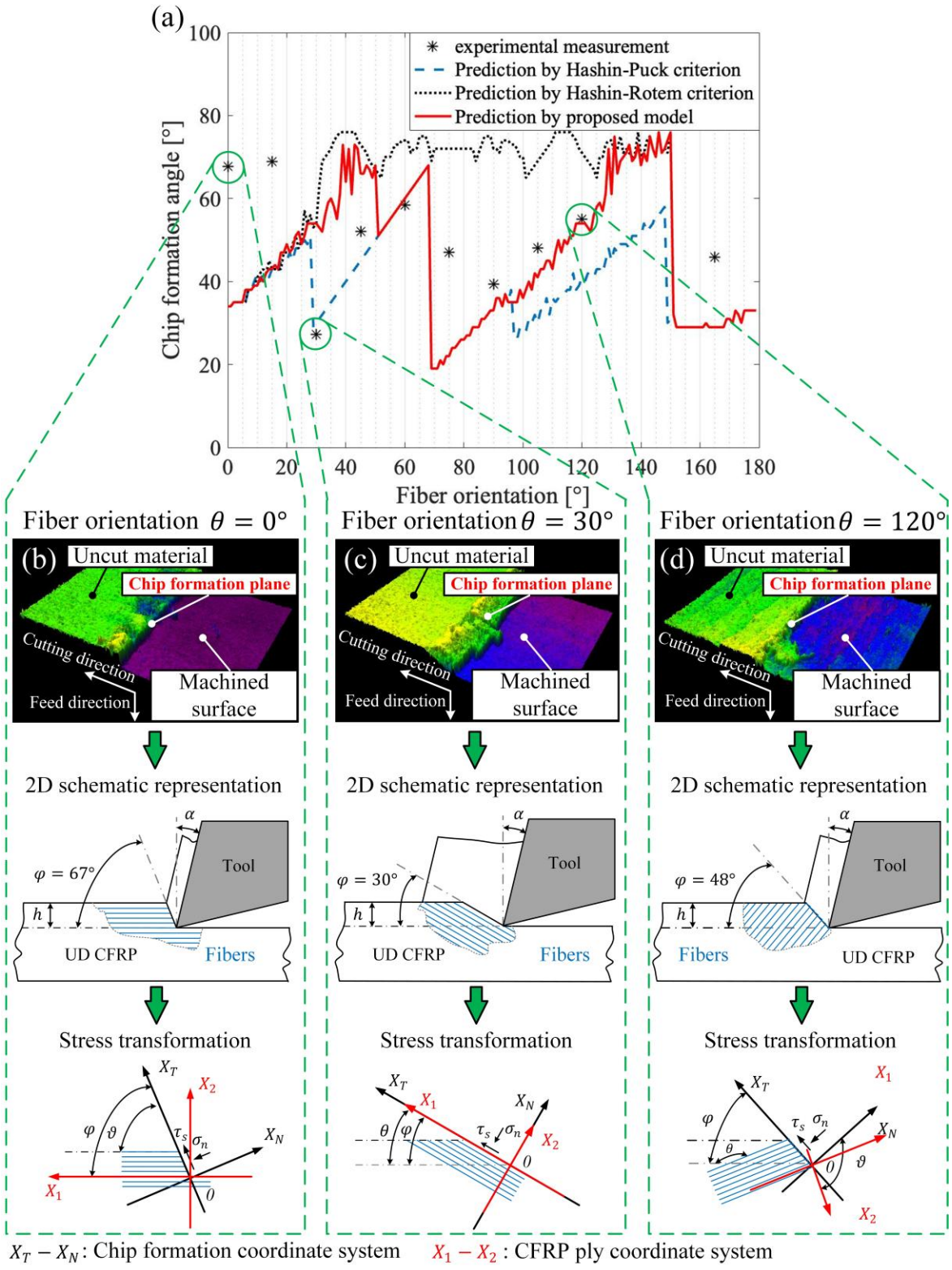

Figure 6.6 Chip formation angle measurements and schematic representation.

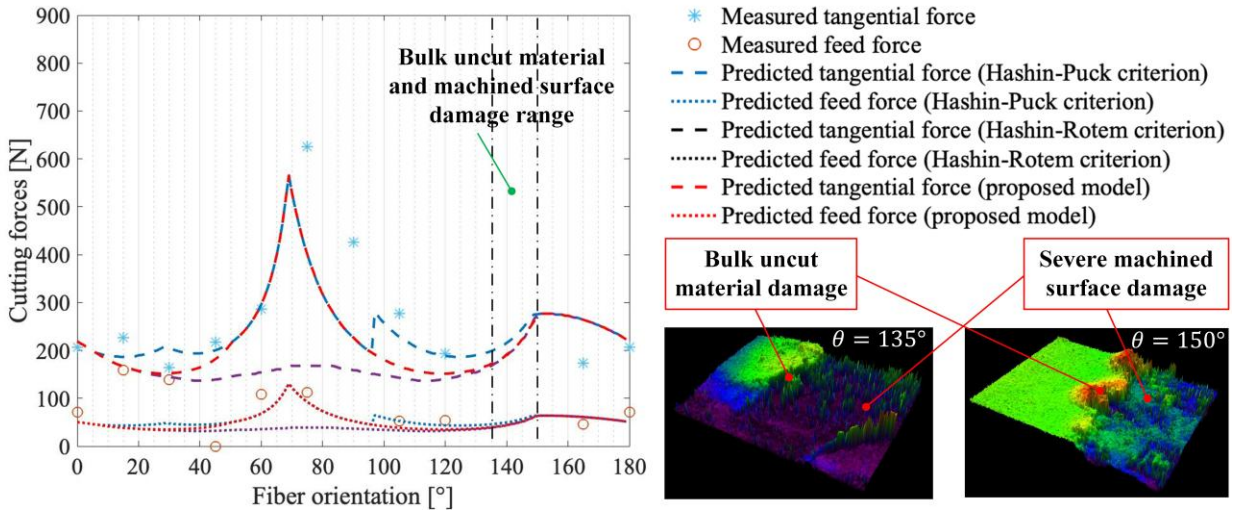

Figure 6.7 Cutting force measurements and predictions of proposed criterion, Hashin-Rotem criterion, and Hashin-Puck criterion.

6.2.3. Prediction of the chip formation mechanism

The variations of the predicted chip formation mode with respect to the potential chip formation angle and fiber orientation are shown in Fig. 6.9. The black lines represent the condition when the chip formation angle is equal to the fiber orientation. The red, blue, and grey curves are the predicted chip formation angles in the entire fiber orientation range when the proposed failure criteria, Hashin-Rotem, and Hashin-Puck failure criteria are applied, respectively. For the Hashin-Rotem failure criterion, the matrix compression dominates the chip formation process in the fiber orientation range of $[7°, 150°]$, while the matrix tension only occurs in the fiber orientation ranges of $[0°, 7°]$ and $[150°, 180°]$. This suggests that the chips are formed owing to the compressive stress ($\sigma_{22} < 0$) in the transverse direction and shear stress (τ_{12}) for the fiber orientation range of $[7°, 170°]$ (matrix compression mode), and tensile stress ($\sigma_{22} \geq 0$) in the transverse direction and shear stress (τ_{12}) for fiber orientation ranges of $[0°, 7°]$ and $[150°, 180°]$.(matrix tension mode). The two fiber failure modes do not play a role in forming the chips in the entire fiber orientation range, because it is easier to activate matrix failure modes when the enhancement effect of the normal compression is not considered. However, this enhancement effect dominates the chip formation in the fiber orientation of $[30°, 97°]$, because the increased shear strength under compression blocks the occurrence of the matrix compression failure mode and makes it easier to result in the fiber tension failure as shown in Fig. 6.9(a) and (c) which are predicted using the

proposed failure criterion and Hashin-Puck failure criterion, respectively. In other words, the ultimate strength owing to the friction in the damaged area requires more energy to be activated compared to the fiber tension mode. It is also noted that the three failure criteria achieve the same chip formation mode prediction in the fiber orientation ranges of $[30°, 90°]$, because the normal compression in the rest fiber orientation ranges is not large enough to block the occurrence of matrix compression mode.

Regardless of the similarity for predicted chip formation modes using the proposed failure criterion and Hashin-Puck failure criterion, the proposed failure criterion considers the friction in the damaged area using frictional-damage mechanics without introducing the 'internal friction'. Besides, because the friction is linearly proportional to the compressive stress (σ_{22}) according to the proposed failure criterion, the ultimate strength increases with the compressive stress which provides a physical explanation of the 'enhancement effect' of the compressive stress on the failure strength. To quantitatively analyze the effect of the friction in the damaged area on the chip formation, the damage variables (d_1, d_2) for the matrix failure and fiber failure modes are given in Fig. 6.9(d). The damage variable for matrix failure (d_2) reaches unity in the fiber orientation range of $[37°, 105°]$, which shows that the matrix fails before the tension failure. However, the friction in the completely damaged material can still influence the chip formation mode. For the cutting force and chip formation angle predictions in the fiber orientation ranges of $[30°, 150°]$, it is noted that Hashin-Rotem failure criteria achieve the lower accuracy for the chip formation angle and cutting forces, which suggests the necessarity of considering the enhancement effect of friction during damage propagation.

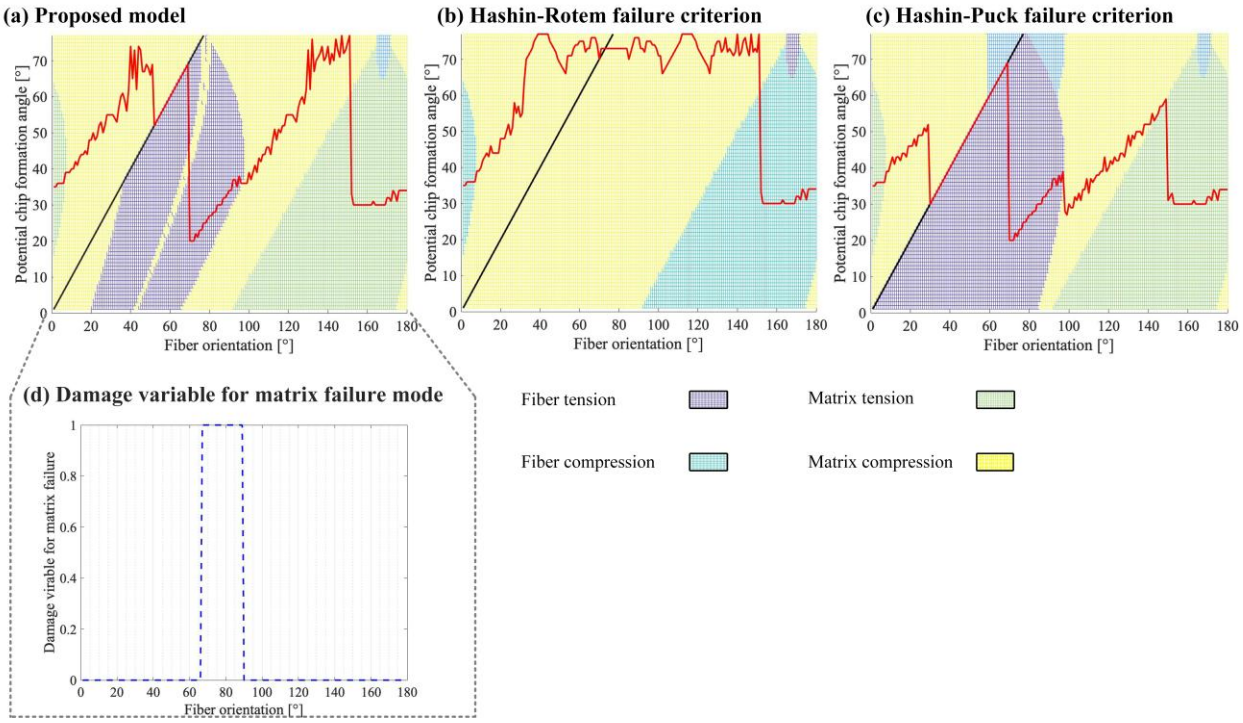

Figure 6.8 Chip formation mode predictions of proposed criterion, Hashin-Rotem criterion, and Hashin-Puck criterion.

6.3. Conclusion

This chapter presents a frictional-damage mechanics model to investigate the chip formation mechanism in the UD CFRP cutting process using the minimum energy principle. The friction in the damaged area during the failure process is considered and proved to play an important role in determining the chip formation mode, chip formation angle, and cutting forces, which are not included in the Hashin-Rotem failure criterion and treated as 'internal friction' in Hashin-Puck failure criterion. This work is validated by the agreement between the cutting mechanics mode using the proposed failure criterion and the experimental measurements. The conclusions from this study are listed below:

(1) The friction in the damaged area increases the ultimate strength of the matrix compressive failure mode, which affects the chip formation and the variation of the chip formation angle in the fiber orientation of $[65°, 90°]$.

(2) The complete failed matrix material can still affect the chip formation mode due to friction when the chip formation angle equals fiber orientation.

(3) The source of the ‘enhancement effect’ of the compressive stress on the ultimate shear strength in the machining process is explained using the Coulomb friction at the damaged interface instead of ‘internal friction’ concept.

7. Orthogonal Cutting Mechanics of Multi-directional CFRP With Interlaminar Bonding

This chapter focuses on the unique chip formation mechanism in orthogonal cutting of MD CFRP in comparison with UD CFRP. Fig. 7.1 shows the flow chart of the work in this chapter. The chip formation plane is experimentally examined, which shows that the chip formation angles of different plies converge to a constant angle. An analytical mechanics model of cutting MD CFRP is developed to predict the chip formation angle, fiber-matrix failure mechanism, and cutting forces with experimental validation.

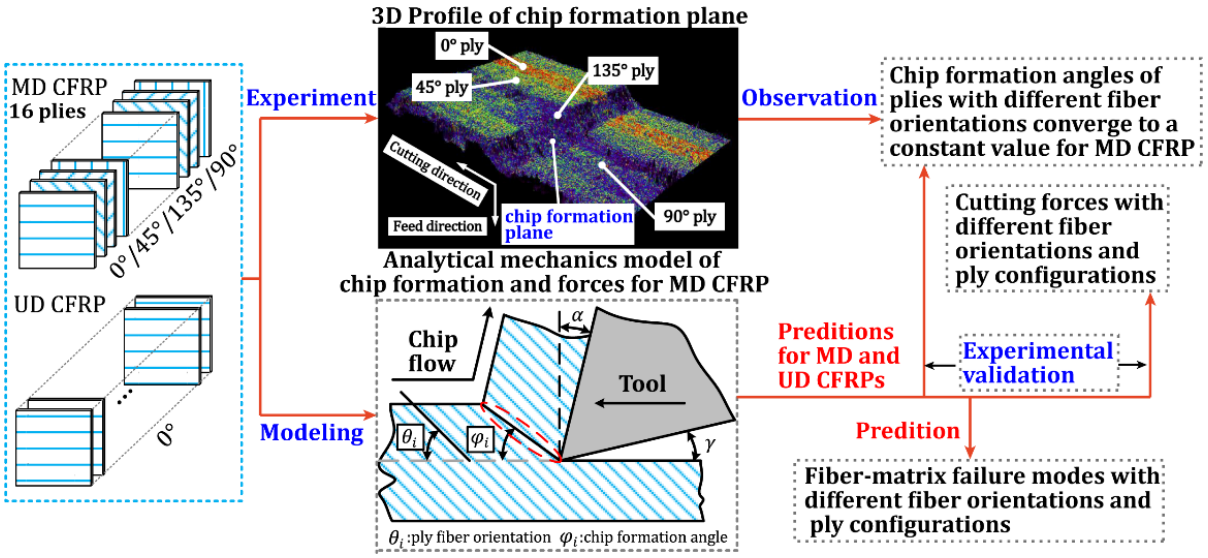

Figure 7.1 Flow chart of the work in this chapter.

7.1. Experimental procedure and results

Orthogonal cutting experiments are conducted for MD CFRP with the ply stacking sequence of $[0°/45°/135°/90°/90°/135°/45°/0°]_2$ and UD CFRP with the ply stacking sequence of $[0°]_{16}$. The experiments are performed on the Fadal VMC 2216A machine tool. The CFRP workpiece is clamped by a vise, and a dynamometer (Kistler 9257B) is mounted under the vise to measure the average tangential and feed forces from the time-domain data. The angular motion of the cutting tool is locked to orient the tool edge in the cutting direction for orthogonal cutting configuration. Three MD CFRP laminates with the first ply at 0°, 15°, and 30° fiber orientations are used. Correspondingly, the ply orientation sequences for the CFRP laminates are $[0°/45°/135°/90°/90°/135°/45°/0°]_2$, $[15°/60°/150°/105°/105°/150°/60°/15°]_2$, and

$[30°/75°/165°/120°/120°/165°/75°/30°]_2$, respectively. To analyze the effect of the interlaminar bonding, the fiber orientations for the UD CFRP workpieces are selected with an angle interval of $15°$ in the entire fiber orientation range of $[0°, 180°]$. The cutting parameters and the mechanical properties of the CFRP workpiece are given in Table 7.1. As this chapter focuses on the effects of fiber orientation and interlaminar bonding on the cutting mechanics of MD CFRP, and the effects of strain rate and temperature on CFRP mechanical properties are not considered, a constant cutting speed of 5 m/min is used in all experiments. The tool was stopped by the machine feed drive with 1 g deceleration at a deceleration period of 8.5 ms. The tool then retracts, and a laser scanning confocal microscope (Olympus LEXT OLS3100) was used to obtain the topography of the chip formation plane which connects the uncut and machined surfaces after each cutting experiment. The chip formation plane corresponds to the material fracture plane shown as 'AB' in the orthogonal cutting configuration of Fig. 7.1, and the chip formation angle is defined by the angle between the chip formation plane and the cutting velocity direction.

Table 7.1 Cutting parameters and ply mechanical properties.

Cutting parameters		
Workpiece types	MD CFRP	UD CFRP
Fiber orientations	0°,15°,30° (Represented by fiber orientation of the first ply)	0°,15°,30°,45°,60°, 75°,90°,105°,120°, 135°,150°,165°
Uncut chip thickness (h)	$0.03, 0.06, 0.09, 0.12, 0.15, 0.18$ mm	
Cutting speed (V)	5 m/min	
Rake/ Friction angle (α/β_f)	$7°/20°$	
Ply thickness	300 μm	
Number of plies	16	
Stacking sequence	$[0°/45°/135°/90°/90°/135°/45°/0°]_2$	$[0°]$
Ply type	Mitsubishi/UNI/UTS 700/NCT 304-1	
Mechanical properties of the ply (Mitsubishi Chemical Carbon Fiber and Composite 304-1)		
Shear strength of ply matrix failure (S_{12})		97 MPa
Tensile strength of ply matrix failure (X_{22}^t)		83 MPa

Tensile strength of ply fiber failure (X_{11}^{t})	2903 MPa
Compressive strength of ply fiber failure (X_{11}^{c})	1675 MPa
Internal friction coefficient (e_{nl})	-0.3566 [87]

The comparison of the measured chip formation angles between the MD and UD CFRPs is shown in Fig. 7.2. For the UD CFRP, the chip formation angle varies in the range of $[27°, 71°]$ when the fiber orientation increases from $0°$ to $180°$. This demonstrates that chip formation angle is highly dependent on the fiber orientation in cutting UD CFRP. However, in cutting MD CFRP, the experimental results show that the chip formation angles the maximum variations of the chip formation angles among the UD plies with different fiber orientations are 15.6°, 4.8°, and 8.7° for 0°, 15°, and 30° MD CFRPs, respectively, with the average vibration of 9.7°. As an example, Fig. 7.3(a) and (b) show the measured 2-D and 3-D topographic maps of the uncut material surface, machined surface, and chip formation plane, respectively. It is observed that the boundaries between the chip formation plane and the neighbouring material surfaces are straight (Fig. 7.3(a)), which demonstrates that the chip formation plane is flat among different plies in MD CFRP. This is proved by the 3-D topography of the chip formation plane shown in Fig. 7.3(a). Therefore, the chip formation angles of UD plies with different fiber orientations converge under MD CFRP configuration. By projecting the chip formation plane in the orthogonal cutting plane as shown in Fig. 7.3(c), the chip formation angles for all the plies in cutting MD CFRP are measured through linearly fitting the position data of the corresponding chip formation planes, with the results shown in Fig. 7.2(b).

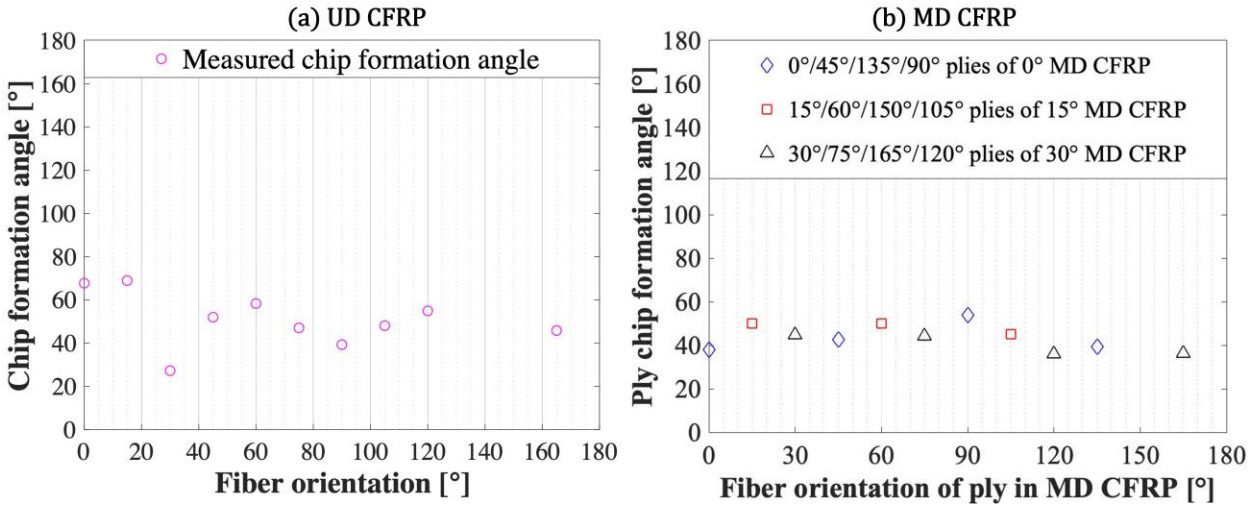

Figure 7.2 Measured chip formation angles for UD and MD CFRPs at 180 μm uncut chip thickness. The chip formation angle for 150° ply of 15° MD CFRP is not provided due to the bulk damage of the material.

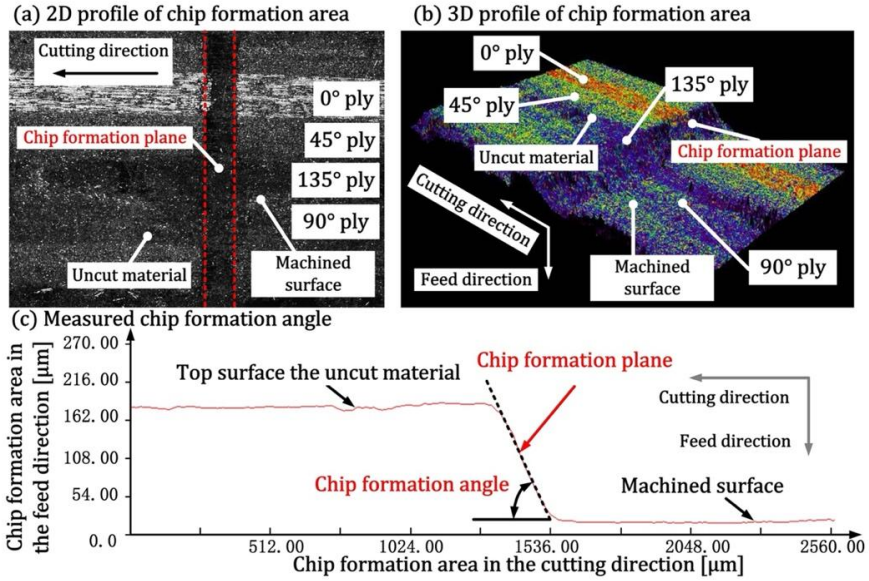

Figure 7.3 Measured chip formation plane for $[0°/45°/135°/90°/90°/135°/45°/0°]_2$ MD CFRP at 180 μm uncut chip thickness. In the 2-D topographic map (a), the boundaries between the chip formation plane and the neighbouring material surfaces are straight, indicating a constant chip formation angle among plies with different fiber orientations. This is supported by the 3-D topographic map (b). The measurement of chip formation angle is presented in (c).

7.2. Mechanics model of orthogonal cutting of MD CFRP

In orthogonal cutting of CFRP, the chips are formed owing to the fracture of the uncut material in the chip formation region. Three assumptions are introduced in developing the mechanics model: (1) The chip formation region is modeled as a flat plane with infinitely small

thickness; (2) The coefficient of friction between the chip and tool rake face does not change with the fiber orientation; (3) The cutting tool is assumed to be perfectly sharp. Because the MD CFRP is composed of plies with various fiber orientations, I define the fiber orientation sequence of all plies starting from the first ply on one side as: $[\theta_1/\theta_2/\theta_3/\ .../\theta_i/\ .../\theta_n]$, and the corresponding chip formation angles are $[\varphi_1/\varphi_2/\varphi_3/\ .../\varphi_i/\ .../\varphi_n]$. Fig. 7.4 shows the schematic of the chip formation in orthogonal cutting of the ith ply of the MD CFRP. The fiber cutting angle for the ith ply is defined as the intersection angle between the chip formation plane and the fiber orientation:

$$\delta_i = \varphi_i - \theta_i \tag{7.1}$$

The normal and shear forces on the ith chip formation plane are represented by $F_{n,i}$ and $F_{s,i}$, and the normal and shear stresses are:

$$\begin{aligned} \sigma_{n,i} &= F_{n,i}/A = F_{n,i}sin\varphi_i/(bh) \\ \tau_{s,i} &= F_{s,i}/A = F_{s,i}sin\varphi_i/(bh) \end{aligned} \tag{7.2}$$

where A is the area of the chip formation plane. b is the width of each ply, and h is the uncut chip thickness.

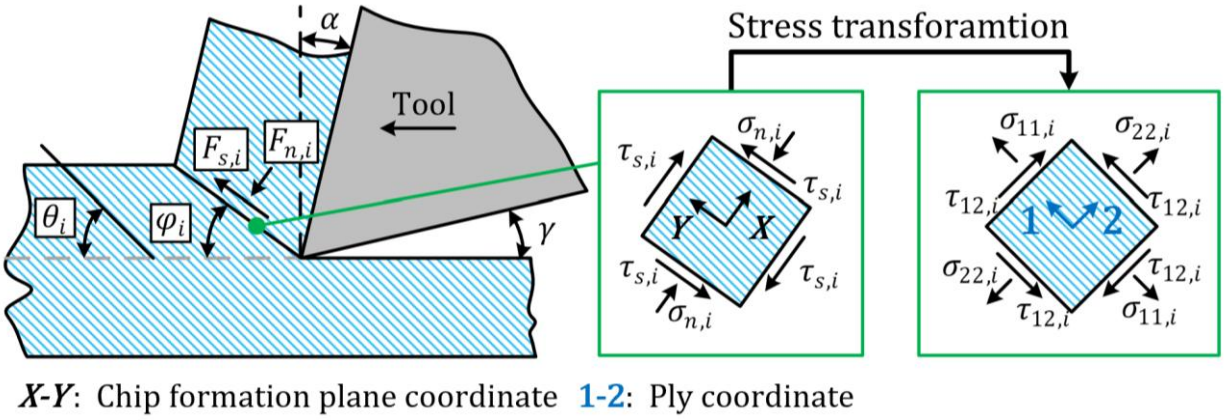

Figure 7.4 Orthogonal cutting configuration for ith ply and stress transformation to ply coordinate in the chip formation region.

The ratio between the normal stress and shear stress in each ply is derived from the force equilibrium condition of the chip as:

$$\frac{\sigma_{n,i}}{\tau_{s,i}} = -tan\left(\varphi_i + \beta_f - \alpha\right) = -T_i \tag{7.3}$$

where α and β are the tool rake angle and friction angle between the formed chips and the rake face, respectively. To evaluate the failure of the uncut material, stress transformation is performed from the chip formation plane ($\sigma_{n,i}, \tau_{s,i}$) to the CFRP ply coordinate (see Fig. 7.4):

$$\begin{aligned}\sigma_{22,i} &= \sigma_{n,i}cos^2\delta_i + 2\tau_{s,i}sin\delta_i cos\delta_i \\ \sigma_{11,i} &= \sigma_{n,i}sin^2\delta_i - 2\tau_{s,i}sin\delta_i cos\delta_i \\ \tau_{12,i} &= -\sigma_{n,i}sin\delta_i cos\delta_i + \tau_{s,i}(cos^2\delta_i - sin^2\delta_i)\end{aligned} \tag{7.4}$$

By substituting Eq. (7.3) into Eq. (7.4), the stresses ($\sigma_{22,i}, \sigma_{11,i}, \tau_{12,i}$) are expressed as functions of fiber cutting angle and shear stress:

$$\begin{aligned}\sigma_{22,i} &= \tau_{s,i}(2sin\delta_i cos\delta_i - T_i cos^2\delta_i) \\ \sigma_{11,i} &= \tau_{s,i}(-2sin\delta_i cos\delta_i - T_i sin^2\delta_i) \\ \tau_{12,i} &= \tau_{s,i}(cos^2\delta_i - sin^2\delta_i + T_i cos\delta_i sin\delta_i)\end{aligned} \tag{7.5}$$

Because the sign (or direction) of the shear stress ($\tau_{s,i}$) on the chip formation plane is positive to form the chip flow, the signs of the stresses ($\sigma_{22,i}, \sigma_{11,i}, \tau_{12,i}$) are only related to the chip formation angle (or fiber cutting angle) and fiber orientation. Therefore, the signs of stresses ($\sigma_{22,i}, \sigma_{11,i}$) are already known for a given fiber orientation and a potential chip formation angle. In this model, Hashin's and Puck's failure criteria [75, 76] including fiber tension, fiber compression, matrix tension, and matrix compression used to model the CFRP failure, expressed as:

(a) Fiber tension and compression failure modes:

$$\begin{aligned}\left(\frac{\sigma_{11,i}}{X_{11}^t}\right)^2 + \left(\frac{\tau_{12,i}}{S_{12}}\right)^2 &= 1, \quad for \;\; \sigma_{11,i} \geq 0 \\ \left(\frac{\sigma_{11,i}}{X_{11}^c}\right)^2 &= 1, \quad for \;\; \sigma_{11,i} < 0\end{aligned} \tag{7.6}$$

(b) Matrix tension and compression failure modes:

$$\begin{aligned}\left(\frac{\sigma_{22,i}}{X_{22}^t}\right)^2 + \left(\frac{\tau_{12,i}}{S_{12}}\right)^2 &= 1, \quad for \;\; \sigma_{22,i} \geq 0 \\ \left(\frac{\tau_{12,i}}{S_{12} + e_{nl}\sigma_{22}}\right)^2 &= 1, \quad for \;\; \sigma_{22,i} < 0\end{aligned} \tag{7.7}$$

where e_{nl} represents the enhancement effect of the normal compression on the shear strength owing to the 'internal friction' [58]. Substitute Eq. (7.5) into Eqs. (7.6) and (7.7), the required shear stress ($\tau_{s,i}$) for activating the failure criterion is obtained, and the corresponding fiber-matrix failure mode is defined as the chip formation mode. Then, the tangential cutting force and power for the ith ply in the MD CFRP are obtained by projecting the forces in the chip formation plane to the tangential direction:

$$F_{tc,i} = bh\frac{\tau_{s,i}(\varphi_i)cos\,(\beta_f - \alpha)}{sin(\varphi_i)cos\,(\varphi_i + \beta_f - \alpha)} \tag{7.8}$$

$$F_{tc,i} = bh\frac{\tau_{s,i}(\varphi_i)cos\,(\beta_f - \alpha)}{sin(\varphi_i)cos\,(\varphi_i + \beta_f - \alpha)} \tag{7.9}$$

According to the experimental results in section 7.1, the chip formation angles at different UD plies converge in cutting of MD CFRP. Because the chip formation angles of the plies are influenced by the interlaminar bonding between adjacent plies, the chip formation plane is formed when the total energy in cutting MD CFRP laminate reaches the minimum value for all plies. The total cutting power is expressed as:

$$W = \sum_{i=1}^{n} W_i = bhV\frac{\sum_{i=1}^{n}\tau_{s,i}\,cos\,(\beta_f - \alpha)}{sin(\varphi_e)cos\,(\varphi_e + \beta_f - \alpha)} \tag{7.10}$$

where V is the cutting speed and φ_e is the chip formation angle for all plies corresponding to the minimum cutting energy. Therefore, φ_e is identified corresponding to the minimum energy (W) in cutting MD CFRP. The resultant tangential and resultant cutting forces are then determined as:

$$F_{tc} = \sum_{i=1}^{n} F_{tc,i} = bh\frac{\sum_{i=1}^{n}\tau_{s,i}\,cos\,(\beta_f - \alpha)}{sin(\varphi_e)cos\,(\varphi_e + \beta_f - \alpha)}$$
$$F_{fc} = \frac{F_{tc}}{cos\,(\beta_f - \alpha)} \tag{7.11}$$

It should be noted that with the identified chip formation angle φ_e and shear stress $\tau_{s,i}$ from the total minimum energy of the plies, the fiber-matrix failure modes for chip formation are predicted from Eqs. (7.6) and (7.7) rather than pre-assumed. This is another difference between the model in this chapter compared to the mechanics models in the literature. Finally, by scanning the fiber orientation from 0° to 180°, the fiber-matrix failure mode, chip formation angle, and cutting forces are predicted in the entire fiber orientation range for cutting MD CFRP.

7.3. Simulations and experimental validation

Fig. 7.5 shows the predicted fiber-matrix failure modes to enable chip formation, and the chip formation angle for orthogonal cutting of the UD and MD CFRPs at various fiber orientations. Because the UD CFRP workpiece is composed of the plies oriented in the same direction, the chip formation modes of different plies are naturally the same. The regions of different colors in Fig. 7.5 refer to the chip formation modes predicted at a given fiber orientation and a potential chip formation angle. The curved line refers to the prediction of chip formation angles for the UD CFRP with respect to the fiber orientation. The predicted chip formation angles for the three MD CFRP laminates with different fiber orientations listed in Table 7.1 are included in the figure. Owing to the interlaminar bonding, the chip formation angles of all plies converge to a constant value for each MD CFRP laminate. The arrows in the figure show the changes of the chip formation angles from UD to MD configuration corresponding to the same fiber orientation angle. For example, for $0°$ MD CFRP, the chip formation angles for $0°$,$90°$, and $135°$ plies decrease, while it increases slightly for the $0°$,$45°$, and $90°$ ply. In addition, the arrows show that the chip formation modes for plies at certain fiber orientations change because of the variations of the chip formation angles. For example, The chip formation modes for the ply at $150°$ fiber orientations change from the matrix compression failure to the matrix tension failure mode. It is also noticed that the chip formation angles between MD and UD CFRP are closer when the chip formation is dominated by the fiber tension failure mode.

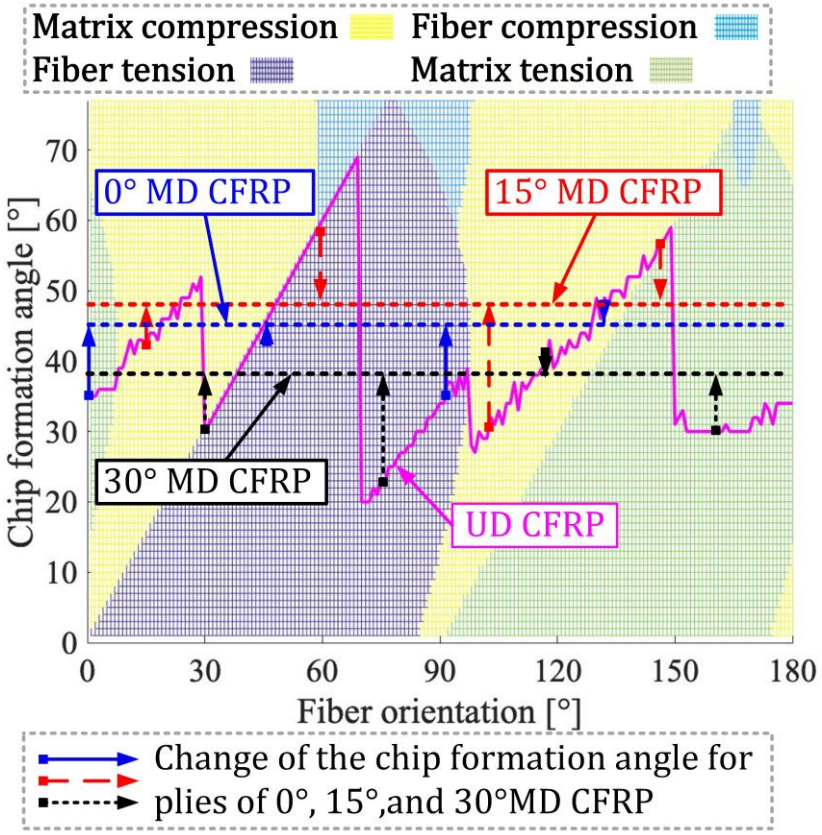

Figure 7.5 Predicted fiber-matrix failure modes for chip formation in cutting UD CFRP, and the changes of the chip formation angles owing to the interlaminar bonding for all plies in MD CFRP.

Fig. 7.6 presents the comparisons between the simulations and the experimental results for chip formation angle and cutting forces in cutting UD and MD CFRPs at 180 μm uncut chip thickness. For the chip formation angle of MD CFRP, an average error of 5.4° between the predictions and the experimental results is observed. The tangential and feed forces for the UD CFRP vary with the fiber orientation, while the forces remain close to each other for all three fiber orientations in cutting MD CFRP owing to the interlaminar bonding. It is noticed that the predicted cutting forces can capture the variations of both the tangential and feed cutting forces. Thus, it is experimentally proved that interlaminar bonding plays an important role in determining the chip formation and cutting forces, which can be quantitatively predicted from the developed mechanics model. The prediction error may be due to the fiber misalignment of the CFRP laminates. The results for UD CFRP in the fiber orientation range of $[135°, 150°]$ are not listed due to the occurrence of bulk material damage.

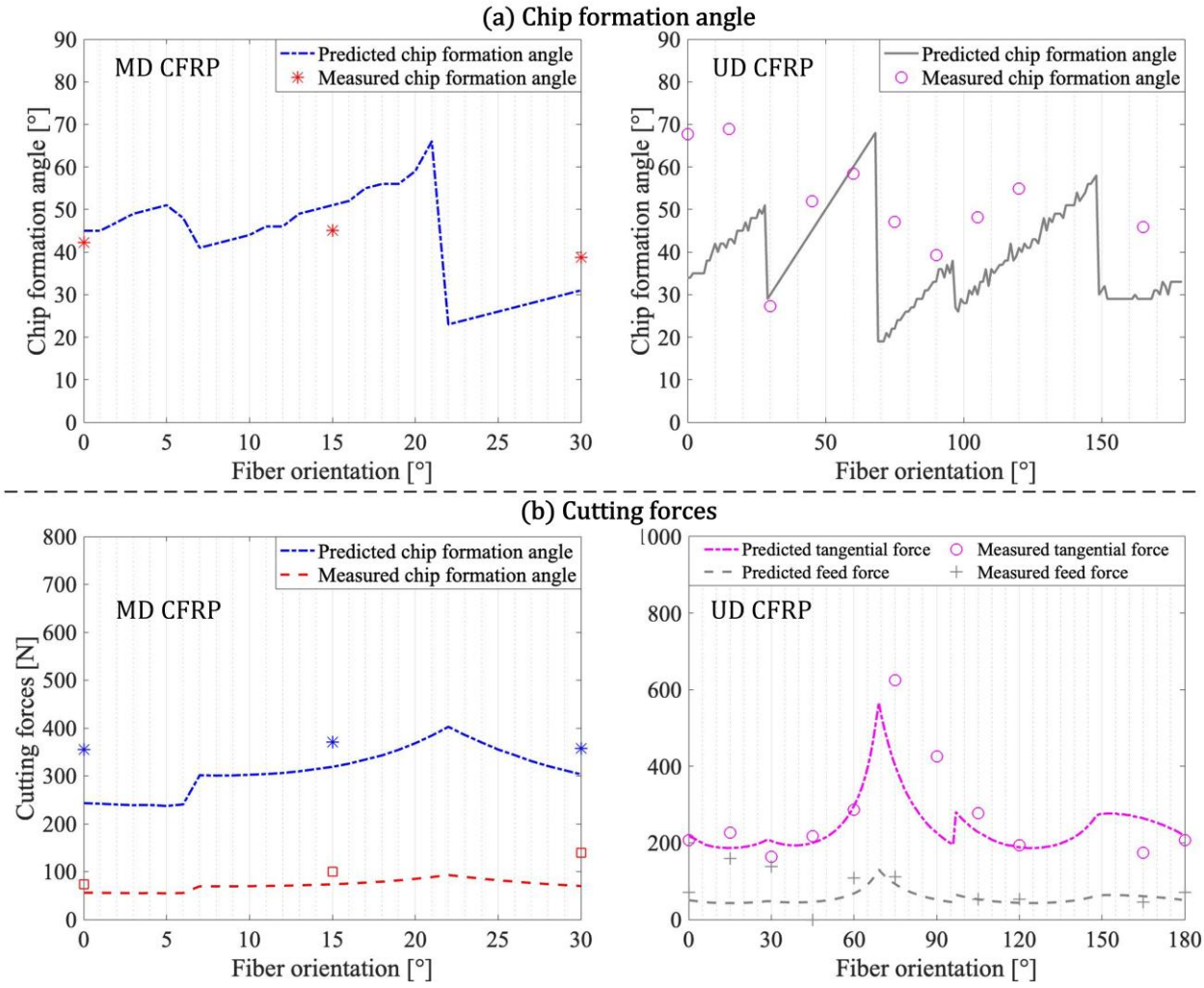

Figure 7.6 Comparison of chip formation angle and cutting forces for UD CFRP (or plies) and MD CFRP. (The calculated tangential and feed forces refer to the summations of the measured forces of all plies in MD CFRP without considering the interlaminar effect.)

7.4. Conclusion

The orthogonal cutting experiments of MD CFRP in this chapter show that the chip formation angles for plies of different fiber orientations converge to a constant value as opposed to UD CFRP. The analytical mechanics model reveals that the fiber-matrix failure mode and chip formation angle change from UD to MD configuration to satisfy the total minimum cutting energy of all plies. Besides, the increase of the cutting forces for MD CFRP compared to the calculated results by directly adding the forces considering cutting each UD plies individually (Fig. 7.6(b)) are proved to be the result of interlaminar bonding. The developed mechanics model is validated based on the agreements between the predicted and experimentally measured chip formation angles and cutting

forces at various fiber orientations for MD CFRP. The effects of the variation of interlaminar bonding strength and tool wear on the cutting mechanics of MD CFRP will be a future independent chapter. In addition, the model will be evaluated for high cutting speed conditions by implementing the mechanical properties of CFRP including the strain rate and temperature effects.

8. Conclusions

Different from metal cutting, the chip formation mechanism, including the chip formation mode, chip formation angle, and cutting force generation, varies significantly with the fiber orientation, tool geometry, and process parameters in machining of CFRP. Understanding the chip formation mechanism and its variation with the fiber orientation is essential to optimize the process condition and enhance the machining performance. Based on the analytical approaches, this thesis focuses on the effect of the fiber orientation, process parameters, and mechanical properties of the CFRP material on the chip formation mechanism in orthogonal machining process.

8.1 Contributions and limitations

In the orthogonal cutting of 0° fiber orientation CFRP, the failure initiation of uncut material includes the Euler buckling [43] and micro buckling [48] modes. In this thesis, to explain the failure process under this cutting condition, the shearing-buckling deformation is proposed to investigate the chip formation mechanism. It is found that the uncut material failure starts from the shearing, followed by fracture propagation in the shear interface layer between the uncut material and the remaining workpiece. The cutting forces remain constant during this fracture propagation and the uncut material can be treated as a cantilever beam. Considering that both the strengths for Euler buckling and micro buckling decrease when the length of the cantilever beam increases, the occurrence of Euler buckling or micro buckling depends on which buckling mode requires a lower cutting energy. In addition, the chip formed is mainly composed of two geometries with different lengths which validated the proposed mechanism. However, there exist two limitations to this model: the chip formation angle of the uncut material fracture can not be predicted owing to the assumed buckling failure mechanism, and the interaction between the shear stress and normal stress on the uncut material is not given.

To overcome these two limitations and achieve the prediction of the chip formation mechanism in the entire fiber orientation range, an analytical mechanics model is proposed to predict the chip formation mode, chip formation angle, and cutting forces in the entire fiber orientation range using continuum mechanics. Rather than assuming the chip formation mode from experimental observation, this model predicts the failure mode of the CFRP material based on the stress state as a function of fiber orientation. Hashin-Puck failure criterion is used to predict the chip formation mode and its transition with the fiber orientation. It is found that the uncut material

breaks in the direction where the required cutting energy is minimum. The dominant chip formation mechanism is composed of fiber tension, matrix compression and matrix tension. It is also noted that fiber compression or buckling mode appears as the secondary mode owing to the interactive effect between the compressive and shear stresses. Besides, the enhancement effect of the normal compression on the shear strength ('internal friction' for matrix compression mode) is proved to determine the chip formation and the variation of the cutting forces. On the other hand, the physical explanation of this enhancement effect is questionable due to the unclear mechanism of the 'internal friction' generation in the CFRP materials.

To further understand the role of this enhancement effect of shear stress under transverse compression, a frictional-damage mechanics model is then proposed to investigate the damage of each constituent in the workpiece. The Coulomb friction on the cracked surfaces, rather than the 'internal friction' is considered. The proposed model demonstrates that the friction at the fractured surfaces plays an important role in the fracture plane orientation, which is quantitatively determined under different stress states. The model provides the physical basis of the damage propagation and fractured plane formation from an energy perspective, and there is no need to identify the friction-related term from the fracture angle measurement. In addition, the friction in the damaged area increases the ultimate strength of the matrix compressive failure mode which affects the chip formation process and the variation of the chip formation angle. Therefore, the friction still influences the chip formation after the material is completely damaged.

For the MD CFRP materials, the interlaminar bonding between plies of different orientations starts to influence the chip formation in the machining process. It is found that the plies of different orientations tend to form a constant chip formation plane owing to this bonding effect. According to the developed mechanics model for machining MD CFRP, the chip formation angles of plies with different fiber orientations converge to form a constant chip formation plane in order to achieve minimum total cutting energy. As a result, the cutting forces contributed by each ply change, which are predicted by the model with experimental validation.

However, some limitations still exist from the work in this thesis:

(1) Because the orthogonal cutting experiment is conducted with a low cutting speed of 5m/min owing to the limitation of the setup, the effect of the cutting speed or the strain rate on the uncut material deformation is not included. For example, the nonlinear shear behavior of the matrix can change to brittle mode under a higher strain rate.

(2) Another problem in practical machining operations is the temperature, which can dramatically change the matrix and fiber-matrix bonding properties. The fiber compression failure or buckling failure behavior can change because the elastic modulus of the matrix reduces by 60% when the cutting temperature reaches the glass transition temperature. Therefore, the effect of the temperature variation on chip formation in machining process needs to be discussed in the future.

8.2 Future work

This thesis proposes analytical mechanics models for the fundamental chip formation mechanism under orthogonal machining configuration. The relationship between the chip formation mechanism and the fiber orientation is quantitatively explained. Further work in the future is suggested as follows:

(1) For more practical applications such as edge trimming and drilling, the cutting speed and heat generation need to be considered because the mechanical properties for the matrix change to be rubber-like once the cutting temperature is beyond the glass transition temperature. The developed mechanics model can be implemented or updated including the mechanical strengths of the matrix material with the temperature effect.

(2) The delamination which frequently occurs in the cutting process reduces the machinability of the CFRP material. Therefore, the physical explanation behind the part delamination needs to be investigated to maintain the workpiece performance in the working condition.

(3) For the material deformation in the pressing region which is related to the surface quality after machining, quantitative analyses may be performed to understand the relationship between the tool edge geometry and the material deformation in the pressing region, which influences the machined surface quality.

References

[1] Michels, J., Widmann, R., Czaderski, C., Allahvirdizadeh, R. and Motavalli, M., 2015. Glass transition evaluation of commercially available epoxy resins used for civil engineering applications. Composites Part B: Engineering, 77, pp.484-493.

[2] Bazli, M. and Abolfazli, M., 2020. Mechanical properties of fibre reinforced polymers under elevated temperatures: An overview. Polymers, 12(11), p.2600.

[3] Jang, J.U., Park, H.C., Lee, H.S., Khil, M.S. and Kim, S.Y., 2018. Electrically and thermally conductive carbon fibre fabric reinforced polymer composites based on nanocarbons and an in-situ polymerizable cyclic oligoester. Scientific reports, 8(1), pp.1-9.

[4] Rolfes, R. and Hammerschmidt, U., 1995. Transverse thermal conductivity of CFRP laminates: A numerical and experimental validation of approximation formulae. Composites Science and Technology, 54(1), pp.45-54.

[5] Sedighi, M., Afshari, D. and Nazari, F., 2018. Investigation of the effect of sheet thickness on residual stresses in resistance spot welding of aluminum sheets. Proceedings of the Institution of Mechanical Engineers, Part C: Journal of Mechanical Engineering Science, 232(4), pp.621-638.

[6] Yoshitake, I., Tsuda, H., Itose, J. and Hisabe, N., 2014. Effect of discrepancy in thermal expansion coefficients of CFRP and steel under cold temperature. Construction and Building Materials, 59, pp.17-24.

[7] Wen, J., Xia, Z. and Choy, F., 2011. Damage detection of carbon fiber reinforced polymer composites via electrical resistance measurement. Composites Part B: Engineering, 42(1), pp.77-86.)

[8] Lin, S.C. and Chen, I.K., 1996. Drilling carbon fiber-reinforced composite material at high speed. Wear, 194(1-2), pp.156-162.

[9] Feito, N., López-Puente, J., Santiuste, C. and Miguélez, M.H., 2014. Numerical prediction of delamination in CFRP drilling. Composite Structures, 108, pp.677-683.

[10] Han, L., Zhang, J. and Sun, T., 2022. Tailoring fiber arrangement in subsurface damage layer of unidirectional CFRP composites by reverse multi-pass cutting. Composites Science and Technology, p.109571.

[11] Friend, C.A., Clyae, R.W. and Valentine, G.G. 'Machining graphite composite materials' Proc 6th Symposium on Composite Materials in Engineering Design (St Louis, MO, May 11-12, 1972)pp 217-225

[12] KoPlev, A.A., Lystrup, A. and Vorm, T., 1983. The cutting process, chips, and cutting forces in machining CFRP. composites, 14(4), pp.371-376.

[13] Wang, D.H., Ramulu, M. and Arola, D., 1995. Orthogonal cutting mechanisms of graphite/epoxy composite. Part I: unidirectional laminate. International Journal of Machine Tools and Manufacture, 35(12), pp.1623-1638.

[14] Wang, D.H., Ramulu, M. and Arola, D., 1995. Orthogonal cutting mechanisms of graphite/epoxy composite. Part II: multi-directional laminate. International Journal of Machine Tools and Manufacture, 35(12), pp.1639-1648.

[15] Dandekar, C.R. and Shin, Y.C., 2012. Modeling of machining of composite materials: a review. International Journal of Machine tools and manufacture, 57, pp.102-121.

[16] Arola, D. and Ramulu, M., 1997. Orthogonal cutting of fiber-reinforced composites: a finite element analysis. International journal of mechanical sciences, 39(5), pp.597-613.

[17] Tsai, S.W., 1968. Strength theories of filamentary structure. Fundamental aspects of fiber reinforced plastic composites.

[18] Hill, R., 1965. Theory of mechanical properties of fibre-strengthened materials—III. Self-consistent model. Journal of the Mechanics and Physics of Solids, 13(4), pp.189-198.

[19] Ramesh, M.V., Seetharamu, K.N., Ganesan, N. and Sivakumar, M.S., 1998. Analysis of machining of FRPs using FEM. International Journal of Machine Tools and Manufacture, 38(12), pp.1531-1549.

[20] Mahdi, L.C. Zhang, in: Abrasive Technology: Current Develop-ment and Applications, Vol. I, World Scientific, Singapore, 1999, p. 337.

[21] Mahdi, M. and Zhang, L., 2001. A finite element model for the orthogonal cutting of fiber-reinforced composite materials. Journal of materials processing technology, 113(1-3), pp.373-377.

[22] Chamis, C.C., 1983, February. NASA Tech. Memo. 83320. In 38th annual conference of the society of plastic industry (SPI).

[23] Arola, D., Sultan, M.B. and Ramulu, M., 2002. Finite element modeling of edge trimming fiber reinforced plastics. J. Manuf. Sci. Eng., 124(1), pp.32-41.

[24] Lasri, L., Nouari, M. and El Mansori, M., 2009. Modelling of chip separation in machining unidirectional FRP composites by stiffness degradation concept. Composites Science and Technology, 69(5), pp.684-692.

[25] Nayak, D., Singh, I., Bhatnagar, N. and Mahajan, P., 2004, June. An analysis of machining Induced damages in FRP composites—a micromechanics finite element approach. In AIP Conference Proceedings (Vol. 712, No. 1, pp. 327-331). American Institute of Physics.

[26] Nayak, D., Bhatnagar, N. and Mahajan, P., 2005. Machining studies of UD-FRP composites part 2: finite element analysis. Machining science and technology, 9(4), pp.503-528.

[27] Rao, G.V.G., Mahajan, P. and Bhatnagar, N., 2007. Micro-mechanical modeling of machining of FRP composites–Cutting force analysis. Composites science and technology, 67(3-4), pp.579-593.

[28] Mkaddem, A., Demirci, I. and El Mansori, M., 2008. A micro–macro combined approach using FEM for modelling of machining of FRP composites: Cutting forces analysis. Composites science and technology, 68(15-16), pp.3123-3127.

[29] Dandekar, C.R. and Shin, Y.C., 2008. Multiphase finite element modeling of machining unidirectional composites: prediction of debonding and fiber damage. Journal of manufacturing science and engineering, 130(5).

[30] Calzada, K.A., Kapoor, S.G., DeVor, R.E., Samuel, J. and Srivastava, A.K., 2012. Modeling and interpretation of fiber orientation-based failure mechanisms in machining of carbon fiber-reinforced polymer composites. Journal of Manufacturing Processes, 14(2), pp.141-149.

[31] Abena, A., Soo, S.L. and Essa, K., 2015. A finite element simulation for orthogonal cutting of UD-CFRP incorporating a novel fibre-matrix interface model. Procedia CIRP, 31, pp.539-544.

[32] Yan, X., Reiner, J., Bacca, M., Altintas, Y. and Vaziri, R., 2019. A study of energy dissipating mechanisms in orthogonal cutting of UD-CFRP composites. Composite Structures, 220, pp.460-472.

[33] Xu, W., Zhang, L.C. and Wu, Y., 2014. Elliptic vibration-assisted cutting of fibre-reinforced polymer composites: understanding the material removal mechanisms. Composites Science and Technology, 92, pp.103-111.

[34] Xu, W. and Zhang, L., 2017. A new approach to characterising the surface integrity of fibre-reinforced polymer composites during cutting. Composites Part A: Applied Science and Manufacturing, 103, pp.272-282.

[35] Xu, W. and Zhang, L., 2019. Heat effect on the material removal in the machining of fibre-reinforced polymer composites. International Journal of Machine Tools and Manufacture, 140, pp.1-11.

[36] Xu, X. and Jin, X., 2021. 3-D finite element modeling of sequential oblique cutting of unidirectional carbon fiber reinforced polymer. Composite Structures, 256, p.113127.

[37] Puw, H.Y., Hocheng, H. and Kuo, H.C., 1995. Anisotropic chip formation models of cutting of FRP. In Proceedings of ASME Symposium on Material Removal and Surface Modification Issues in Machining Processes, New York.

[38] Takeyama, H. and Iijima, N., 1988. Machinability of glassfiber reinforced plastics and application of ultrasonic machining. CIRP Annals, 37(1), pp.93-96.

[39] Merchant, M.E., 1945. Mechanics of the metal cutting process. II. Plasticity conditions in orthogonal cutting. Journal of applied physics, 16(6), pp.318-324.

[40] Bhatnagar, N., Ramakrishnan, N., Naik, N.K. and Komanduri, R.B.A.O.S.U., 1995. On the machining of fiber reinforced plastic (FRP) composite laminates. International journal of machine tools and manufacture, 35(5), pp.701-716.

[41] Zhang, L.C., Zhang, H.J. and Wang, X.M., 2001. A force prediction model for cutting unidirectional fibre-reinforced plastics.

[42] Xu, W. and Zhang, L.C., 2014. On the mechanics and material removal mechanisms of vibration-assisted cutting of unidirectional fibre-reinforced polymer composites. International Journal of Machine Tools and Manufacture, 80, pp.1-10.

[43] Puw, H.Y. and Hocheng, H., 1999. Milling of polymer composites. Manufacturing Engineering and Materials Processing, 53, pp.267-294.

[44] Xu, W. and Zhang, L., 2016. Mechanics of fibre deformation and fracture in vibration-assisted cutting of unidirectional fibre-reinforced polymer composites. International Journal of Machine Tools and Manufacture, 103, pp.40-52.

[45] Jahromi, A.S. and Bahr, B., 2010. An analytical method for predicting cutting forces in orthogonal machining of unidirectional composites. Composites Science and Technology, 70(16), pp.2290-2297.

[46] Qi, Z., Zhang, K., Cheng, H., Wang, D. and Meng, Q., 2015. Microscopic mechanism based force prediction in orthogonal cutting of unidirectional CFRP. The International Journal of Advanced Manufacturing Technology, 79(5), pp.1209-1219.

[47] Chen, L., Zhang, K., Cheng, H., Qi, Z. and Meng, Q., 2017. A cutting force predicting model in orthogonal machining of unidirectional CFRP for entire range of fiber orientation. The International Journal of Advanced Manufacturing Technology, 89(1-4), pp.833-846.

[48] Voss, R., Seeholzer, L., Kuster, F. and Wegener, K., 2019. Analytical force model for orthogonal machining of unidirectional carbon fibre reinforced polymers (CFRP) as a function of the fibre orientation. Journal of Materials Processing Technology, 263, pp.440-469.

[49] Song, C. and Jin, X., 2020. Shearing-buckling mechanism in orthogonal cutting of unidirectional carbon fiber reinforced polymer. Journal of Materials Processing Technology, 280, p.116612.

[50] Paris, F. and Jackson, K.E., 2001. A study of failure criteria of fibrous composite materials (No. NAS 1.26: 210661).

[51] Pinho, S.T., Dávila, C.G., Camanho, P.P., Iannucci, L. and Robinson, P., 2005. Failure models and criteria for FRP under in-plane or three-dimensional stress states including shear non-linearity (No. NASA/TM-2005-213530).

[52] Hill, R., 1948. A theory of the yielding and plastic flow of anisotropic metals. Proceedings of the Royal Society of London. Series A. Mathematical and Physical Scïiences, 193(1033), pp.281-297.

[53] Tsai, S.W., 1965. Strength Characteristics of Composite Materials. Philco Corp Newport Beach CA.

[54] Hoffman, O., 1967. The brittle strength of orthotropic materials. Journal of Composite Materials, 1(2), pp.200-206.

[55] Tsai, S.W. and Wu, E.M., 1971. A general theory of strength for anisotropic materials. Journal of composite materials, 5(1), pp.58-80.

[56] Hashin, Z. and Rotem, A., 1973. A fatigue failure criterion for fiber reinforced materials. Journal of composite materials, 7(4), pp.448-464.

[57] Hashin, Z., 1980. Failure criteria for unidirectional fiber composites. ASME Journal of Applied Mechanics, 47(2): 329–334.

[58] Puck, A. and Schürmann, H., 2004. Failure analysis of FRP laminates by means of physically based phenomenological models. In Failure criteria in fibre-reinforced-polymer composites (pp. 832-876). Elsevier.

[59] Nusayr, A. M., Paslay, P. R., 1972. Buckling of an infinite sheet with a one-sided constraint. J. Appl. Mech. 39, 302-303.

[60] Bradley, W.L., 1989. Relationship of matrix toughness to interlaminar fracture toughness. Compos Mater Series. Vol. 6, 159-187.

[61] Steif, P. S., 1990. A model for kinking in fiber composites—I. Fiber breakage via micro-buckling. Int. J. Solids. Struc. 26, 549-561.

[62] Steif, P. S., 1990. A model for kinking in fiber composites—II. Kink band formation. Int. J. Solids. Struc. 26, 563-569.

[63] Rosen, B.W., 1965. Mechanics of Composite Strengthening.

[64] Hahn, H. T., Sohi, M. M., 1986. Buckling of a fiber bundle embedded in epoxy. Compos. Sci. Technol. 27, 25-41.

[65] Soutis, C., 1991. Measurement of the static compressive strength of carbon-fibre/epoxy laminates. Compos. Sci. Technol. 42, 373-392.

[66] Sackfield, A., Dini, D., Hills, D. A., 2005. The finite and semi-infinite tilted, flat but rounded punch. Int. J. Solids. Struc. 42, 4988-5009.

[67] Zhu, Y., 2008. Characterization of interlaminar fracture toughness of a carbon/epoxy composite material. The Pennsylvania State University. Pennsylvania.

[68] Machado, J. J. M., Marques, E. A. S., Campilho, R. D. S. G., da Silva, L. F. M., 2017. Mode II fracture toughness of CFRP as a function of temperature and strain rate. Compos. Part B: Eng. 114, 311-318

[69] Friedrich, K., Walter, R., Carlsson, L. A., Smiley, A. J., Gillespie, J. W., 1989. Mechanisms for rate effects on interlaminar fracture toughness of carbon/epoxy and carbon/PEEK composites. J. Mater. Sci. 24, 3387-3398.

[70] Matzenmiller, A.L.J.T.R., Lubliner, J. and Taylor, R.L., 1995. A constitutive model for anisotropic damage in fiber-composites. Mechanics of materials, 20(2), pp.125-152.

[71] Ismail, Y., Sheng, Y., Yang, D. and Ye, J., 2015. Discrete element modelling of unidirectional fibre-reinforced polymers under transverse tension. Composites Part B: Engineering, 73, pp.118-125.

[72] Anderson, T.L., 2017. Fracture mechanics: fundamentals and applications. CRC press.

[73] Malvern, L.E., 1969. Introduction to the Mechanics of a Continuous Medium (No. Monograph).

[74] Maimi, P., Mayugo, J.A. and Camanho, P.P., 2008. A three-dimensional damage model for transversely isotropic composite laminates. Journal of Composite Materials, 42(25), pp.2717-2745.

[75] Pinho, S.T., Iannucci, L. and Robinson, P., 2006. Physically-based failure models and criteria for laminated fibre-reinforced composites with emphasis on fibre kinking: Part I: Development. Composites Part A: Applied Science and Manufacturing, 37(1), pp.63-73.

[76] Shi, Y., Swait, T. and Soutis, C., 2012. Modelling damage evolution in composite laminates subjected to low velocity impact. Composite structures, 94(9), pp.2902-2913.

[77] Schön, J., 2000. Coefficient of friction of composite delamination surfaces. Wear, 237(1), pp.77-89.

[78] Wiegand, J., Petrinic, N. and Elliott, B., 2008. An algorithm for determination of the fracture angle for the three-dimensional Puck matrix failure criterion for UD composites. Composites Science and Technology, 68(12), pp.2511-2517.

[79] Schirmaier, F.J., Weiland, J., Kärger, L. and Henning, F., 2014. A new efficient and reliable algorithm to determine the fracture angle for Puck's 3D matrix failure criterion for UD composites. Composites science and technology, 100, pp.19-25.

[80] Puck, A., Kopp, J. and Knops, M., 2002. Guidelines for the determination of the parameters in Puck's action plane strength criterion. Composites Science and Technology, 62(3), pp.371-378.

[81] Jin, X. and Song, C., 2022. Orthogonal cutting mechanics of multi-directional carbon fiber reinforced polymer with interlaminar bonding effect. CIRP Annals.

[82] Song, C. and Jin, X., 2021. Fracture angle prediction for matrix failure of carbon-fiber-reinforced polymer using energy method. Composites Science and Technology, 211, p.108869.

[83] Kroll, L. and Hufenbach, W., 1997. Physically based failure criterion for dimensioning of thick-walled laminates. Applied composite materials, 4(5), pp.321-332.

[84] Paris, F. and Jackson, K.E., 2001. A study of failure criteria of fibrous composite materials (No. NAS 1.26: 210661).

[85] Li, X., Hallett, S.R. and Wisnom, M.R., 2008. Predicting the effect of through-thickness compressive stress on delamination using interface elements. Composites Part A: Applied Science and Manufacturing, 39(2), pp.218-230.

[86] Gan, K.W., Hallett, S.R. and Wisnom, M.R., 2013. Measurement and modelling of interlaminar shear strength enhancement under moderate through-thickness compression. Composites Part A: Applied Science and Manufacturing, 49, pp.18-25.

[87] Donadon, M.V., Iannucci, L., Falzon, B.G., Hodgkinson, J.M. and de Almeida, S.F., 2008. A progressive failure model for composite laminates subjected to low velocity impact damage. Computers & Structures, 86(11-12), pp.1232-1252.

Appendix

Fig. A.1 shows the schematic of shearing and fracture zones in the shear interface layer due to the compression stress (σ) at the tool-workpiece interface. As the cutting tool moves forwards, the shear stress of the shear interface layer increases due to the longitudinal compression of rake face. Once mode II fracture is initiated and propagates in the shear interface layer, two zones exist in the layer: fracture zone and shearing zone including elastic sub-zone and damaged sub-zone as shown in Fig. A.1. This phenomenon has also been discussed by Friedrich et al. [69] and Bradley [60].

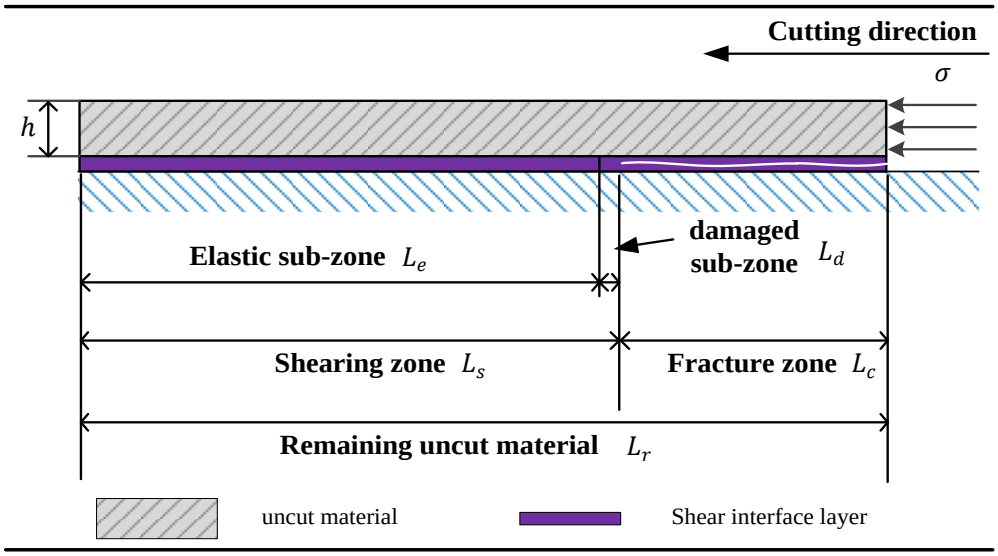

Figure A.1. Schematic of shearing and fracture zones in the shear interface layer.

At the boundary of the two sub-zones, the shear stress in the shear interface layer reaches the maximum because the micro cracks formed in the damaged sub-zone reduce the resistant capacity. In addition, the shear stress is equal to zero in the fracture zone as two new fracture surfaces are formed in the shear interface layer. Therefore, it is the shearing resistance (R) in the shearing zone that determines the value for the compressive force (P) in the fracture initiation and propagation processes based on the force equilibrium condition in the cutting direction.

$$P = \sigma t h = -R \tag{A.1}$$

where σ is the compressive stress, t is the width of workpiece and h is the uncut chip thickness.

The shearing resistance (R) is divided into two parts: shearing resistance (R_1) in elastic sub-zone and shearing resistance (R_2) in the damaged sub-zone.

$$R = R_1 + R_2 \tag{A.2}$$

As shown in Fig. A.2, two different moments during the fracture growth process are presented to explain why the long sheet assumption makes the shearing resistance a constant. Since the damaged sub-zone acts as a transitional stage between elastic shear deformation and fracture, the resistance R_2 is a constant during the fracture propagation. Thus, the change of the resistance R depends on the change of shearing resistance R_1 in the elastic sub-zone. The elastic sub-zone length decreases from L_{e1} to L_{e2} at these two moments, and the origin of x-axis is placed at the boundary between the elastic sub-zone and the damaged sub-zone.

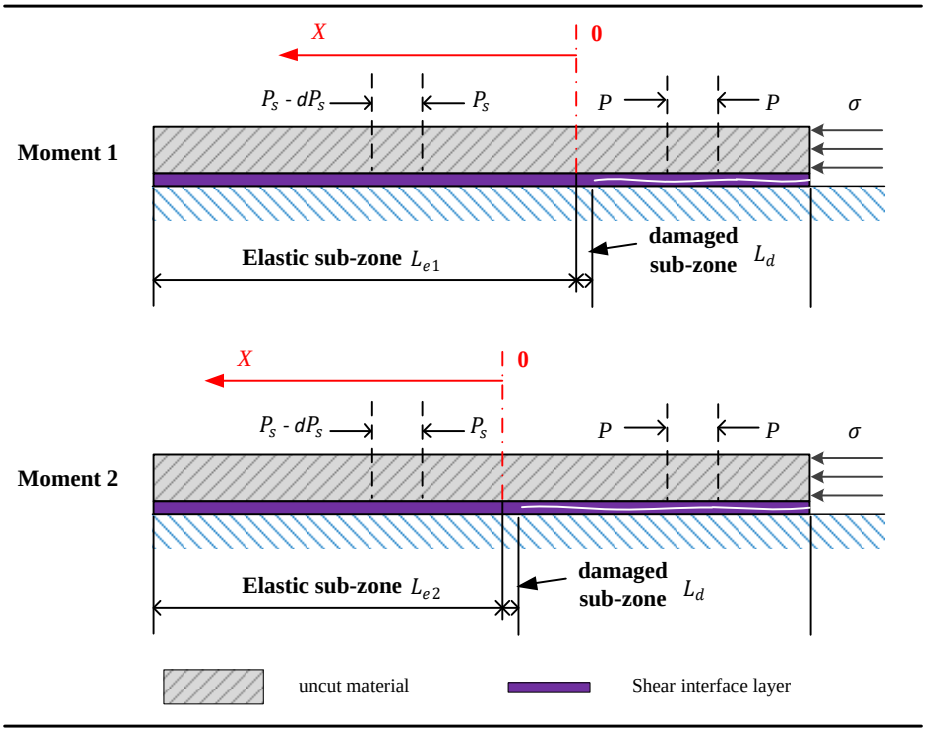

Figure A.2. Fracture propagation moments.

The force equilibrium equation in longitudinal direction for the uncut material in the elastic sub-zone is expressed as

$$\frac{dP_s}{dx} - \tau t = 0 \tag{A.3}$$

where P_s is the compressive force in the elastic sub-zone, t is the width of the workpiece. The shear stress (τ) provided by the shear interface layer is expressed as the function as

$$\tau = G_m \frac{u_x}{2h_m} \tag{A.4}$$

where G_m is the shear modulus, $2h_m$ is the thickness of shear interface layer and u_x is the displacement in the longitudinal direction. The compression force P_s is expressed as

$$P_s = E_a t h \frac{du_x}{dx} \tag{A.5}$$

where h is the real uncut chip thickness and E_a is the elastic modulus of uncut material given in Eq. (3.6).

The force equilibrium Eq. (A.3) is updated as

$$E_a t h \frac{d^2 u_x}{dx^2} - G_m t \frac{u_x}{2h_m} = 0 \tag{A.6}$$

When long sheet assumption applies, both the lengths L_{e1} to L_{e2} are long enough so that the deformation displacement (u_x) of the sheet in the longitudinal direction in the far end approaches to zero, that is, $u_x(\infty) = 0$. This boundary condition applies at both moments during the fracture growth process. After applying the boundary conditions ($u_x(0) = -\frac{\tau_s 2h_m}{G_m}$ and $u_x(\infty) = 0$) to Eq. (A.6), the solution of the displacement in the elastic sub-zone for the two moments is obtained:

$$u_x = -\frac{2\tau_s h_m}{G_m} e^{-\sqrt{\frac{G_m}{2h_m E_a h}}x} \tag{A.7}$$

The compressive force at the boundary of two sub-zones ($x = 0$) is determined according to the Eq. (A.5)

$$P_s = E_a t h \frac{du_x}{dx}\bigg|_{x=0} = \tau_s t \sqrt{\frac{2h_m E_a h}{G_m}} \tag{A.8}$$

The resistance R_1 of the shear interface layer in the elastic sub-zone, which is equal to the compressive force, is given as

$$R_1 = -P_s = -\tau_s t \sqrt{\frac{2h_m E_a h}{G_m}} \quad \text{(A.9)}$$

Therefore, the shearing resistances R is a constant during the fracture growth process according to the Eqs. (A.1) and (A.2), because it is not related to the length of the fracture zone in the shear interface layer, and the boundary condition does not change under the long sheet assumption. Thus, the compressive force P at the tool-uncut material contact surface is also a constant based on force equilibrium condition. It should be noted that the long sheet assumption does not apply when the cutting tool moves close to the left end of the CFRP plate where the remaining uncut material is short.